COMPARISON OF NEAR-SURFACE SEISMIC VELOCITY ESTIMATION METHODS WITH APPLICATION TO ON-SHORE PERU AND OFFSHORE MALAYSIA

A Thesis

Presented to

the Faculty of the Department of Earth and Atmospheric Sciences

University of Houston

In Partial Fulfillment

of the Requirements for the Degree

Master of Science

By

Hui Fan

August 2012

COMPARISON OF NEAR-SURFACE SEISMIC VELOCITY ESTIMATION METHODS WITH APPLICATION TO ON-SHORE PERU AND OFFSHORE MALAYSIA

Hui Fan

APPROVED:

Dr. Christopher Liner, Chairman
Department of Earth and Atmospheric Sciences

Dr. Robert Stewart
Department of Earth and Atmospheric Sciences

Dr. Lee Bell
Geokinetics Inc.

Dean, College of Natural Sciences and Mathematics

Acknowledgements

During my research and my thesis writing there were so many people who provided me support and help, I can not mention and thank them all. However, I would like to single out a few people to express my thanks.

First of all, I would like to express my deepest gratitude to my advisor, Christopher Liner, whose patience and guidance were of immense help when I meet challenges in both research and life. Also I am indebted to Dr. Lee Bell, my committee member and another mentor, who gave me the opportunity to do my research at Geokinetics Inc. and helped me choose my project. Working with Dr. Lee Bell is a marvelous learning experience since he always has the ability to make geophysical theories more understandable and interesting.

I would like to thank prof. Robert R. Stewart for his introduction to an excellent book and valuable suggestions on my thesis. That helped me to understand a number of important issues in tomography.

I am also grateful to BPZ Energy who gave me permission to use the Peru data for my research. Also, many thanks for Richard Verm, Oscar Garcia, Nestor Sanabria, Leidy Cruz, Chris Evert, and Lance Williams, my colleagues in Geokinetics. They taught me how to process the data.

Moreover, I would like to take this opportunity to express my appreciation to Weizhong Wang, Jing Chen, Steve Syme, and many others in GeoTomo. They gave me valuable advice in the use of their software when deriving near-surface velocity models.

Last but not least, thanks to my classmates Jiangbo Yu and Rui Zhou who helped on my coursework and had many valuable discussions and suggestions with me.

Without the people I mentioned above, I could never accomplish my thesis.

COMPARISON OF NEAR-SURFACE SEISMIC VELOCITY ESTIMATION METHODS WITH APPLICATION TO ON-SHORE PERU AND OFFSHORE MALAYSIA

An Abstract of a Thesis

Presented to

the Faculty of the Department of Earth and Atmospheric Sciences

University of Houston

In Partial Fulfillment

of the Requirements for the Degree

Master of Science

By

Hui Fan

August 2012

Abstract

The near-surface of the Earth often has rapidly varying velocity changes that distort the seismic images to a greater or lesser degree. Depending on the complexity of the velocity variations, a variety of methods have been developed to remove these distortions so that the deeper structures can be more properly imaged.

If the near-surface is characterized by layers, where the layers below the top layer have velocity variations that slowly vary laterally, an efficient and effective approach is the Refraction Delay-Time method (RDT). In this technique first-arrival picks are used to infer layer information in the shallow sub-surface. If the layer assumption fails and the velocity still generally increases with depth, then the First-Arrival Traveltime Tomography (FAT) technique may produce a better solution using the same or more extensively picked traveltime data. However, if one or more of the layers decreases in velocity with depth (the hidden layer problem), the interpretation of the traveltimes can be difficult. In such a situation Early-Arrival Waveform (EAT) Tomography may be able to handle the complexity at a greater computation cost.

These three techniques were applied to a 2D onshore example from Peru and a 2D Ocean Bottom Cable (OBC) dataset from Malaysia. In both cases the more sophisticated techniques of FAT and EAT produced superior results than the RDT technique. In addition, the EAT method gave further improvement to the land example.

Contents

List of Figures

Chapter 1

Introduction

1.1 Purpose and Scope

For this paper two 2D seismic datasets were considered: one an onshore project from Peru and the other an Ocean Bottom Cable (OBC) dataset from Malaysia. The Peru dataset's surface elevation gently varies from 67m to 80m, but has significant near-surface lateral velocity changes that substantially distort the seismic image of the deeper structures. The problem in the Malaysia OBC dataset is the presence of gas in the near-surface that has leaked from the hydrocarbon accumulation deeper in the section. The water bottom is quite flat, varying only from 55m to 58m in depth and the dominant structure below is a gently anticline whose image is distorted by the effects of the gas on the near-surface velocities.

In both cases three techniques were applied to the datasets to remove the distortion to the seismic image due to these velocity changes in the shallow part of the geologic section. In each case an estimate of the delay in the vertical arrival time due to these changes was calculated and applied to the seismic data to produce an image of the subsurface structures. The differing impact on the geologic structure produced from each of the methods is compared.

It is important to note that the statics compared in this paper are the long-period (longer than the cable length) statics. The velocity and short-period effects on the geologic structure are estimated and removed by first calculating the long period statics by refraction statics (described below), velocity estimation and application, then reflection statics estimation and application. The data are then stacked to see the time structure. The refraction estimate of the long period is then removed for the no-statics case and stacked again. Each of the other two methods is applied instead to see the change in the structure due to their various estimates of the near-surface velocity field. Two additional stacks are then produced to examine their structural time images.

If the near-surface is characterized by layers, where the layers below the top layer have velocity variations that slowly vary laterally, an efficient and effective approach is the Refraction Delay-Time method (RDT). In this technique first-arrival picks are used to infer layer information in the shallow sub-surface. If the layer assumption fails and the velocity still generally increases with depth, then the First-Arrival Traveltime Tomography (FAT) technique may produce a better solution using the same or more extensively picked traveltime data. However, if one or more of the layers decreases in velocity with depth (the"hidden layer" problem), the interpretation of the traveltimes can be difficult. In such a situation Early-Arrival Waveform (EAT) Tomography may be able to handle the complexity but at greater computation cost.

EAT introduces new assumptions on the input waveform data, but it does not require any simplifying assumptions on the velocity structure. For example, early-arrival waveforms (within about 200-300 ms time window following the first arrivals) are assumed acoustic and associated with the near-surface. In 2D data, 3D structure effects may be more influential on waveform techniques than on RDT or FAT.

In the application of the three techniques, the limitations of each method is explored, the near-surface and subsurface seismic images are produced, and the velocity fields derived from each method are compared. The resulting correction delays to the vertical traveltimes (statics) from each method are compared as well.

The two major software packages used in this work are TomoPlus v4.5, a refraction and tomographic statics analysis suite offered commercially by GeoTomo LLC, and the proprietary seismic data processing package Ethos (v3.4.0.b2) owned by Geokinetics, Inc. Their usage is described below.

The overall workflow to derive the correction statics is as follows:

1) The first-arrival energy (first break) is timed (picked). These are examined for correctness of the shot and receiver positions (geometry QC) and repositioned if necessary. For RDT only the first 2 to 3 layers are picked. For FAT and EAT further offsets may be included, depending on the depth of the velocity variations and the source-receiver distances (offsets) available in the dataset.

2) Perform the RDT, FAT, and EAT techniques for the 2D P-wave velocity model using the first-arrival picks to define the beginning time window of the early arrivals. These methods invert the picks (or the waveforms in the time window) to calculate a velocity model and subsequent statics to apply to the seismic data.

3) In the case of the EAT method, additional signal processing is applied and the time window of data is selected for the 2D waveform data inversion. The FAT velocity model is used as an initial estimate.

4) Results and comparisons of the near-surface solutions for RDT, FAT, and EAT are then shown. Steps 1 through 4 were accomplished using the TomoPlus software package.

5) Final stacks using the different statics solutions associated with the different models are then exhibited. This step involves importing the derived statics models from TomoPlus and applying them within Ethos. Other typical seismic processing steps such as the velocity corrections, noise editing, etc. are performed as well.

Steps 1 through 3 are of key importance to the methods and are further explained below.

First-Break Picking

First-break picking is the detection and timing ("picking") of the initial energy that travels from the seismic source to the receiver arrays. Naturally their arrival time increases with increasing distance the receivers are from the source ("offset"). This often can be difficult, especially with vibroseis sources which tend to produce "ringy" first arrival waveforms. Fortunately the land data analyzed here used dynamite as a source and the OBC was acquired with airguns. Impulsive sources such as these tend to yield fairly clean signals.

By the use of a workflow that involved pre-processing of the initial waveforms such as amplitude scaling, linear moveout, and muting, an automatic picking technique could be employed for most of the picking. The picks were then quality controlled both visually and with the use of display techniques demonstrated below.

Refraction Delay-Time Method (RDT)

This method is the most common technique used to solve a variety of near-surface velocity problems. It works on the assumption that the near-surface structure is layer-based without severe topography variations, and that the velocity changes in the layers beneath the first layer vary slowly laterally. By calculating the layer depth and velocities from refractor traveltimes, it yields good near-surface statics solutions if the layer assumption is valid.

First-Arrival Traveltime Tomography (FAT)

This is a non-linear inversion technique in which the velocity model is iteratively updated. The forward modeling utilizes a 2D wavefront ray tracing method, and the inversion technology applies a conjugate gradient method to perturb the velocity model until the differences between the predicted traveltimes and the measured traveltimes are as small as possible. It is particularly useful in the areas of rough topography and severe lateral velocity variation in the near-surface area, where velocity increases roughly with depth.

The workflow is as follows:

1) Pick the first arrival traveltimes of the shot records. The longer the offsets that can be reliably picked, the deeper the velocity model can be determined.

2) Construct an initial grid velocity model using either a simple 1D velocity as a function of depth or the refraction delay-time solution velocity.

3) Perform wavefront ray tracing for each shot location to calculate traveltimes.

4) Calculate the difference between these calculated traveltimes and the measured

traveltimes and invert the differences for each cell of the grid that the rays pass through to update the velocity. This is an iterative process where the velocity model is updated with each loop until the desired convergence is reached.

Early-Arrival Waveform Tomography (EAT)

The early-arrival waveform method is helpful in resolving hidden layers and complex velocity structures, and the computer capacity today is sufficient to deal with waveform tomography. A 2D time-domain waveform tomography method is employed which makes use of early-arrival seismic data. This includes direct waves, refractions, reflections, and diffractions as input data. The forward model calculates the 2D acoustic-wave in the time domain. The inversion uses a conjugate gradient method to generate the early-arrival waveform tomography solution. The workflow is as follows:

1) Apply initial seismic data signal processing. This includes balancing shot domain amplitudes, defining the early-arrival window, selecting an offset range, band pass filtering, muting noise, etc. In this procedure, care must be taken that the mute zones leave enough information to define detailed near-surface geologic structure. Including too much data can lead to very long computer runtimes.

2) A source wavelet from the seismic data is extracted to provide the waveform used during the iterations. A Ricker wavelet with a bandwidth representative of the early arrival data may also be used.

3) The first-arrival traveltime tomography velocity is used as an initial model and the iteration loops are then run.

4) The intermediate and final datums are then defined and the statics are calculated from the resulting velocity field.

1.2 Previous Studies

There are several techniques to solve near-surface velocity problems. Among these are: 1) refraction delay-time solution (Gardner, 1939; Hagedoorn, 1959; Lawton, 1989), 2) first-arrival traveltime tomography (Nolet, 1987; Lutter et al., 1990; Aldridge and Oldenburg, 1992; Ammon and Vidale, 1993; Nemeth et al., 1997; Zhang and Toksoz, 1998 and many others), 3) early-arrival traveltime tomography (Gauthier et al, 1986; Luo and Schuster, 1991; Sheng, 2006; Chaiwood, 2008 and any others), and 4) full-waveform tomography (Tarantola, 1984; Shipp and Singh, 2002), to name a few.

All traveltime methods assume certain types of velocity structures, but the data (traveltimes) are very reliable. On the other hand, waveform tomography does not assume a velocity structure, but does makes significant assumptions on the waveform.

Refraction Delay-Time solution (RDT) is an efficient conventional approach for the following reasons:

1. It builds the model directly by calculating the velocity and depth from traveltimes.

2. It can resolve high vertical velocity contrasts.

3. It provides good solutions in simple layered near-surface situations.

However, it fails in the presence of hidden layers. The hidden layer problem occurs when the velocity of one or more layers is less that the layer above it. According to Snell's law, if the lower layer velocity is higher than the upper layer velocity, it will generate refractions, i.e., head waves, when the incident angle reaches critical angle. There will not be a refraction generated in a hidden layer because the velocity in the upper layer is higher than those in the layer below and critical angle is not achieved.

RDT is a simple layer based model, so it does not represent geologic situations like rough topography and severe lateral velocity variations in the layers below the first layer.

Another issue is that if there is not a persistent refractor along the line due to perhaps regional dip and the refractor outcropping, significant interruption of the refractor due to thrusting of the deeper structures or significant near-surface channeling the method fails. In these cases first-arrival tomography work well.

Tomography is derived from the Greek for "section drawing". It refers to imaging by sections or sectioning, through the use of any kind of penetrating wave. Tomography is a method for finding the velocity and reflectivity distribution from a multitude of observations using combinations of source and receiver locations (Sheriff, 2002). Among these methods, FAT has long been considered the appropriate and standard geophysical tool due to its cost efficiency and ability to provide accurate velocity model estimates in most conditions (Zhu et al., 1992; Zelt et al., 2006). It utilizes the ray theory and inverts first arrivals of seismic waves to generate a velocity model. During the forward ray tracing procedure, FAT applies the Graph method by Moser (1991) and it outputs calculated traveltimes and athe ray paths used for calculating the difference between model traveltimes and picked first arrivals. It then inverts the difference back to perturbations in the velocity model. During the inversion, a conjugate gradient method is used to minimize a non-linear objective function of data misfit to update the new velocity model. It calculates iteratively until a minimum is attained. A more detailed description of the method may be found in Zhang and Toksoz (1998).

FAT does not need assumptions of simple geological structures, as for example layers and stable refractors. But it does assume velocity generally increases with depth like any other traveltime method. This method can resolve the challenges of complex near-surface structures, such as rough topography and strong lateral velocity variations.

Though FAT is an excellent method for dealing with the distortion caused by many near-surface velocity variations, it still has a limitations. Accurate picking and interpretation of first arrivals is essential in the calculation of realistic models. Mis-picking can introduce velocity errors and thus statics errors. The hidden layer problem is particularly difficult to accurately interpret.

Early-Arrival Waveform Tomography, which utilizes the events that arrive within a few cycles of the first arrivals (Sheng et al., 2006; Zhang and Zhang, 2011) has no such limitations, but imposes some assumptions on the waveform data. EAT contains not only more seismic information, but also has a range of wavelengths. It also contains fewer local minima so convergence is more reliable and faster.

EAT estimates the velocity distribution by minimizing the waveform misfit between predicted and observed early arrivals. It fits the early arrivals in the seismic data, including the direct wave, refractions, diffractions, and reflections.

In the forward modeling phase, it applies a finite-difference method to solve the 2D acoustic wave-equation and generate synthetic data in the initial or updated model. In the time domain a conjugate gradient inversion technique is iteratively performed to minimize the least-squares difference between the synthetic and real data.

Significant efforts have been made to develop EAT to resolve complicated situations where RDT and FAT fail. The results on the SEG foothill model show that EAT often provides a much more robust velocity estimate than FAT when near-surface velocities vary significantly (He et al., 2011).

1.3 Organization of Thesis

This thesis focuses on different methods to remove the distortion due to near-surface velocity variations. Among these are the conventional Refraction Delay-Time solution, the First-Arrival Traveltime Tomography technique, and the Early-Arrival Waveform Tomography. Chapter 1 introduced the purpose and scope for the thesis. It also described previous work on the different methods. In chapter 2, detailed explanations are given in for the three methodologies. The geologic background of area where the 2D seismic data from Peru is introduced, along with the acquisition methodology is contained in Chapter 3. The procedure for calculating statics for this project by each of the three methods is then described in detail. In chapter 4, the geology and seismic acquisition of the 2D OBC data from Malaysia is described. Again the three methodologies are applied to derive the statics. Chapter 5 presents the comparison of the calculated velocity models, statics and stack results derived from different techniques for these two cases. Finally, the conclusions are contained in Chapter 6.

Chapter 2

NEAR-SURFACE IMAGING METHODOLOGIES

2.1 Refraction Delay-Time Solution (RDT)

The refraction delay-time method is a conventional refraction statics correction technique that uses the traveltimes of critically refracted seismic energy to compute the depth and velocity structure of near-surface layers. It assumes the near-surface structure is simple and layer based. It neither has severe topography variations nor has rapid lateral velocity variation in layers beneath the near-surface weathering layer. It resolves intermediate and long-wavelength weathering static anomalies that cannot be handled by residual statics corrections.

The overall workflow to derive the correction statics is as follows:

First of all, the first-arrival energy (first break) needs to be picked. Normally, only the first 2 to 3 layers are picked. Moreover, these are examined for correctness of the geometry QC and repositioned if necessary. Furthermore, delay-time branches are chosen and RDT velocity model is to be drived. Finally, calcualte the statics after defining intermediate datum and final datum.

The specific method used in this thesis was developed by Lawton (1989). This method can indirectly estimate intercept time and bedrock velocity using the first breaks. It uses the multiplicity of first-break data available in multi-fold reflection surveys to determine the number of refractors present and to calculate statistically robust delayed times and refractor velocities. It mitigates the ambiguity in the interpretation of traveltime-distance graphs caused by the presence of topography or structure on the refractor.

Figure 2.1 is a two-layer model with one layer over half a space. The first layer can be considered as the weathering layer with an undulating base. It shows three raypaths associated with shot-receiver pairs AB, BC, and AC. Assuming that the delay times for a shotpoint and receiver at a common location are equal, we can easily derive the equations as below:

$$T_{AB} = T_A + \frac{AB}{v_2} + T_B \tag{2.1}$$

$$T_{BC} = T_C + \frac{BC}{v_2} + T_B \tag{2.2}$$

$$T_{AC} = T_A + \frac{AC}{v_2} + T_C \tag{2.3}$$

$$T_{AC} - T_{BC} = T_A - T_B + \frac{AB}{v_2} \tag{2.4}$$

$$T_{AB} - (T_{AC} - T_{BC}) = 2T_B \tag{2.5}$$

$$T_B = \frac{1}{2}(T_{AB} + T_{BC} - T_{AC}) \tag{2.6}$$

$$T_A = \frac{Z_A \cos\theta}{v_1} \tag{2.7}$$

$$T_B = \frac{Z_B \cos\theta}{v_1} \tag{2.8}$$

$$T_C = \frac{Z_C \cos\theta}{v_1} \tag{2.9}$$

$$\theta_1 = \arcsin\frac{v_1}{v_2} \tag{2.10}$$

where T_{AB}, T_{AC} and T_{BC} represent first-arrival traveltimes from source to receiver. T_A T_B T_C are delayed traveltime for A, B, and C, respectively. θ is incident angle, Z_A, Z_B and Z_C are the depth from shot/receiver to the refractor, velocities in the two layers are v_1 and v_2.

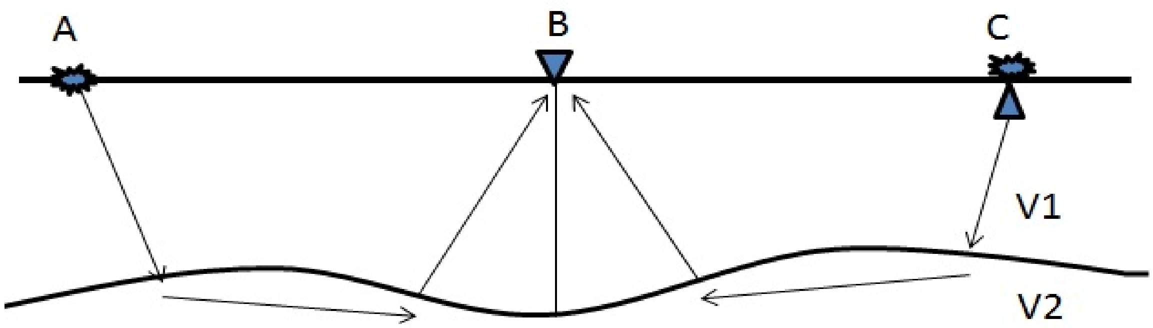

Figure 2.1: Two-Layer Refraction Delay-time Model. T_{AB}, T_{AC} and T_{BC} represent first-arrival traveltimes from source to receiver. T_A T_B T_C are delayed traveltime for A, B, and C, respectively. v_1 and v_2 are velocities in two layers.

Delay times for deeper refractors can be computed in an identical manner by using further offset from the shotpoints. In the general case for refractor n, the delayed time can be expressed as

$$T_{AB_n} = T_{A_n} + \frac{AB}{v_{n+1}} + T_{B_n} \tag{2.11}$$

The depth of the layer can be computed from the equation

$$T_{A_n} = \sum_{i=1}^{n} \frac{Z_{A_i} \cos\theta_i}{v_i} \tag{2.12}$$

where

$$\theta_i = \arcsin \frac{v_i}{v_{i+1}} \tag{2.13}$$

Though this conventional approach can resolve high vertical-velocity contrasts and also provide high resolution solutions in simple near-surface situations, it does have the following limitations:

1) Since it utilizes the refractions, it can't account for hidden layers. Refractions aren't generated if the velocities in the upper layer are higher than those in the layer below.

2) The method assumes a simple layer-based model. Departures from this due to complex near-surface structures like rough topography and severe lateral velocity variations degrade the results.

3) The refractors need to be continuously present throughout the dataset. If they disappear due outcropping to the surface or get interrupted due to valley fill then it becomes very difficult to apply this technique.

2.2 First-Arrival Traveltime Tomography (FAT)

This is an iterative method that utilizes a starting model and first-arrival traveltimes. The forward modeling uses 2D wavefront raytracing, and the differences between the predicted times and the first-arrival picks are minimized via a conjugate gradient inversion technique. The velocity model is updated with each iteration.

The workflow is as follows:

Initially, first arrival traveltimes or the"first break" in seismic data need to be picked. Typically most or all of the source-receiver offsets are picked, whereas in RDT only a few refractors are interpreted. The first arrivals are direct waves, refractions or diving-waves. Generally the picking isn't too difficult, especially for airgun or dynamite sources. However a vibroseis source can be hard to interpret due to the emergent nature of the first arrivals after correlation. On land ambient noise can also make the interpretation difficult. Finally if the near-surface is structurally complicated or there are significant lateral velocity changes, or hidden layers are present causing discontinuities, then the picking can be challenging.

After picking the first breaks, an initial model with a simple velocity increasing with depth is constructed. The forward modeling utilizes wavefront raytracing (graph method, Moser, 1991) to output calculated traveltimes and ray paths. The difference between the calculated traveltimes and picked first arrivals are then used to define the misfit function:

$$\epsilon = \frac{1}{2}\sum_i (t_i^{obs} - t_i^{cal})^2 \tag{2.14}$$

Where t_i^{obs} is the observed traveltime picked from seismic data; t_i^{cal} is the predicated traveltime calculated from forward modeling; ϵ is the misfit between them; the summation is over the i_{th} raypaths. During the inversion process, the traveltime tomography applies the Conjugate Gradient method.

The j_{th} gradient of the γ_j misfit function is defined as:

$$\gamma_j = \frac{\delta \epsilon}{\delta s_j} = \sum_i \delta t_i \frac{\delta t_i}{\delta s_j} = \sum \delta t_i l_{ij} \tag{2.15}$$

where δs_j is the slowness in the j_{th} cell, l_{ij} is the ray path propagating the j_{th} cell, δt_i is the traveltime residual.

A series of iterations is performed to minimize the nonlinear objective function of data misfit term. The velocity model is updated and a new model is output during each iteration until a minimum error is reached.

FAT has long been considered the appropriate and standard geophysical tool due to its cost efficiency and ability to provide accurate velocity model results in most of conditions (Zhu et al., 1992; Zelt et al., 2006). There is no need of assumptions as layers based and continuous refractors. This method can robustly handle the challenges of complex near-surface structures such as rough topography or severe lateral velocity variations.

Though FAT can offer accurate velocity models with details in most of the cases, it still has limitations:

1. The discontinuities caused by hidden layers make the interpretation of the first arrivals very difficult.

2. The method is sensitive to accurate interpretation of first arrivals. Consistent bad picks can introduce artificial structures.

Under these circumstances, FAT can be used to supply a good initial model to a more robust and sophisticated geophysical method such as early-arrival waveform tomography.

2.3 Early-Arrival Waveform Tomography (EAT)

EAT is a nonlinear waveform-tomography method for estimating 2D near-surface velocity distribution. It minimizes the waveform misfit between the predicted and observed early arrivals in seismograms, including direct wave, refractions, diving-waves, diffractions, and reflections.

The workflow is as follows:

1. Apply initial seismic data signal processing.

2. Extract a source wavelet from data or using Ricker wavelet.

3. Use first-arrival traveltime tomography velocity model as initial model, perform inversion.

4. Define intermediate and final datum.

5. Calculate statics.

EAT utilizes the 2D acoustic wave-equation to perform forward modeling calculation,

$$\frac{1}{K(r)}\frac{\partial^2 p(r,t|r_s)}{\partial t^2} - \nabla \bullet [\frac{1}{\rho(r)}\nabla p(r,t|r_s)] = s(r,t|r_s) \tag{2.16}$$

where K(r) and $\rho(r)$ are the bulk modulus and density functions, $p(r,t|r_s)$ stands for the pressure at time t in the receiver r related to a source at r_s, and $s(r,t|r_s)$ is the source function. These parameters can be used to generate synthetic seismograms by a fourth-order, finite-difference method (Levander, 1988, Sheng, 2006).

The inversion is performed in the time domain and is based on a nonlinear preconditioned conjugate gradient optimization algorithm to minimize the least-square difference between calculated data and observed data.

The objective function which is to be minimized through tomographic inversion is given by:

$$\Phi = \|(d - G(m)\|^2 + \tau\|L(m)\|^2 \tag{2.17}$$

where d is the observed early arrival waveform data, m is model parameters, G(m) is the calculated early arrival waveform from forward modeling, L is the Laplacian operator, and τ is the smoothing control. The early-arrival data is typically a window of the first 200ms to 300ms of data below the first-arrival data and includes much or all of the offsets.

The preconditioning term **P** is the diagonal inverse to the Hessian and the velocity model is updated recursively using the conjugate directions defined by

$$\mathbf{d}_k = -\mathbf{P}_k\mathbf{g}_k + \beta_k\mathbf{d}_{k-1} \tag{2.18}$$

for iterations k=1,2,...,k_{max}. The velocity model is updated by

$$c_{k+1}(x) = c_k(x) + \lambda_k d_k(x) \tag{2.19}$$

where λ_k is the step length, d={d(x) for all image points x in the model}, and g = {g(x) for all image points x in the model}. The misfit gradient $\mathbf{g}_k$ at iteration k is given by $\mathbf{g}_k(x)=\frac{\partial\phi_k}{\partial c_k(x)}$ for all image points x. The parameter β_k is computed by the Polak-Ribire formula (Nocedal and Wright, 1999). The initial model is supplied by FAT in order to obtain accurate long wavelength estimate of the velocity model (Sheng, 2006, Zhang, 2010). The velocity model is updated and a new model is output iteratively until it achieves a minimum.

EAT does not assume simple geology but does assume the data field is acoustic. As long as this assumption is valid, the method can resolve very complex near-surface structures such as hidden layers, severe lateral velocity variations, high velocity thrusts to the near-surface and so on.

Though EAT can offer accurate velocity models with details in most of the cases, it still suffers from limitations besides the acoustic precondition:

1. It requires a good starting model.
2. It's very computationally intensive.
3. The inversion result is sensitive to the estimated source wavelet.

Chapter 3

SEISMIC DATA PROCESSING METHODS FOR PERU DATA

3.1 Site Geology

The area in this study is located in Lancones Basin of Peru (Figure 3.1) in South America. There is nearby oil production from the Portachuelo Oil Field, the San Pedro Oil Field (offshore) and the La Isla Oil Field.

The Lancones Basin is located in northwestern Peru and southwestern Ecuador. It is an extensional basin opened between a volcanic arc to the east and southeast and the Paleozoic Amothape-Tahuin mass to the west and northwest (Figure 3.2). The basin is a tectonically active Albian-Conicacian trough infilled mainly by turbidities. The sediments of the basin constitute the sedimentary cover of the Amotape-Tahuin Massif toward the west and volcanic arc rocks and related volcaniclastic sediments of probably Albian age toward the east. They are unconformably overlain by the

Figure 3.1: Location of processed 2D data line.

NNE-trending Paita-Yunguillaforearc basin (Jaillardetal, 1999). Channel cutting and slow-velocity infill on the scale of several km frequently occurs in the area. The stratigraphic model is show in Figure 3.3.

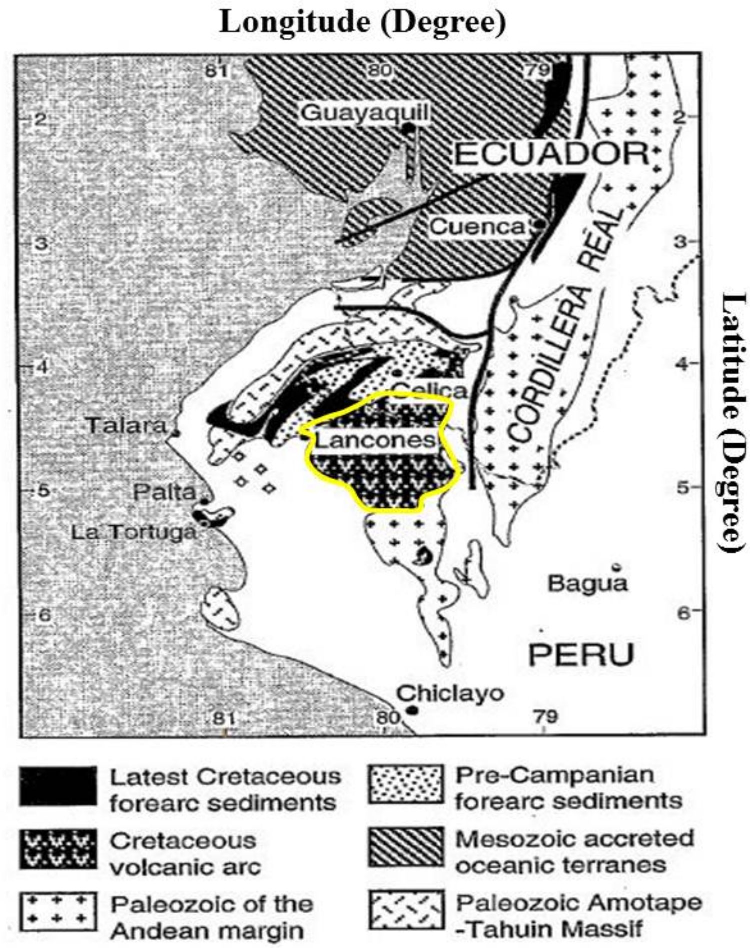

Figure 3.2: Location sketch map of the Lacones Basin (Jaillard et al., 1999). The study line is inside yellow area.

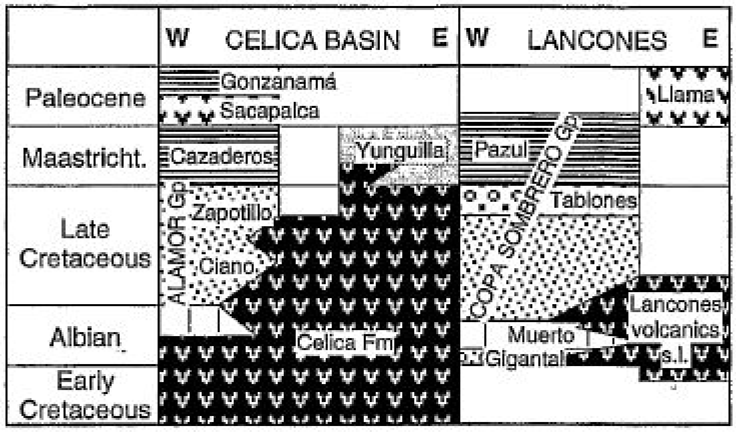

Figure 3.3: Stratigraphic models of the Lacones model (Jaillard et al., 1999).

3.2 Seismic Surveys

The survey area is located onshore in block XXII of northwest Peru. The study data set includes one 2D line (see Figure 3.4). The shot line is about 12 kilometers in length and the receiver line is around 15 kilometers long. The record length is 4 seconds and sample rate is 4ms. There are 264 shots and 1053 receivers in this 2D survey with a 45m shot interval and 15m receiver interval (see Figure 3.5). The topography is fairly flat; the shot and receiver elevation only vary from 67 meters to 80 meters as can be seen in Figure 3.6. Lateral axis is X coordinate in meter, vertical axis is the depth which assumes that above sea level is negtive.

3.3 Seismic Data Processing Method

3.3.1 Refraction Delay-Time Solution (RDT)

Before applying RDT, we need to follow the steps as below:

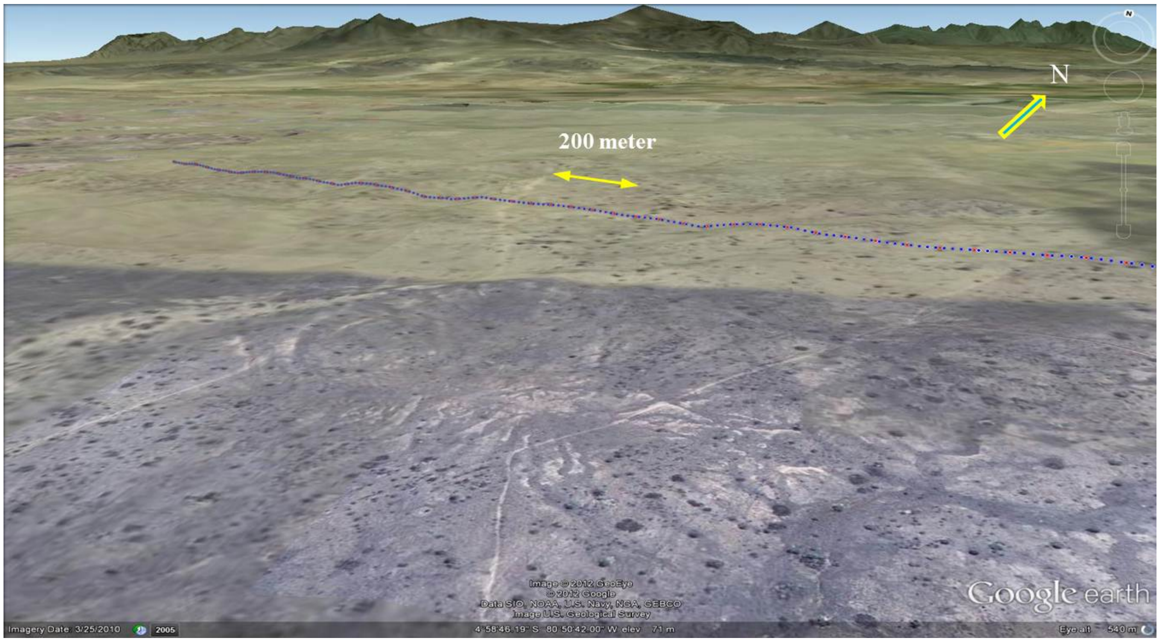

Figure 3.4: 2D Seismic survey map.

1 Pick first arrivals, QC the geometry and the first breaks.

2 QC first breaks again, choose delay-time refractor.

3 Derive RDT velocity model and define intermediate and final datums.

4 Calculate statics.

3.3.1.1 Picking and Quality Control

First-break Picking

Picking the first arrivals in this dataset was straightforward due to the dynamite source. The first breaks are easily identified as shown in Figure 3.7, even for very near offsets. Besides employing the automatic picking, the tracker was used to manually refine the bad first breaks in common shot gathers.

Total Number of Shots: 264
First Shot ID: 19855
Last Shot ID: 23975
Estimated Shot Interval: 46.2
Minimum Channels per Shot: 439
Maximum Channels per Shot: 880
Shot X Coordinate Range: 515809.0 to 527527.0
Shot Y Coordinate Range: 9445082.0 to 9451021.0
Shot Elevation Range: 80.0 to 67.0
Shot Depth Range: 0.0 to 0.0

Total Number of Receiver Stations: 1053
First Receiver ID: 1985
Last Receiver ID: 3037
Estimated Receiver Interval: 12.2
Receiver X Coordinate Range: 515803.0 to 527532.0
Receiver Y Coordinate Range: 9445079.0 to 9451024.0
Receiver Elevation Range: 80.0 to 66.0

Number of Offsets: 944
Offset Interval: 12.0
Offset Range: -5824.0 to 5501.0
Minimum Channels per Offset: 1
Maximum Channels per Offset: 406

Shot sequence is not in order
Receiver sequence order from minimum X to maximum X
Receiver sequence order from maximum Y to minimum Y

Total Number of Traces: 183602

Measurement System: meter

Shot ID : Unique
Receiver ID : Unique

Shot ID : Positive
Receiver ID : Positive

Figure 3.5: Geometry information.

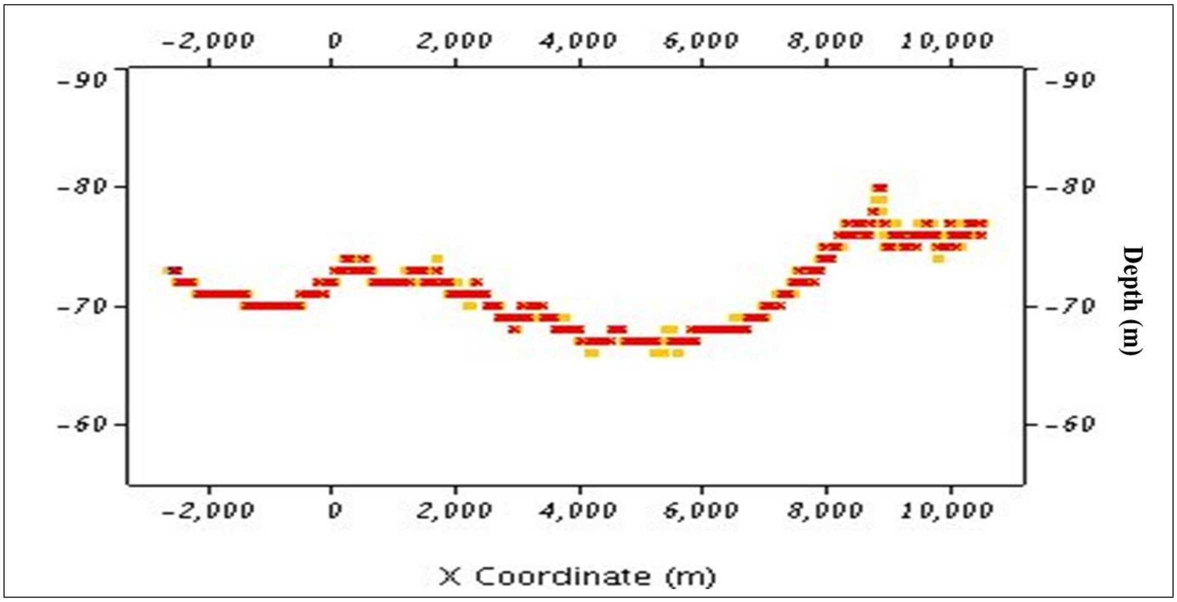

Figure 3.6: Shot and receiver elevation plot. Lateral axis is X coordinate in meter, vertical axis is the depth which assumes that above sea level is negtive.

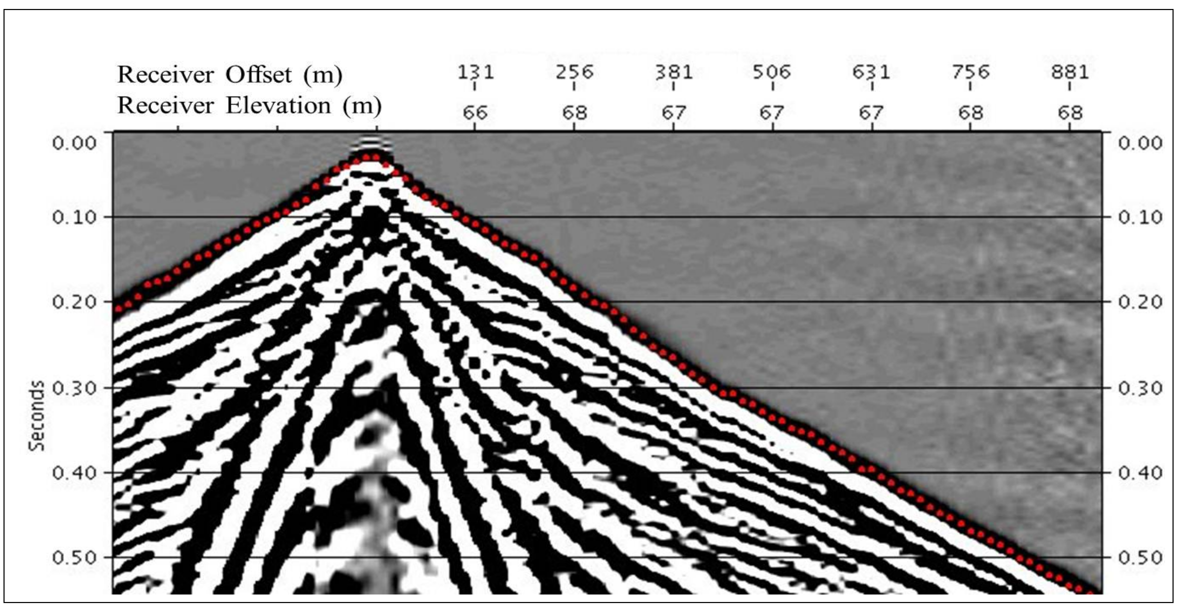

Figure 3.7: Shot gather 3 with picks. Dynamite source makes it easier to pick first breaks automatically. Red dots are user picks.

QC Geometry and Refine Bad Picks

After picking the first breaks, we use the Reciprocal Error QC plot to check the picks and geometry for the first time. In theory, the reciprocity principal states that interchanging of the shot and receiver locations does not alter the traveltimes. The reciprocal error is the difference between the picked first arrival from the source to the receiver and the receiver to the source. In general, the maximum reciprocal error should be less than 20ms, and the average of the reciprocal errors for all shots should be around 10ms. However, in practice, errors are often caused by geometry or picking error.

In this case, the utility indicates the reciprocal error range for all the first breaks and how they are distributed as can be seen in Figure 3.8. The X and Y coordinates indicate the geometry spread in meters. The color coding means different Reciprocal Error and distributions in the picked geometry line, varying from 2ms in blue to 33ms in pink. There are 264 shots totally and the maximum Reciprocal Error of picking is 33 ms. Shots with larger Reciprocal Error errors stand out and offer an opportunity to refine the first break picks shot by shot. Mostly, the shots reciprocal error vary from 2ms in blue to 10ms in green. Moreover in Figure 3.9, besides the inform of the maximum Reciprocal Error for picking is 33 ms, it points out that there are 9 shots with Reciprocal Error bigger than 15 ms. These shots can then be examined for bad picks. If the error cannot be reduced by further refining the picks then geometry errors may be indicated.

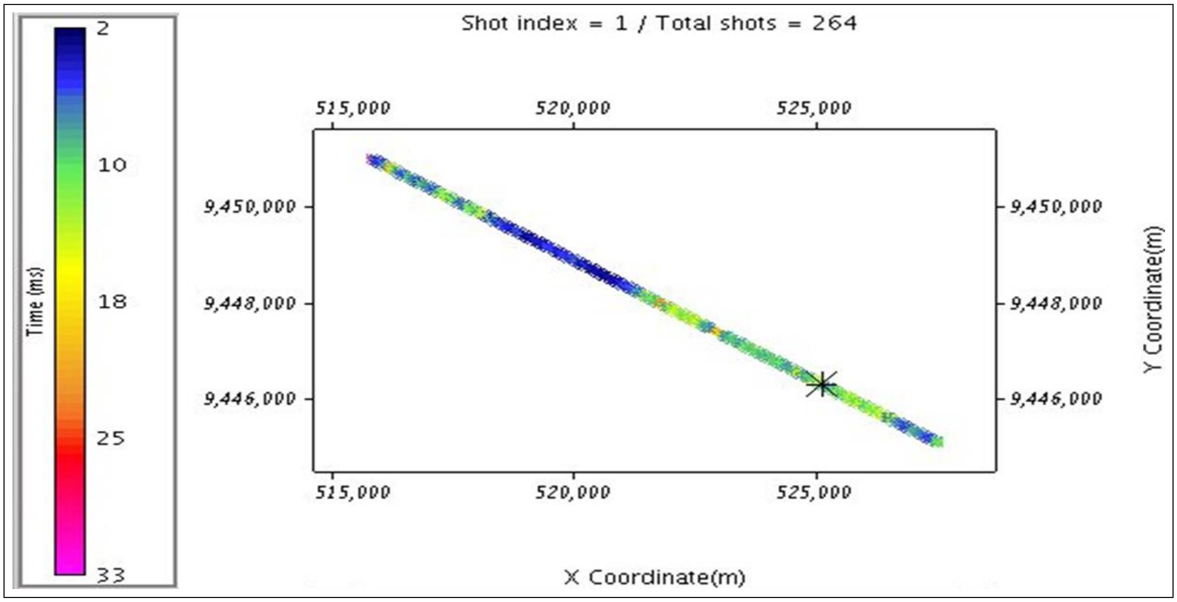

Figure 3.8: QC Geometry and first breaks. The maximum Reciprocal Error for picking is 33 ms, and different color stands for different Reciprocal Error and distributions in the geometry line.

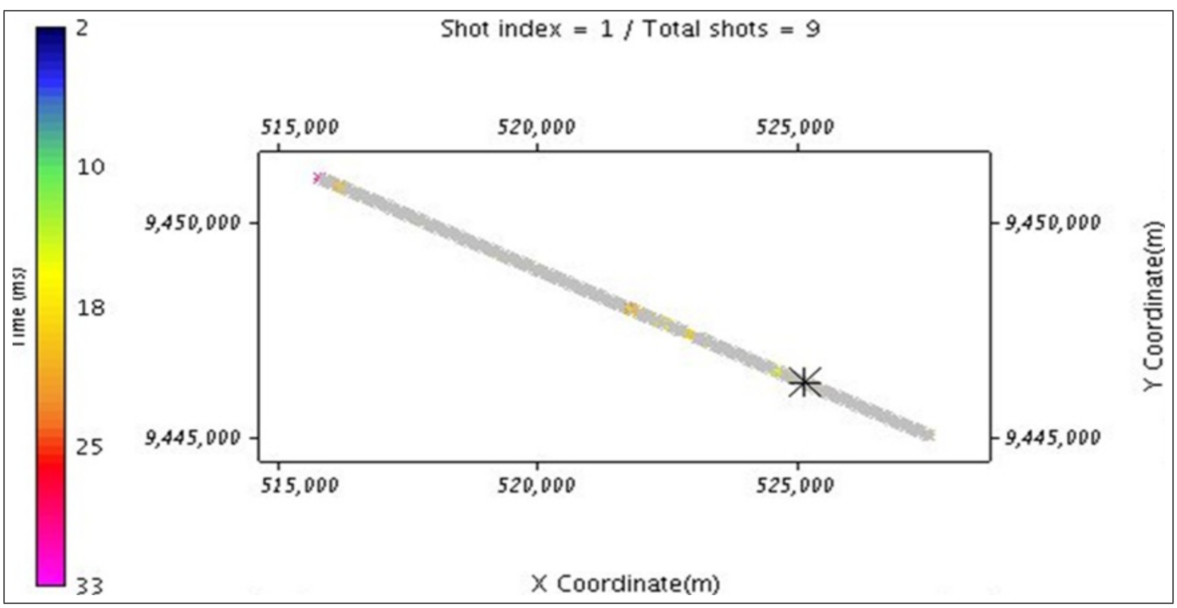

Figure 3.9: QC Geometry and first breaks. Besides the inform of the maximum Reciprocal Error for picking is 33 ms, it points out that there are 9 shots with Reciprocal Error bigger than 15 ms.

3.3.1.2 QC First Breaks Again and the Selection of the RDT Branch

In Figure 3.10, the plot of Reciprocal Error spread for all the shots is exhibited. The X coordinate displays the line geomery spread in x direction in meters. The Y axis stands for reciprocal error in ms. Each asterisk represents the reciprocal error for each shot. In the display shown here, most shots have a reciprocal error below 10ms. Placing the cursor on a shot with high reciprocal error identifies the shot number and allows the user to go back and examine it.

Figure 3.11 shows a plot of the first arrival times of all shots versus source-receiver distance (offset). This allows one to choose the refractors to employ in the solution. To identify the refractors more clearly, a 2500m/s linear velocity shift has been applied to the pick times to flatten them, and three refractor branches have been selected as seen by the boxes on the plot.

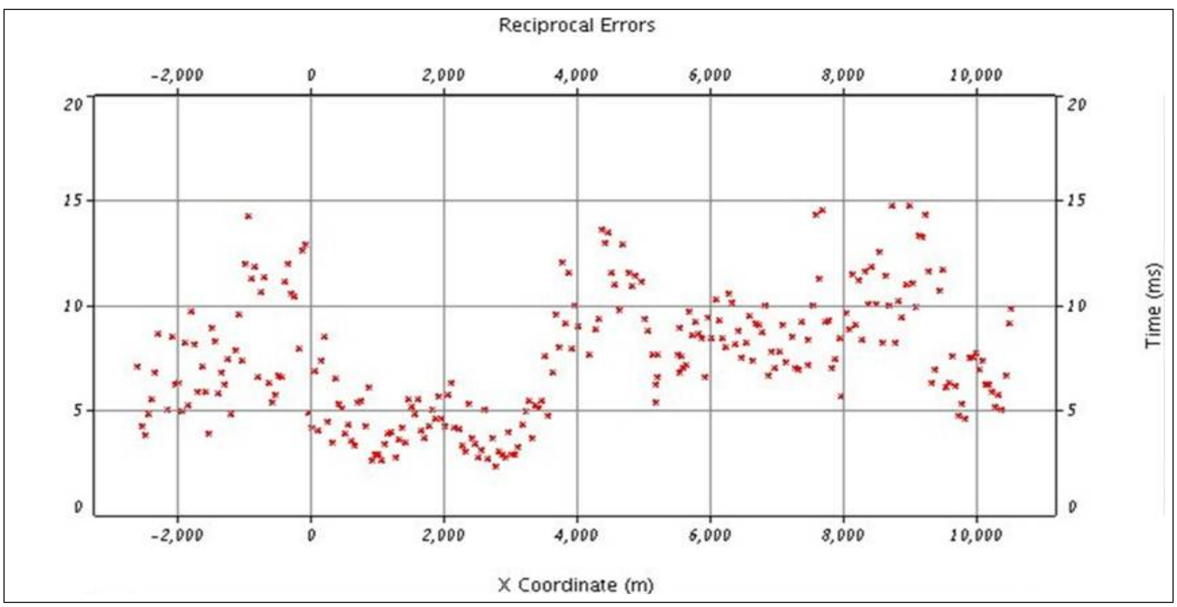

Figure 3.10: QC Geometry and first breaks again. It plots Reciprocal Error spread with all the shots. Each asterisk represents the reciprocal error for each shot.

Figure 3.11: Pick 3 branches of first breaks according to the refractors. To identify the refractors more clearly, a 2500m/s linear velocity shift has been applied to the pick times to flatten them.

3.3.1.3 Build RDT Velocity Model, Define Intermediate and Final Datum

After picking the overall refractor branches (in this case three), an RDT solution is performed to derive a velocity model and define intermediate and final datum as can be seen in Figure 3.12. The X axis is the horizontal distance in meters and the vertical axis notes the depth in meters. The color bar presents the velocity spread from 800m/s in blue increasing to 3300m/s in pink. The top white line denotes the final datum which is 80 meters above the sea level and the intermediate datum which is beneath it is 100 meters below the sea level.

There are two reasons to define 80 meters as final datum: first, the shot and receiver elevation vary from 67 meters to 80 meters; second, the further processing would utilize 80 meters as final datum to be consistent with other seismic data in the area.

Considering the depth of the near-surface velocity anomalies (the high velocity and low velocity regions), 100 meters below the sea level was picked as intermediate datum. Consequently, the average of the velocities along the intermediate datum which is 2500m/s was used as replacement velocity.

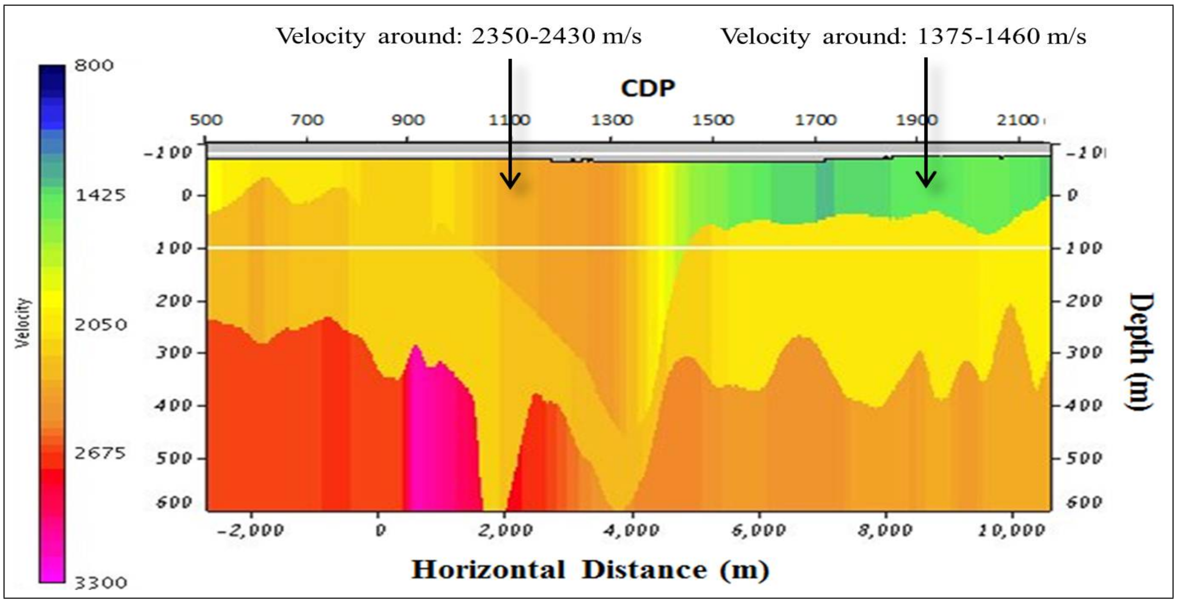

Figure 3.12: Three-Layer RDT velocity model. Two white lines are final datum on the top and intermediate datum at the bottom respectively.

3.3.1.4 RDT Statics

Using the above datums and the replacement velocity the statics were calculated and plotted in Figure 3.13. The X axis is the horizontal distance in meters. The vertical axis displays the calculated statics in ms. Red are shot statics and blue are receiver statics. The computation is applied in two steps: first, shots and receivers are moved down from topography to the intermediate datum using the velocity field derived from RDT method and associated with the near-surface area; second, they are moved up to the final datum using the replacement velocity.

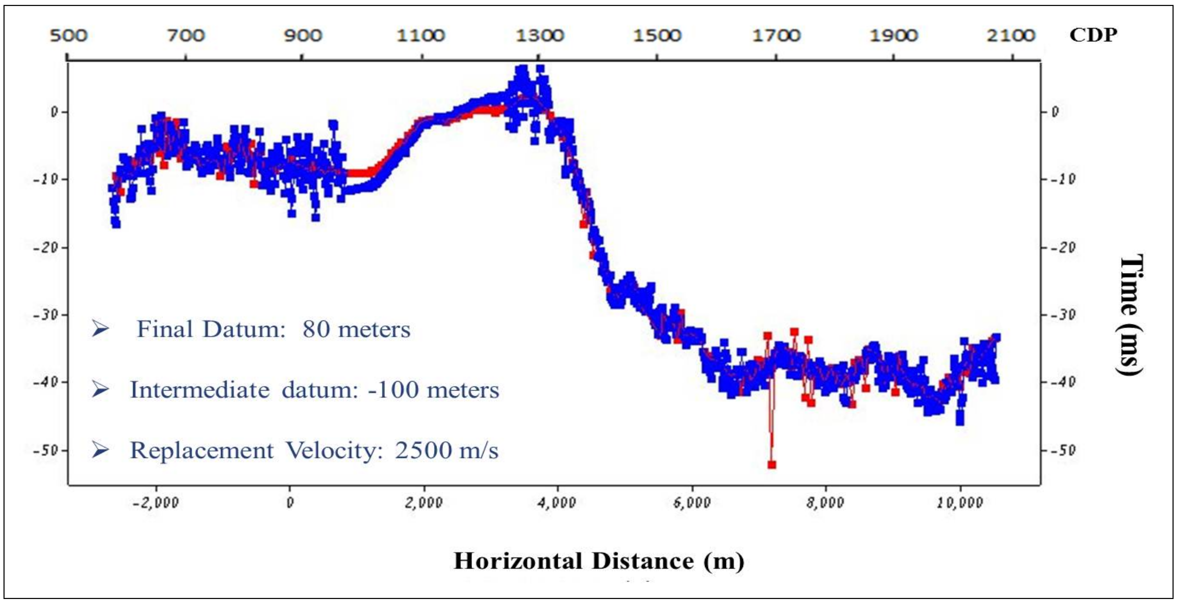

Figure 3.13: Delay-Time statics plot. Red are shots and blue are receivers.

3.3.2 First-Arrival Traveltime Tomography Solution (FAT)

3.3.2.1 FAT Velocity Model

With the RDT velocity model as initial estimate and performing first-arrival traveltime tomography inversion, iterations were run to update velocity model. Convergence was achieved after 20 iterations as can be seen Figure 3.14, and the final velocity model is exhibited in Figure 3.15. At the same time a ray density model has also been generated in Figure 3.16. We also utilize overlay the predicted first arrival picks with user picks to QC FAT solution (Figure 3.17 to 3.19). Figure 3.14

is the graphical display to indicate the misfit (Y axis) of all shots over 20 iterations (X axis). The convergence is quite stable after 8 iterations during the inversion.

Similar to Figure 3.12, Figure 3.15 is the final FAT velocity model derived from RDT as initial after 20 iterations inversion. Lateral axis and vertical axis indicate horizontal distance and the depth respectively in meters. Model grid size is 5m*5m. Color bar presents the same velocity range from 800m/s in blue to 3300m/s in pink. The two white lines are the intermediate datum and final datum. The high velocity zone varies from 2700 m/s to 3200 m/s, and the low velocity area spreads to a range of 850 m/s to 1300 m/s.

Figure 3.16 is the ray density associated with the velocity model. It has the same explanations of x and y axis but different meaning for color. The color bar in the model indicates the number of rays that pass through each grid cell. The model is deep enough so that the rays couldn't hit the bottom of the model. The velocity model is reliable to the depth where a sufficient number of rays penetrate.

As a QC, Figure 3.17 to 3.19 show the modeled travel times (blue) overlayed over the user picked travel times (red).

3.3.2.2 FAT Statics

We use final a flat datum 80 meters, an intermediate datum of -100 meters and a replacement velocity of 2500 m/s just as was done in the RDT solution to calculate the statics shown in Figure 3.20.

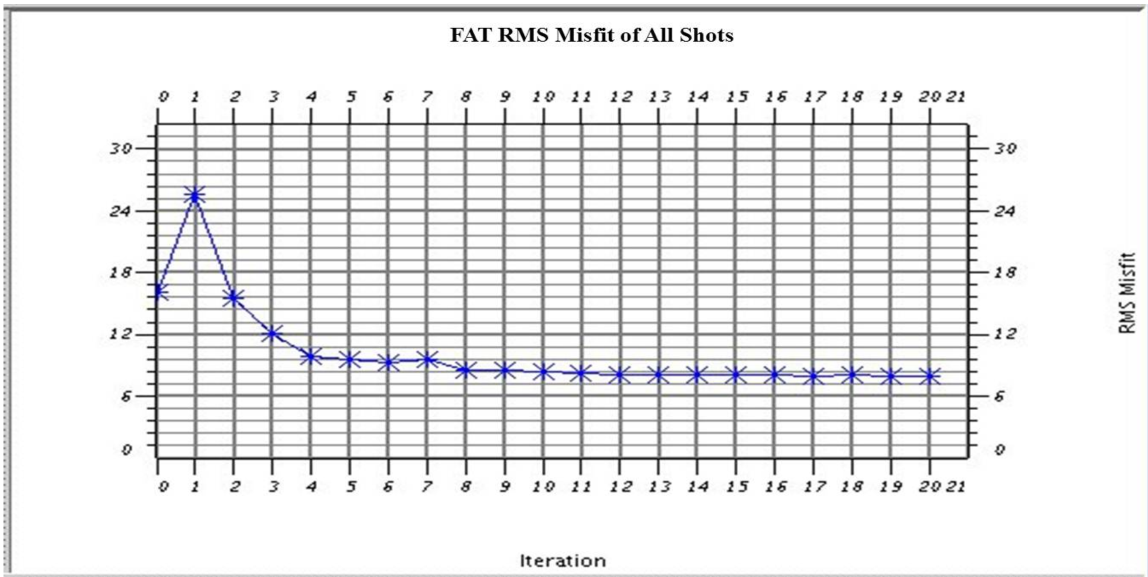

Figure 3.14: Tomographic inversion misfit versus iteration number.

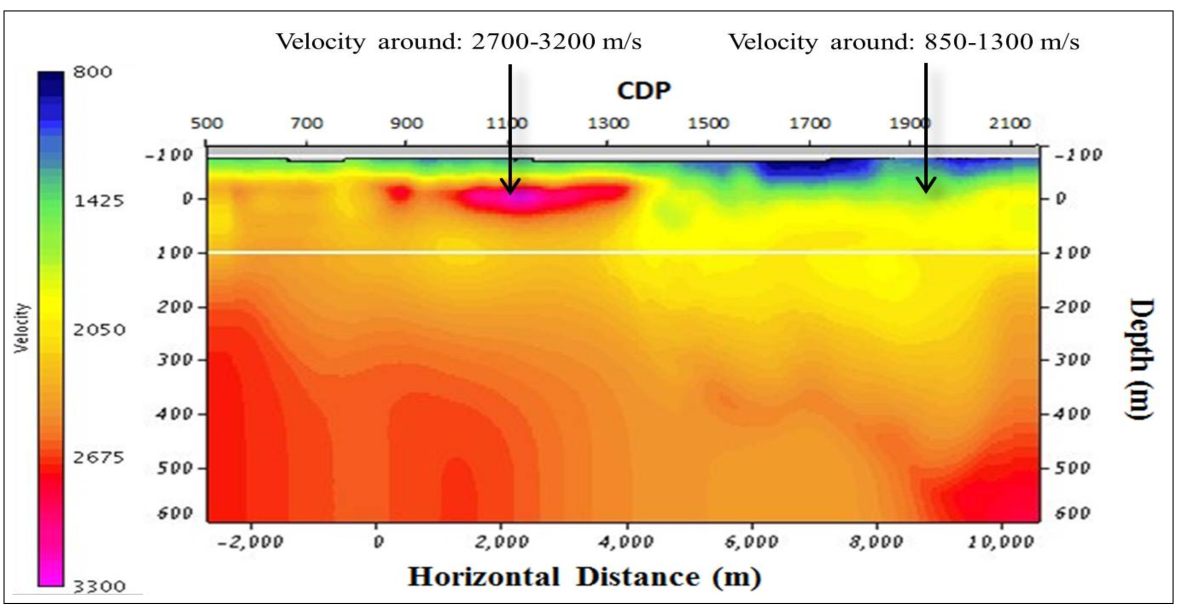

Figure 3.15: Final FAT velocity model inversed from delay-time model. Model grid size is 5m*5m. Two white lines are final datum on the top and intermediate datum at the bottom respectively.

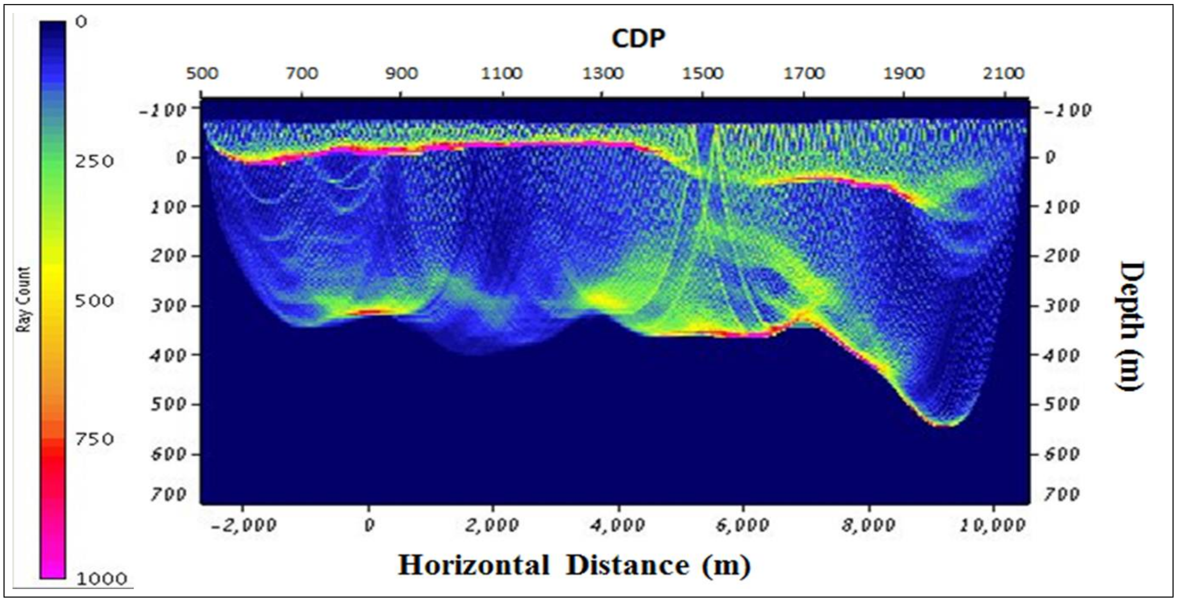

Figure 3.16: Ray density of final traveltime velocity model. Lateral axis and vertical axis indicate horizontal distance and the depth respectively in meters. The color bar in the model indicates the number of rays that pass through each grid cell.

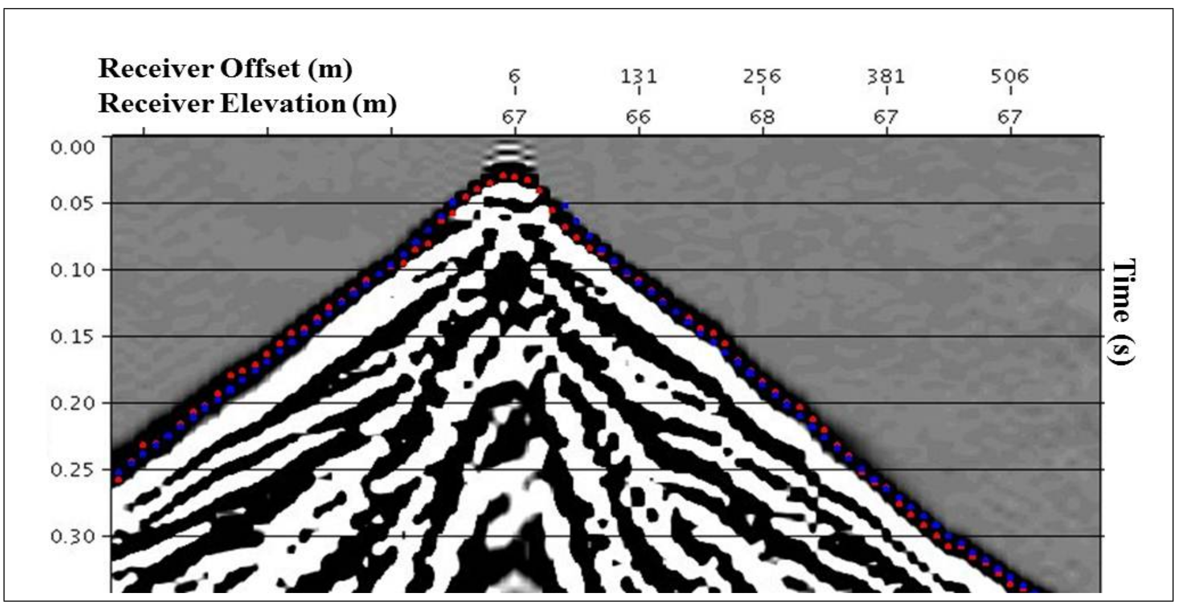

Figure 3.17: FAT overlay for shot 3: fitting the synthetic first arrivals in user picks. Blue are synthetic first breaks, red are observed first arrivals.

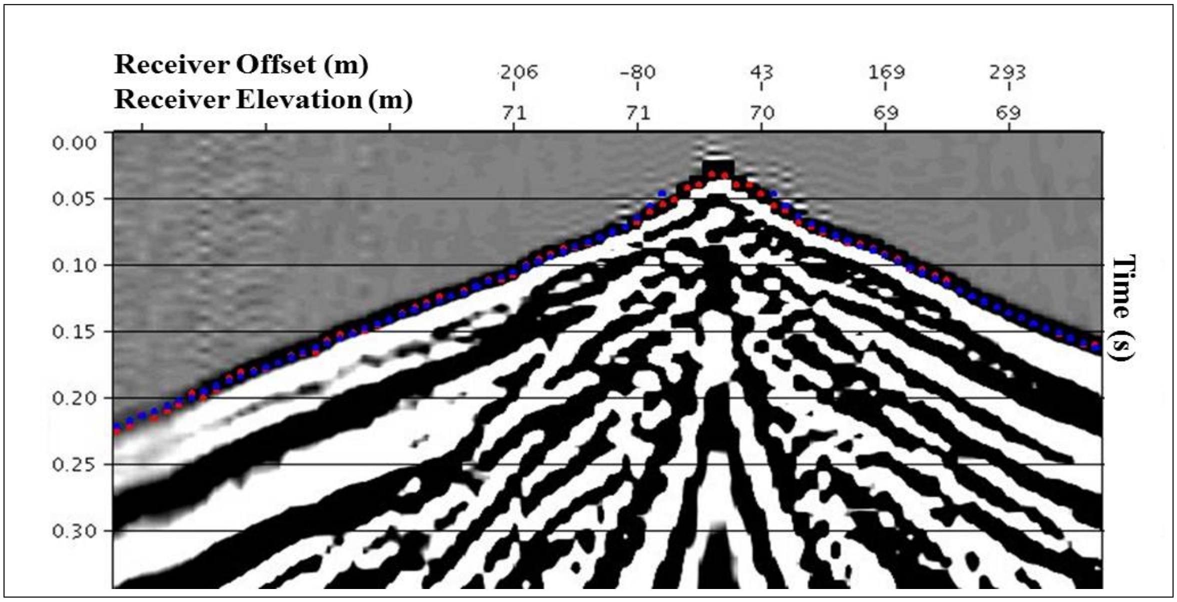

Figure 3.18: FAT overlay for shot 4: fitting the synthetic first arrivals in user picks. Blue are synthetic first breaks, red are observed first arrivals.

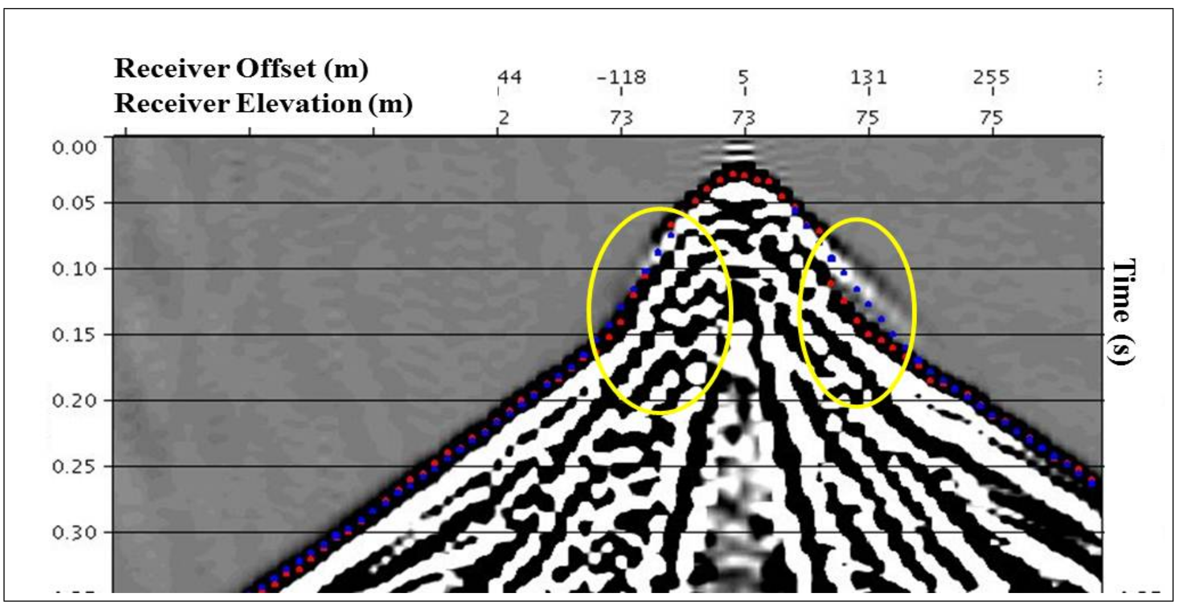

Figure 3.19: FAT overlay for shot 7: fitting the synthetic first arrivals in user picks. Blue are synthetic first breaks, red are observed first arrivals. Shingling due to velocity inversion (small hidden layer area).

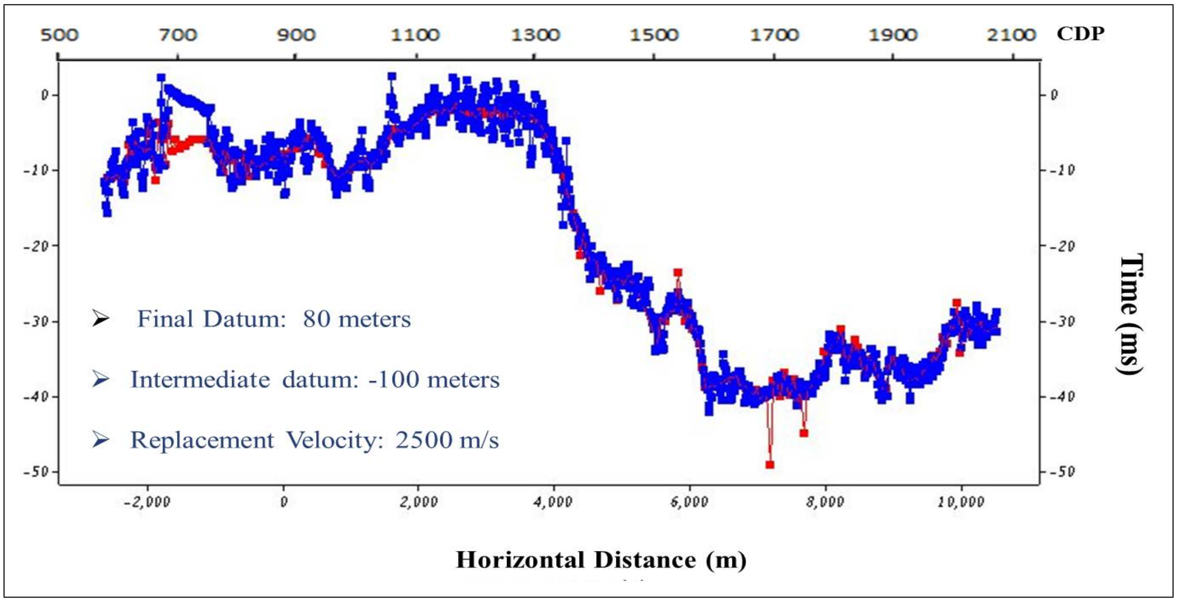

Figure 3.20: First-Arrival Traveltime Tomography statics. Red are shots and blue are receivers. The FAT and RDT statics are quite similar, both vary from -50ms to 5ms.

3.3.3 Early-Arrival Waveform Tomography (EAT) Solution

3.3.3.1 EAT Initial Seismic Data Signal Processing

Before using EAT, the seismic data is pre-processed to prepare for waveform tomography. The offset range is selected, band passed, a mute applied before the first arrivals to remove any pre-cursor noise and another mute is applied below the first arrivals to eliminate ground roll and limit the window to minimize the computation. Figures 3.21 to 3.25 show these steps. The spectrum variations before and after the processing are show in Figures 3.26 to 3.28. The color in Figures 3.26 to 3.28 represents the degree of amplitude/energy, varying from blue (weak) to pick (strong).

Taking a common shot gather as an example, Figures 3.21 plots how this original shot looks with low and high frequency noise (see Figures 3.26) after balancing.

Limiting the offset range (Figures 3.22) can decrease some noise as well as decreasing the computation time.

Applying a band pass filter as shown in Figures 3.23 reduces high frequency noises to avoid cycle-skipping in waveform inversion. For instance, if the initial input velocity model for inversion is too different from the true earth, the differences between the real data and modeled data will increase with each iteration. To address this problem, low frequency data are desired for waveform inversion since low frequency cycles are hardly skipped even with a poor starting model. Therefore band pass of 1-3-20-30 is applied to keep only the low frequency components of seismic data according to the spectrum of original data after balancing the amplictude.

To apply 2D acoustic forward modeling and improve inversion efficiency, limiting the seismic waveform window with muting precursor noise and ground roll noise is necessary (Figures 3.24 and Figures 3.25). The spectrum after mute is shown as Figures 3.28.

3.3.3.2 EAT Velocity Model

The first-arrival traveltime tomography velocity was used as an initial model and waveform tomography inversion was performed with the convergence show in Figure 3.29. 25 iterations were been completed in 5 hours and 6 minutes with 64 CPUs computational resources. After 19 iterations, the convergence became stable.

The final waveform velocity model is exhibited in Figure 3.30. An overlay of the predicted early arrivals from the model superimposed on shots 100, 230, and 240 can be seen in Figures 3.31 to 3.33.

3.3.3.3 EAT Statics

Again using the same intermediate datum, final datum, and replacement velocity as before, the EAT statics are calculated and displayed in Figure 3.34.

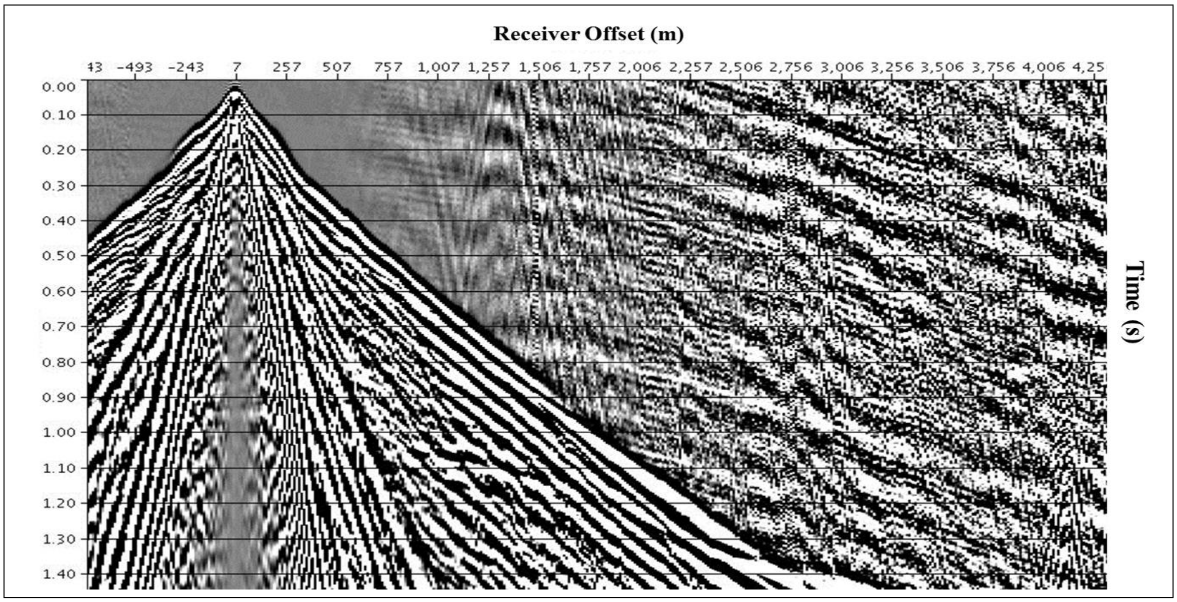

Figure 3.21: Initial seismic data signal processing: balance the amplictude of original data.

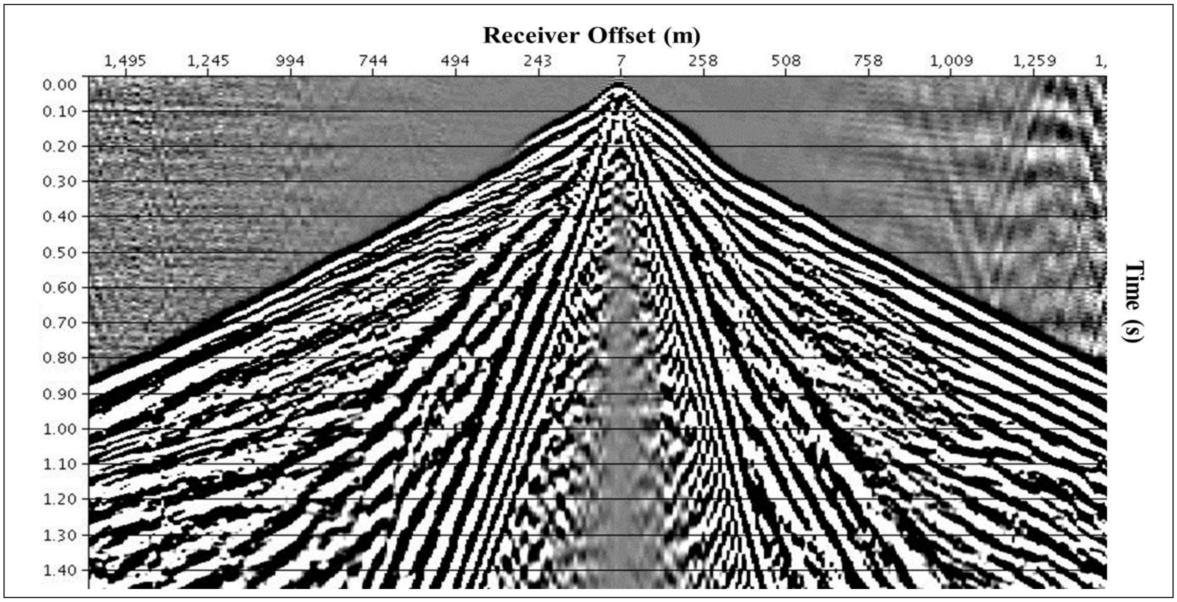

Figure 3.22: Initial seismic data signal processing: offset selection: 0-3000 meters.

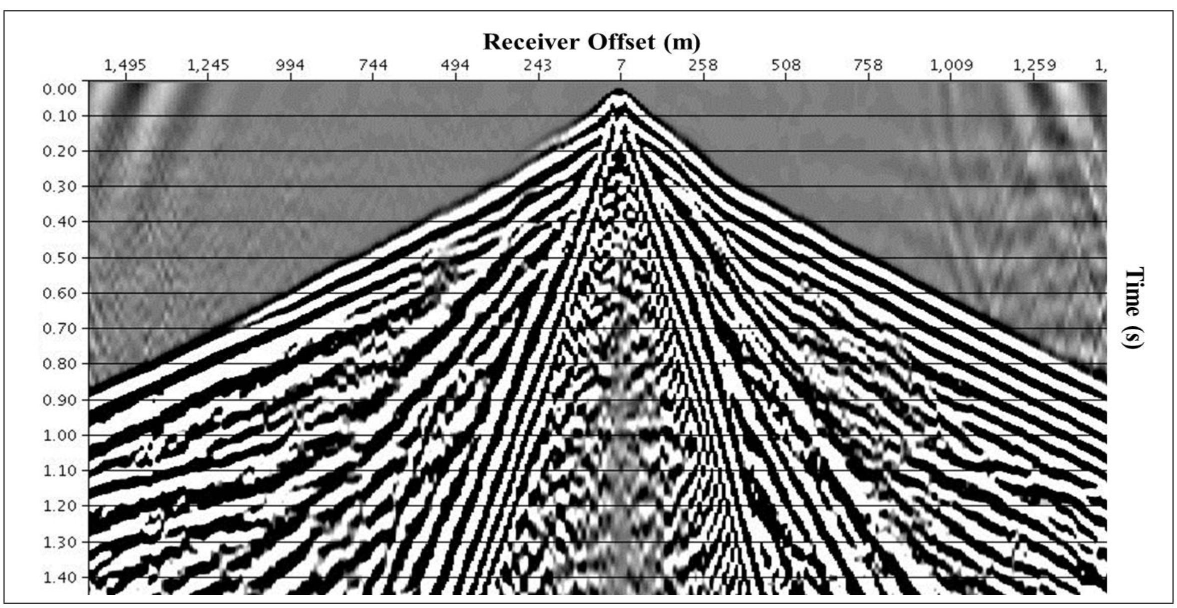

Figure 3.23: Initial seismic data signal processing: band pass filter: 1-3-20-30.

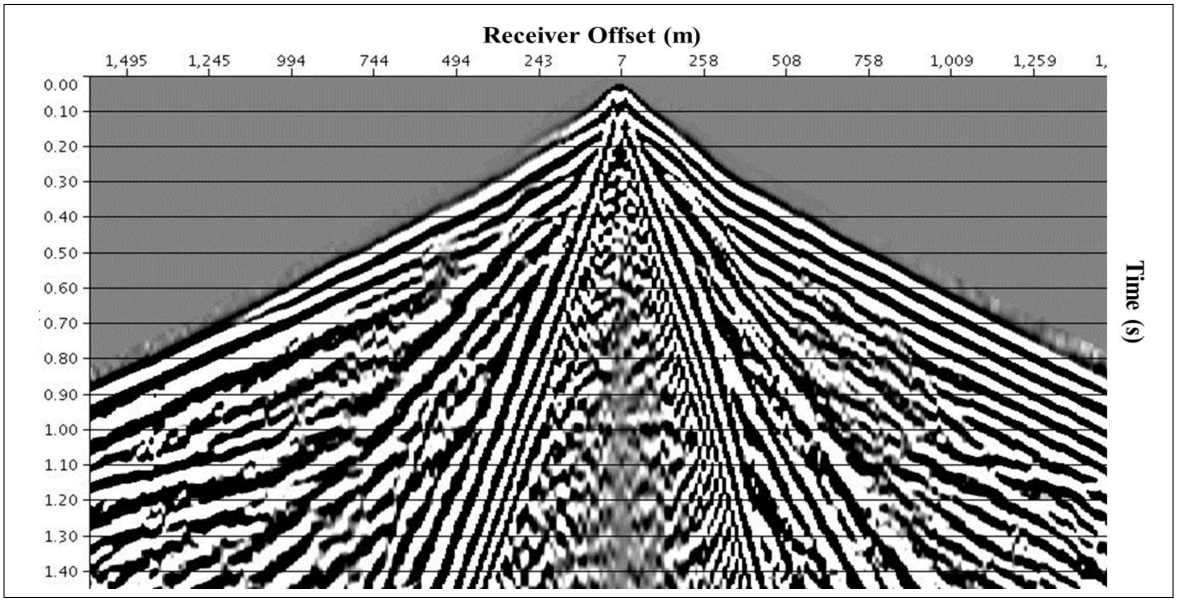

Figure 3.24: Initial seismic data signal processing: mute outside.

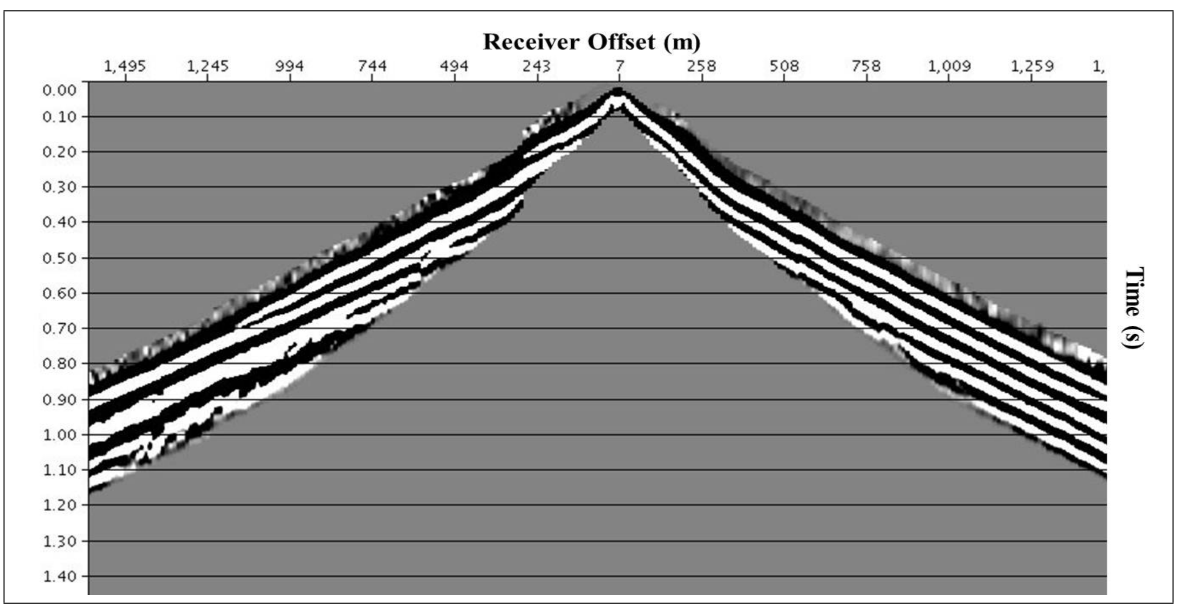

Figure 3.25: Initial seismic data signal processing: mute inside.

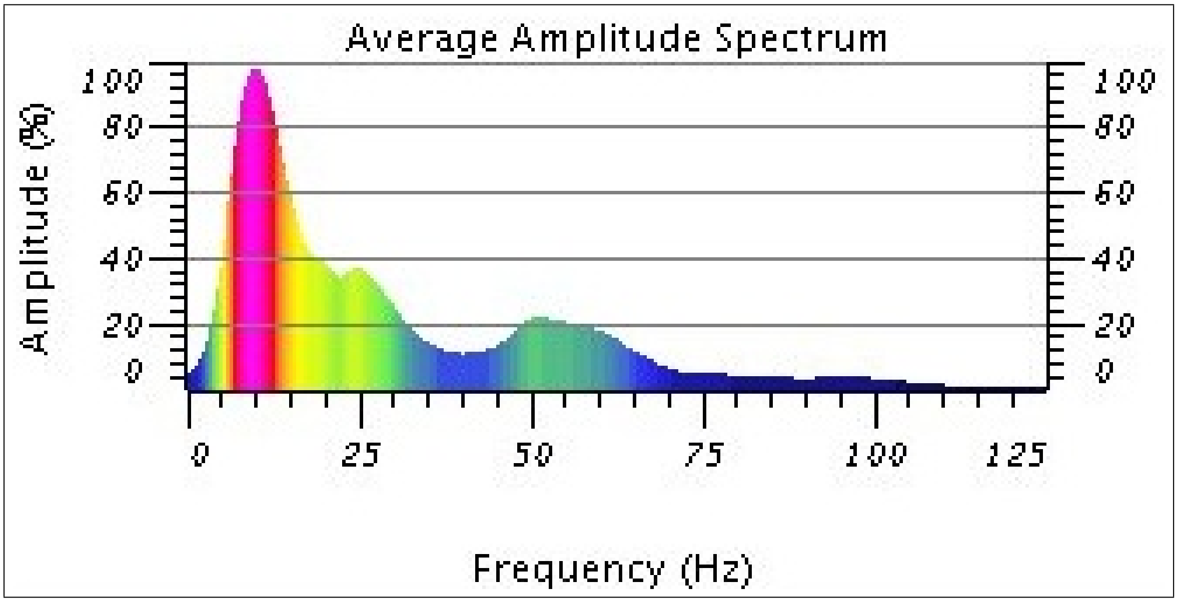

Figure 3.26: Spectrum of original data. Frequency spreads from 5-100hz. The biggest amplitude is round 5-15hz in pink.

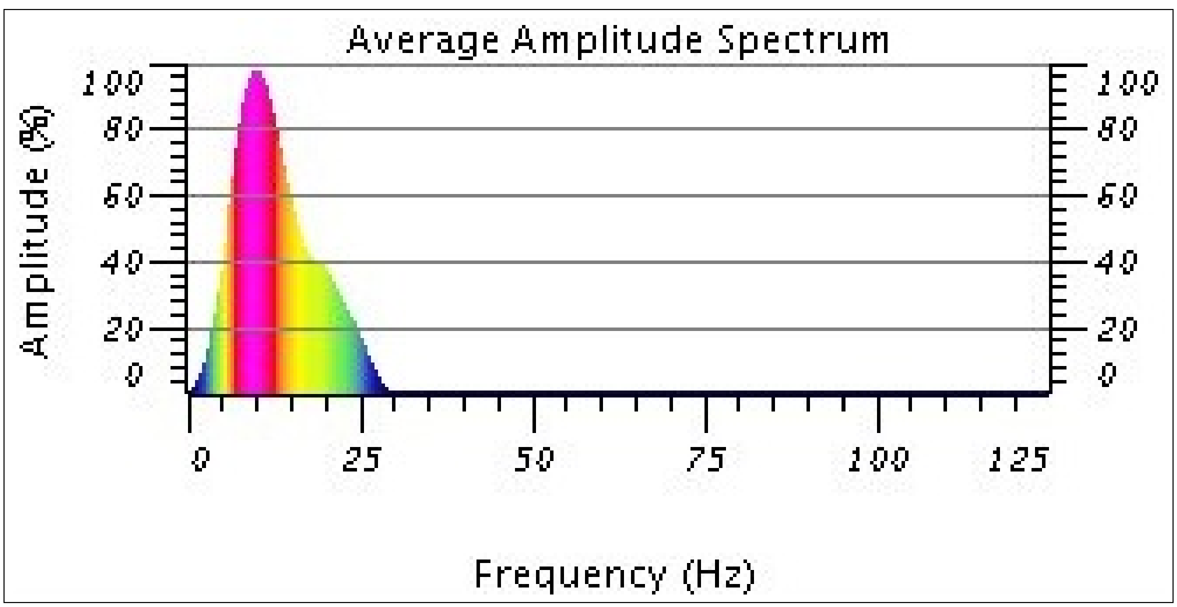

Figure 3.27: Spectrum after bandpass 1-3-20-30. Frequency spreads from 5-30hz. The biggest amplitude is round 5-15hz in pink.

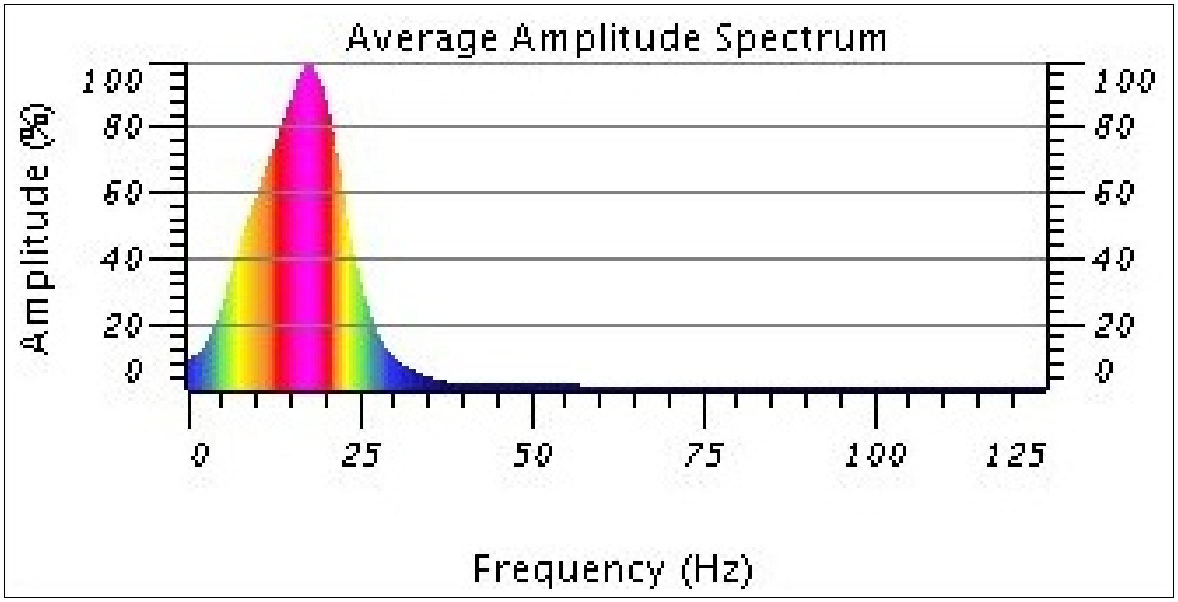

Figure 3.28: Spectrum after mute inside. Frequency spreads from 5-30hz. The biggest amplitude is round 5-20hz in pink.

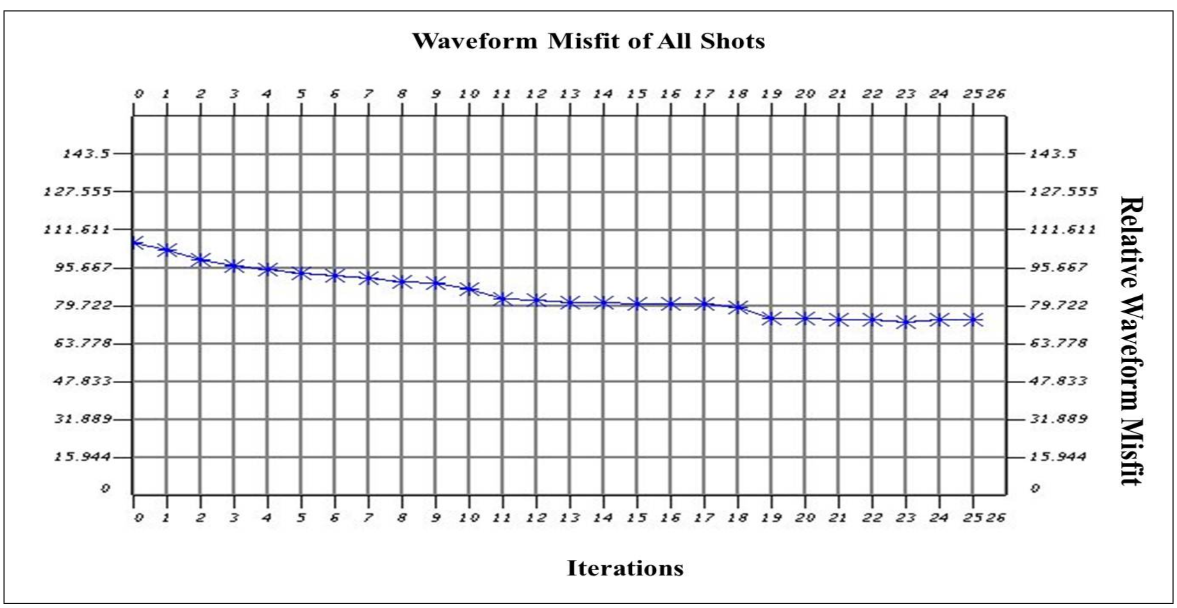

Figure 3.29: Convergence of EAT inversion

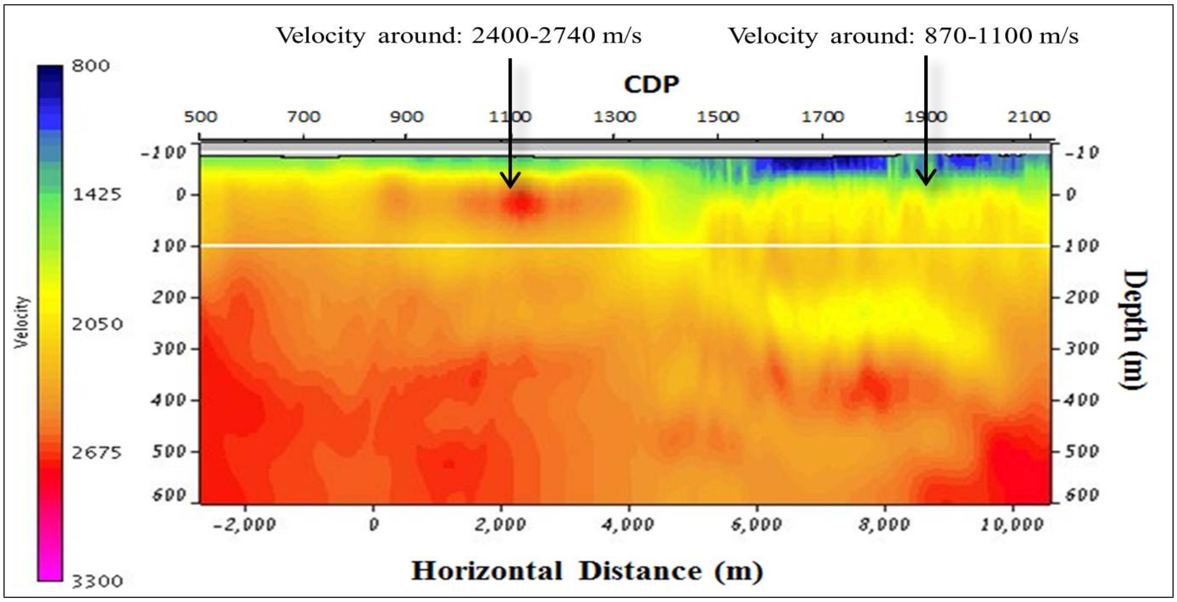

Figure 3.30: Final velocity model after 25th iterations of waveform tomography inversion. Two white lines are final datum on the top and intermediate datum at the bottom respectively. Comparing RDT and FAT (see Figure 3.12 and 3.15), RDT depicts the smoothest velocity change in both low velocity and high velociy regions. EAT describes a more laterally extended high velocity area than RDT, FAT extends the high velocity portion to the largest expanse. In the low velocity region, FAT finds a much larger and lower range of velocities than RDT, EAT produces the lowest velocity zone, covering from 870 m/s to 1100 m/s in the shallowest zone.

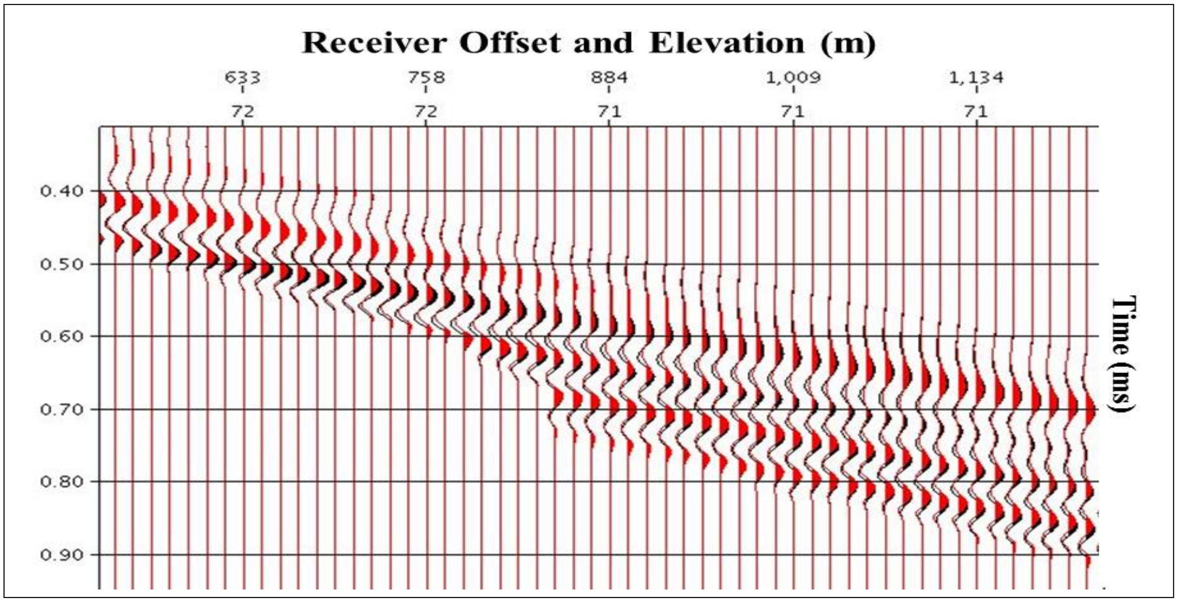

Figure 3.31: Overlay of synthetic data (red) with seismic data (black) for shot 100.

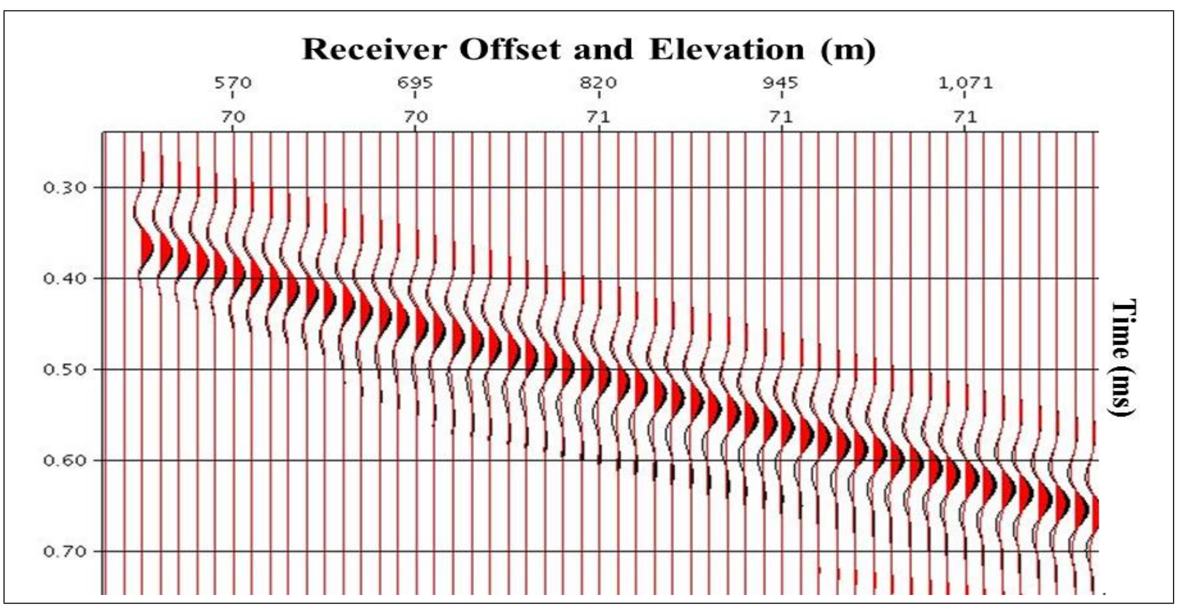

Figure 3.32: Overlay of synthetic data (red) with seismic data (black) for shot 230.

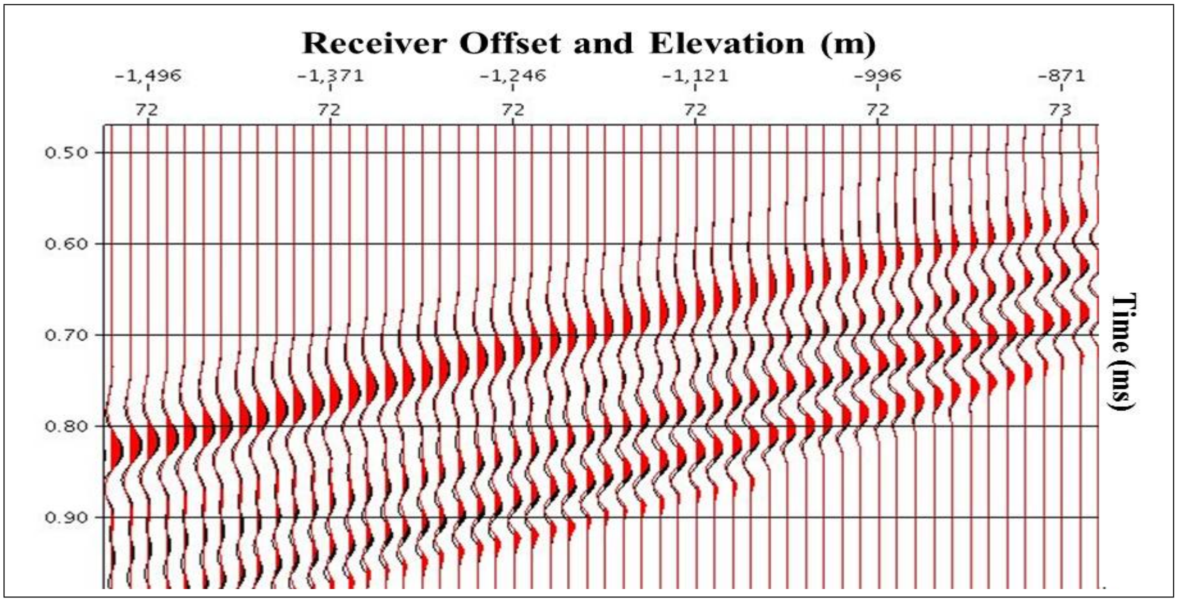

Figure 3.33: Overlay of synthetic data (red) with seismic data (black) for shot 240.

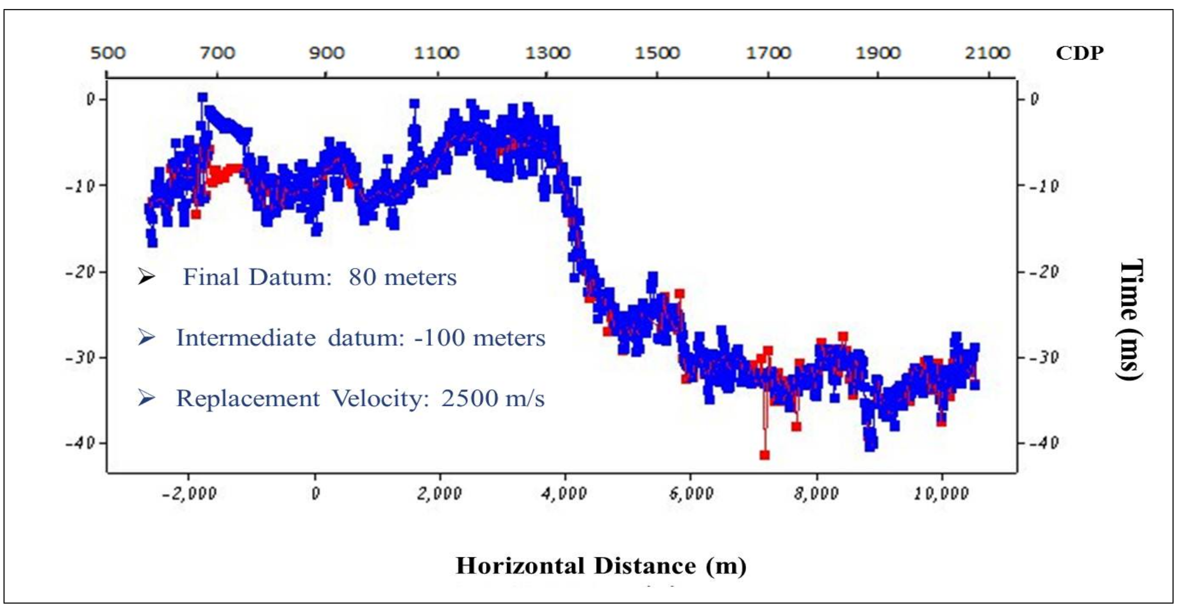

Figure 3.34: Statics of waveform tomography inversion. Red are shots and blue are receivers. The biggest difference among the three statics solutions is between CDP 1390 and 1790. This discrepancy is associated with the low-velocity abnormality. The FAT and RDT statics are quite similar, whereas the EAT results are 10ms less.

Chapter 4

SEISMIC DATA PROCESSING METHODS FOR MALAYSIA DATA

4.1 Site Geology

The Balingian test location is situated in the SK315 block of Sarawak, Malaysia (see Figure 4.1). This area is known as the Balingian Province of the Sarawak Basin (see Figure 4.2). The province is bounded on the north by the Central Luconia Province and on the west by the Southwest Balingian Line fault-complex (see Figure 4.3) with about 30 percent of this province on land. The two major synclines, known as the Acis and Balingian sub-basins, divide the province into west Balingian, characterized by NW-SE-trending fold axes, and East Balingian, characterized by NE-SW-trending fold axes. The Acis sub-basin and the Balingian sub-basin are important kitchens for oil and gas generation, which has migrated up-dip into contiguous anticlinal structures.

Reservoirs in this area are present in Late Oligocene to Middle Miocene deltaic complexes. These deltas were built by clastic sediment derived from the present-day south and west. From geochemical analysis, the hydrocarbons are derived from terrestrially derived organic matter. The oils have a high pristine/phytane ratio. Coals and marine condensed intervals within the deltaic succession are considered to be the source rocks. This area is still undergoing subsidence but most of the overburden was deposited by the mid-Pliocene. A series of sub-basin and strikeslip faults were created by differential subsidence across the area during the Miocene.

The area has a high geothermal gradient averaging 420 C/km. Reservoir rocks are in sandstone. A mixture of facies is represented: upper shoreface sandstones, fluvial and distributary sandstones of regressive parasequences, and fluvial and tidal sandstones that infill incised lowstand valleys. Traps are majorly formed by anticlines and sealed by marine condensed intervals. Gas is abundant in the area and gas clouds are frequently a problem above the anticlines.

4.2 Seismic Surveys

The survey area is located in South China Sea, Balingian, Malaysia, onshore SK315 block of Sarawak. Water depths are expected to be in the range of 30m - 50m with benign seafloor conditions and currents. This 2D OBC survey includes two shot lines and two receiver lines as seen in Figure 4.4. Shot line A (SLA) and shot line B (SLB) are 28 kilometers and 35 kilometers respectively. Receiver line A (RLA) and

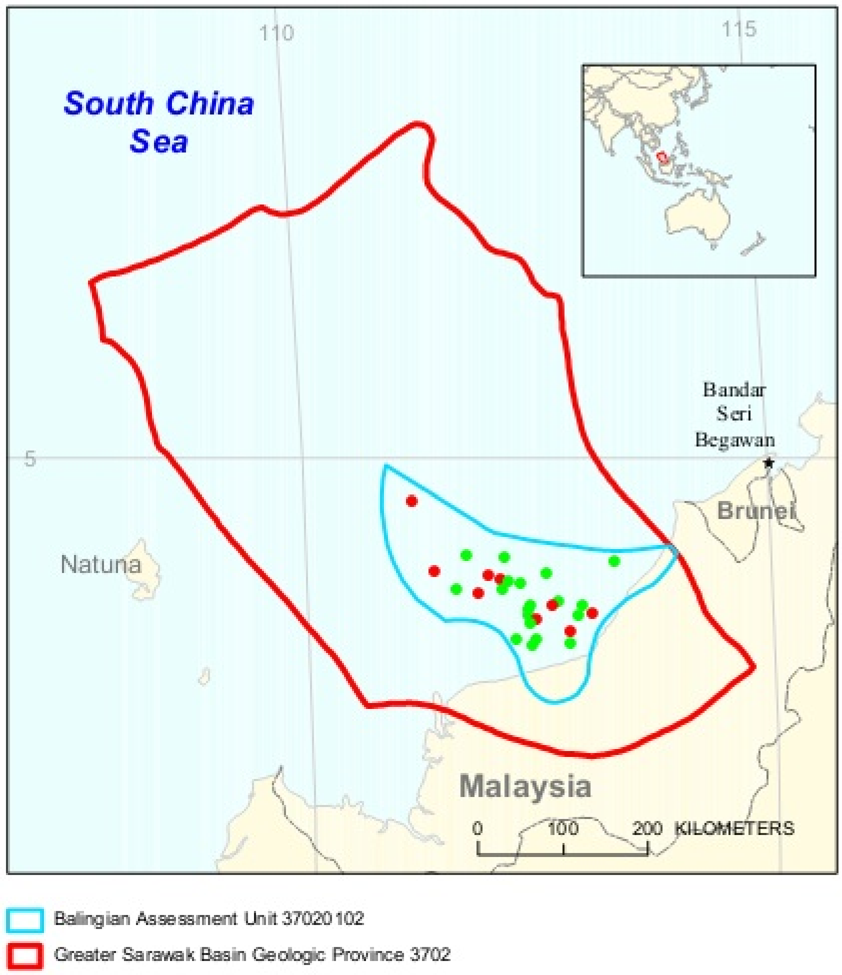

Figure 4.1: Location of processed 2D OBC data.

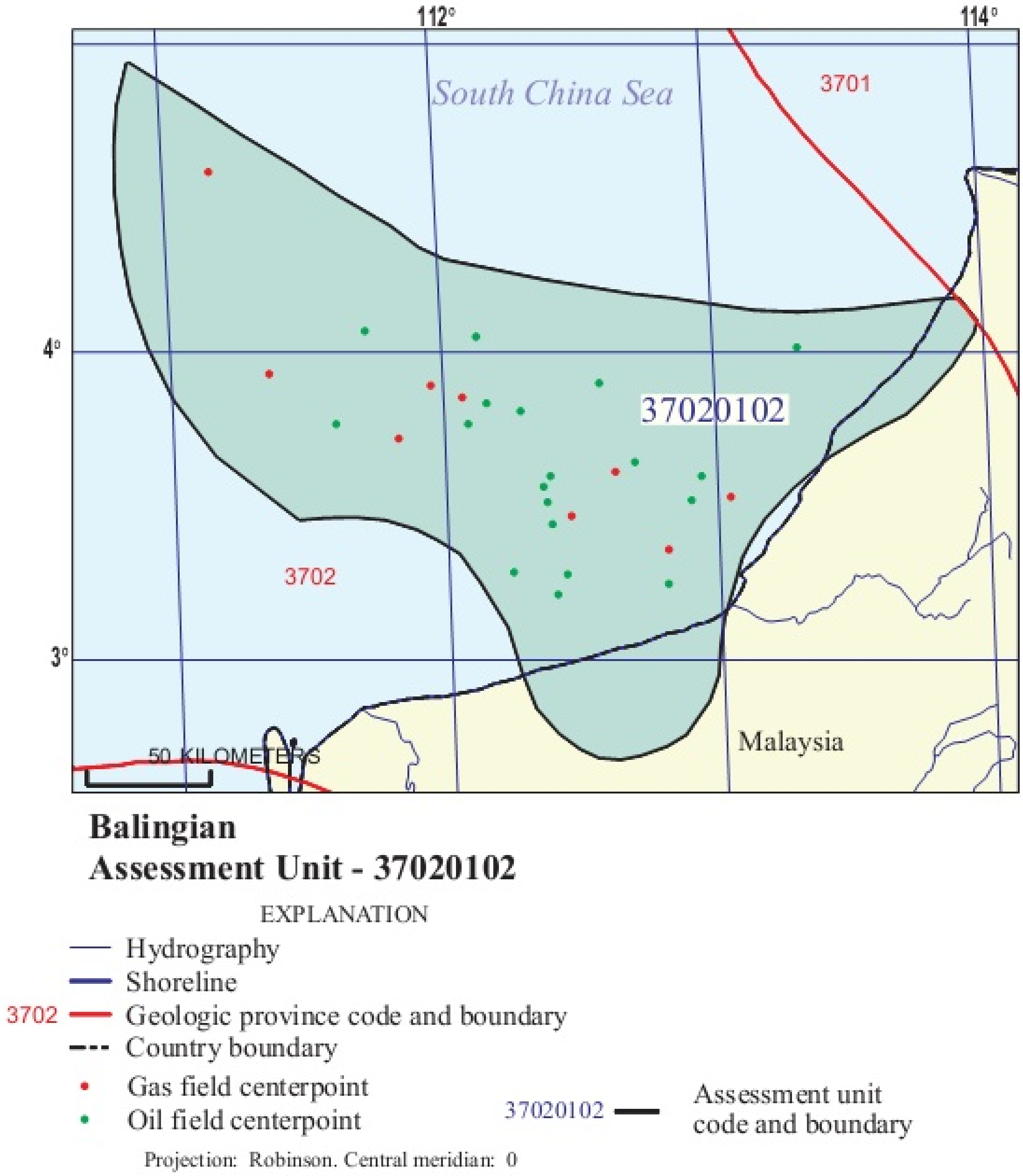

Figure 4.2: Balingian Province of the Sarawak Basin.

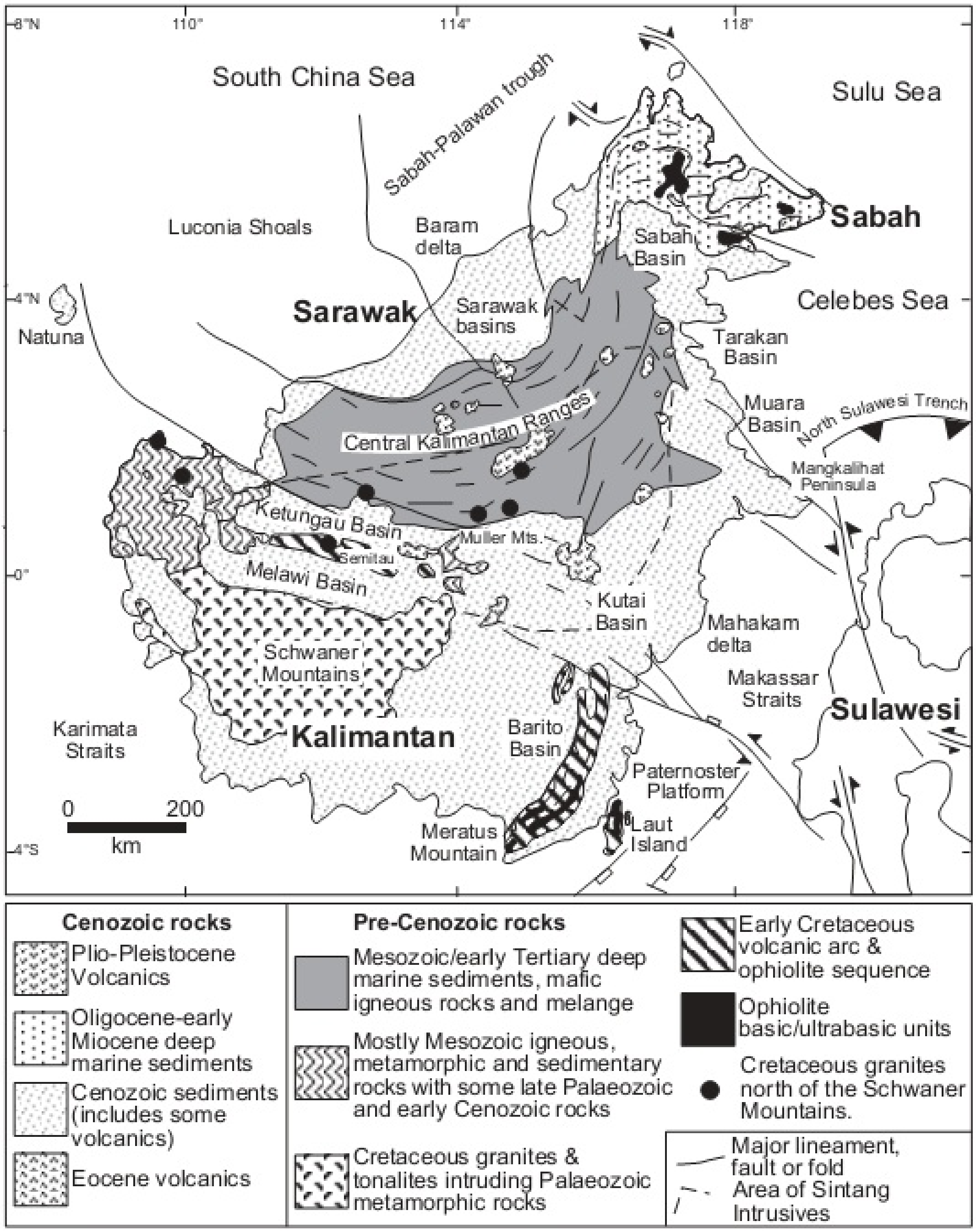

Figure 4.3: Site geology of Balingian Province of the Sarawak Basin.

receiver line B (RLB) are both 5 kilometers, spreading above the gas cloud which is an estimated 18 kilometers long. Respectively the source lines are shot from outside, through and beyond the gas cloud. There are approximately 2520 shots and 400 receivers into the two spreads. The amount of data here contains 2069 shots and 400 receivers which lay above the gas cloud region. There is a 25m shot interval and 25m receiver interval with a record length of 4 seconds and sample rate of 2ms. The geometry and certain statics of the survey are displayed in Figure 4.5. In order to improve the picking efficiency and inversion, a common receiver sort is used. So the shot information shown in Figure 4.5 should be the actual receiver information, while the receiver number is the real shot number.

The Sercel SeaRay system was fielded for the test. A 5km continuous cable section was recorded and moved as required. The sensors include a hydrophone and a 3C MEMS accelerometer packaged together in a single housing.

The parameters for source and receiver are as below:

o Airgun: Large Towed Array with 12 Sercel G guns with a total volume of 1550 in and a depth of 5m.

o Sensor type: SeaRay 4C.

o Cable Length: 5 km x 2 = 10 km

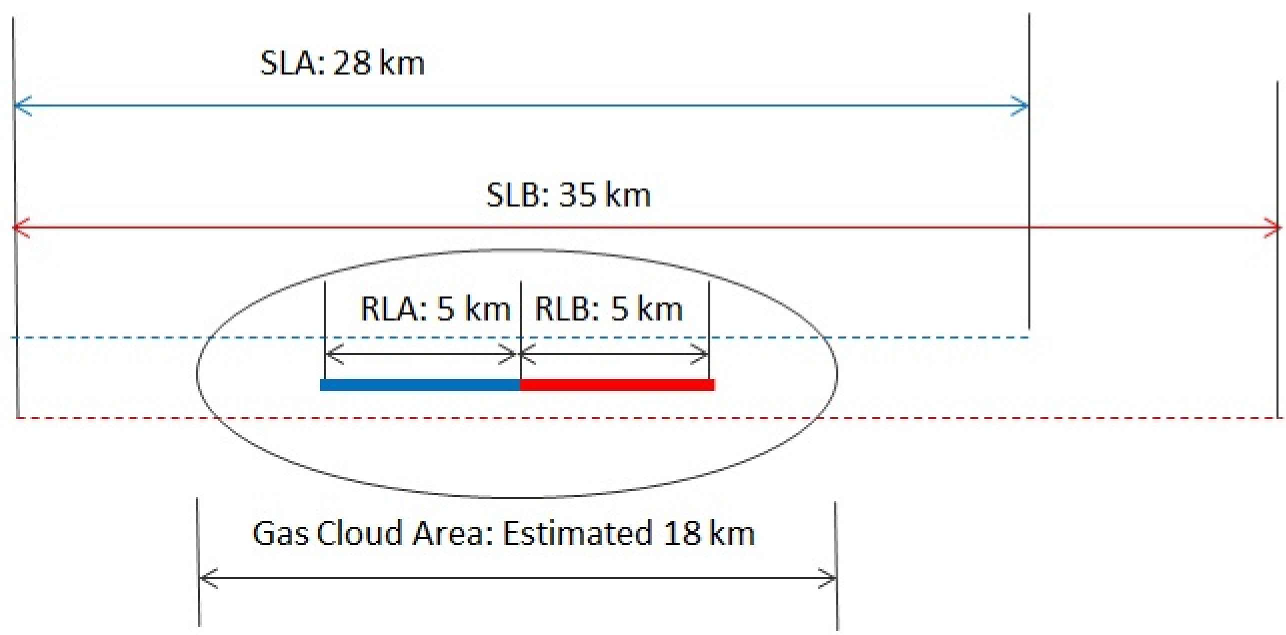

Figure 4.4: Seismic survey layout. Shot Line A (SLA): Blue Line, 28 kilometers. Shot Line B (SLB): Red Line, 35 kilometers. Receiver Line A (RLA): Bold Blue Line, 5 kilometers, spreading above the gas cloud. Receiver Line B (RLB) : Bold Red Line, 5 kilometers, spreading above the gas cloud.

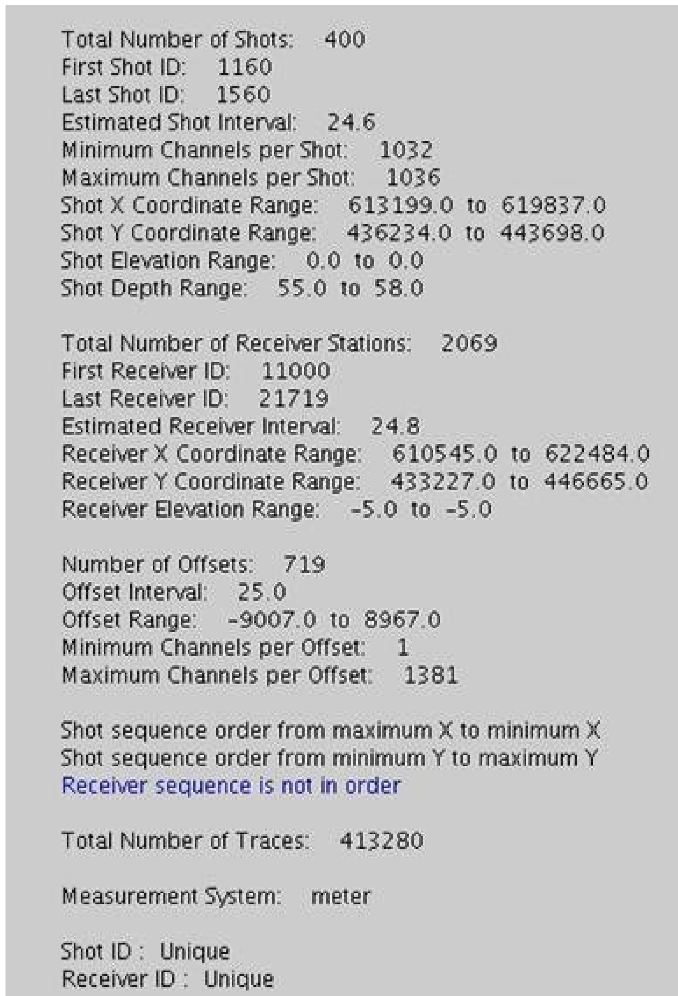

Total Number of Shots: 400
First Shot ID: 1160
Last Shot ID: 1560
Estimated Shot Interval: 24.6
Minimum Channels per Shot: 1032
Maximum Channels per Shot: 1036
Shot X Coordinate Range: 613199.0 to 619837.0
Shot Y Coordinate Range: 436234.0 to 443698.0
Shot Elevation Range: 0.0 to 0.0
Shot Depth Range: 55.0 to 58.0

Total Number of Receiver Stations: 2069
First Receiver ID: 11000
Last Receiver ID: 21719
Estimated Receiver Interval: 24.8
Receiver X Coordinate Range: 610545.0 to 622484.0
Receiver Y Coordinate Range: 433227.0 to 446665.0
Receiver Elevation Range: -5.0 to -5.0

Number of Offsets: 719
Offset Interval: 25.0
Offset Range: -9007.0 to 8967.0
Minimum Channels per Offset: 1
Maximum Channels per Offset: 1381

Shot sequence order from maximum X to minimum X
Shot sequence order from minimum Y to maximum Y
Receiver sequence is not in order

Total Number of Traces: 413280

Measurement System: meter

Shot ID : Unique
Receiver ID : Unique

Figure 4.5: Geometry information.

4.3 Seismic Data Processing Method

4.3.1 Refraction Delay-Time Solution (RDT)

As what was mentioned in Chapter 3, first arrivals need to be picked, geometry QC, and the delay-time refractor branches determined before the RDT velocity model can be calculated and statics derived.

4.3.1.1 Picking and Quality Control

First-break Picking

It is not difficult to pick first breaks automatically using the hydrophone portion of the data. The first breaks can be easily identified as shown in Figure 4.6 and 4.7. After applying fully automatic picking, the tracker to half-manually refine the bad first breaks in common shot gathers was used.

QC Geometry and Refine Bad Picks

As in the workflow for the Peru example, the function of Reciprocal Error to QC the picks and geometry for the first time was used. In Figure 4.8, all the Reciprocal Error is lower than 10 ms and the geometry seems correct.

4.3.1.2 QC First Breaks Again and Pick RDT Branch

As seen in Figure 4.9, all Reciprocal Errors are below 8 ms and most of them spread from 3 ms to 6 ms.

Picking RDT Branches

In plotting the traveltime versus offset with LMO 2500m/s applied and three refractors were defined, as seen in Figure 4.10.

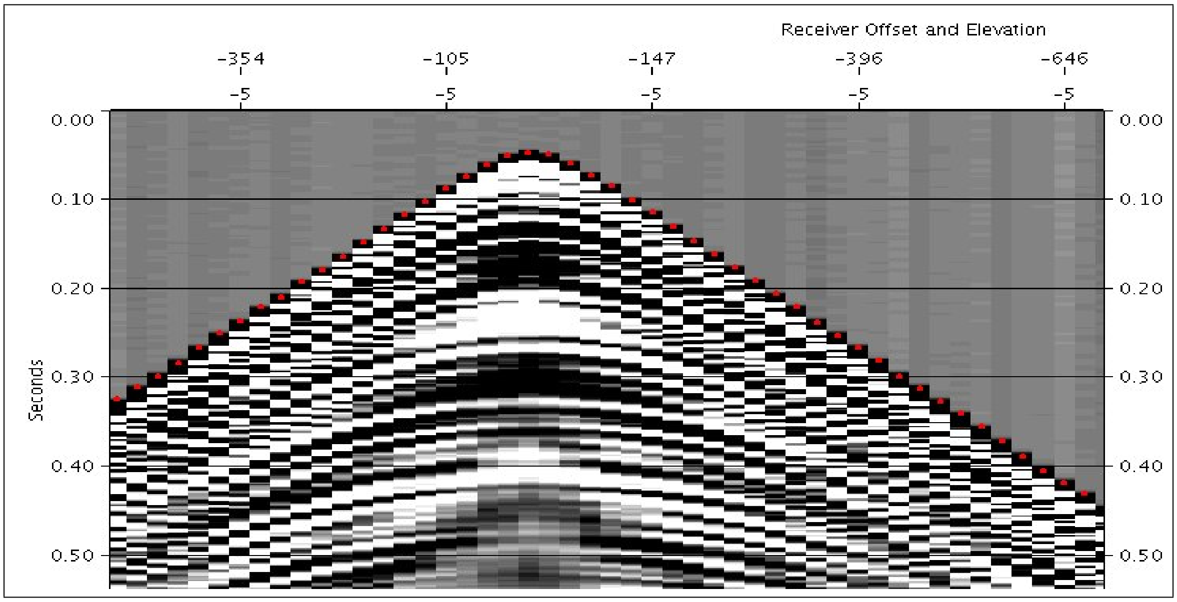

Figure 4.6: Shot gather 31 with picks from one receiver cable. Red dota are user picking.

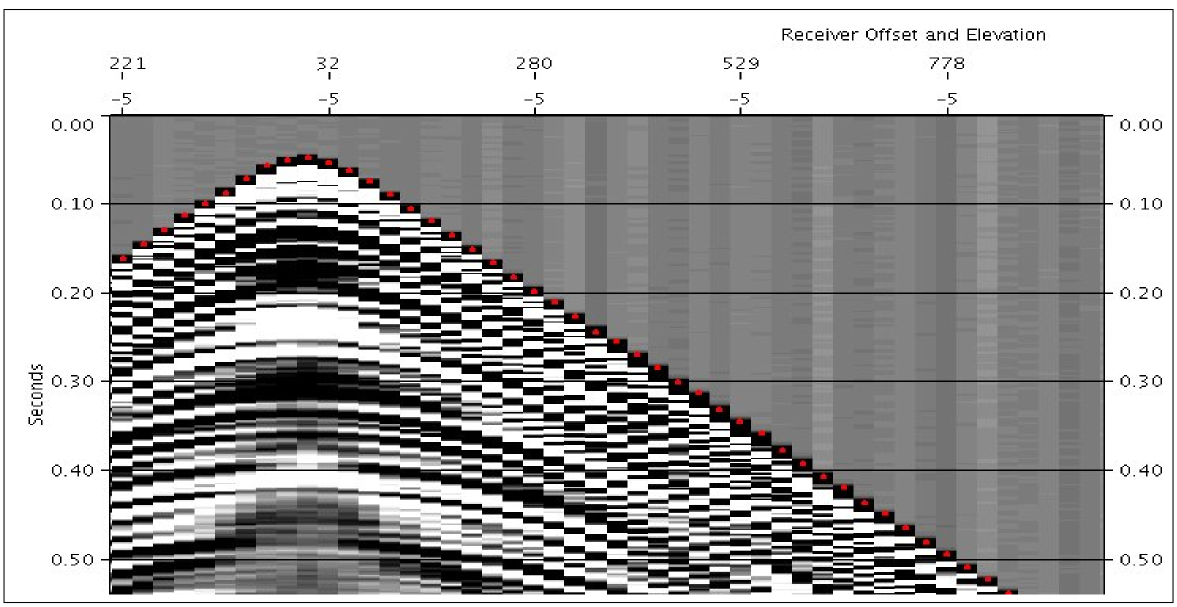

Figure 4.7: Shot gather 31 with picks from the other receiver cable. Red dota are user picking.

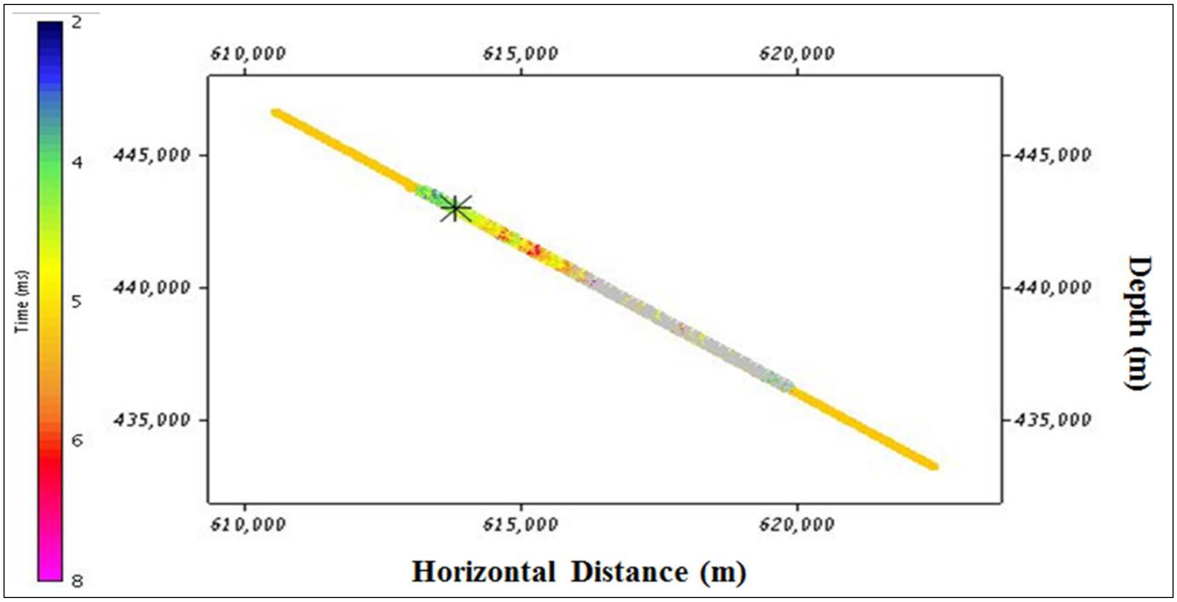

Figure 4.8: QC geometry and first breaks. The maximum Reciprocal Error for picking is 10 ms, and different color stands for different Reciprocal Error and distributions in the geometry line.

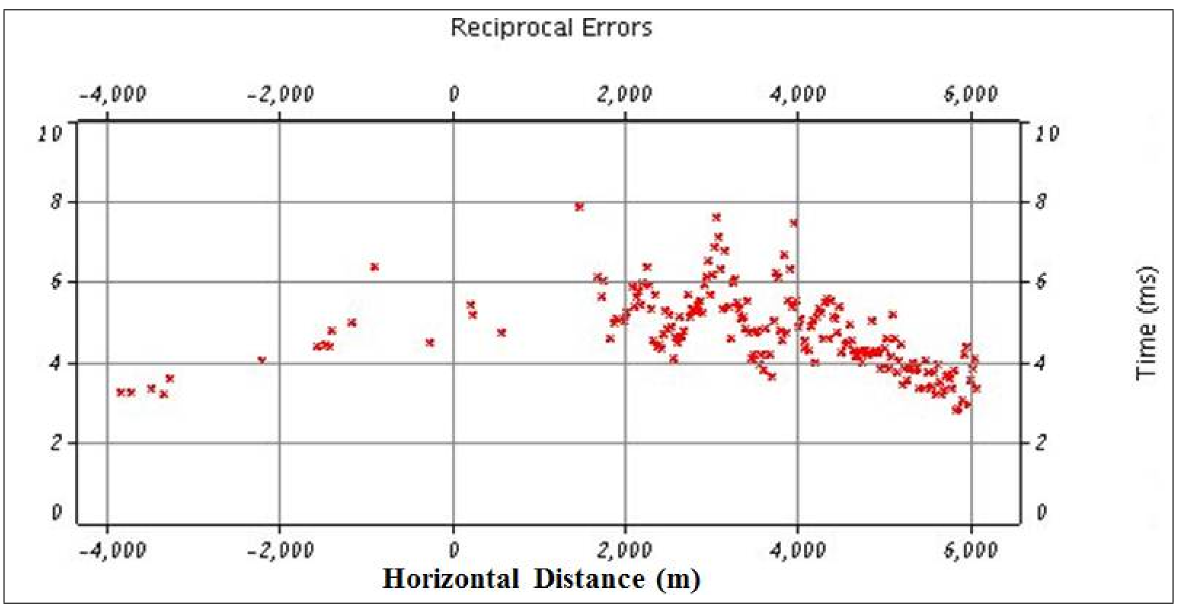

Figure 4.9: QC Geometry and first breaks again. It plots Reciprocal Error spread with all the shots. All Reciprocal Errors are below 8 ms and most of them spread from 3 ms to 6 ms.

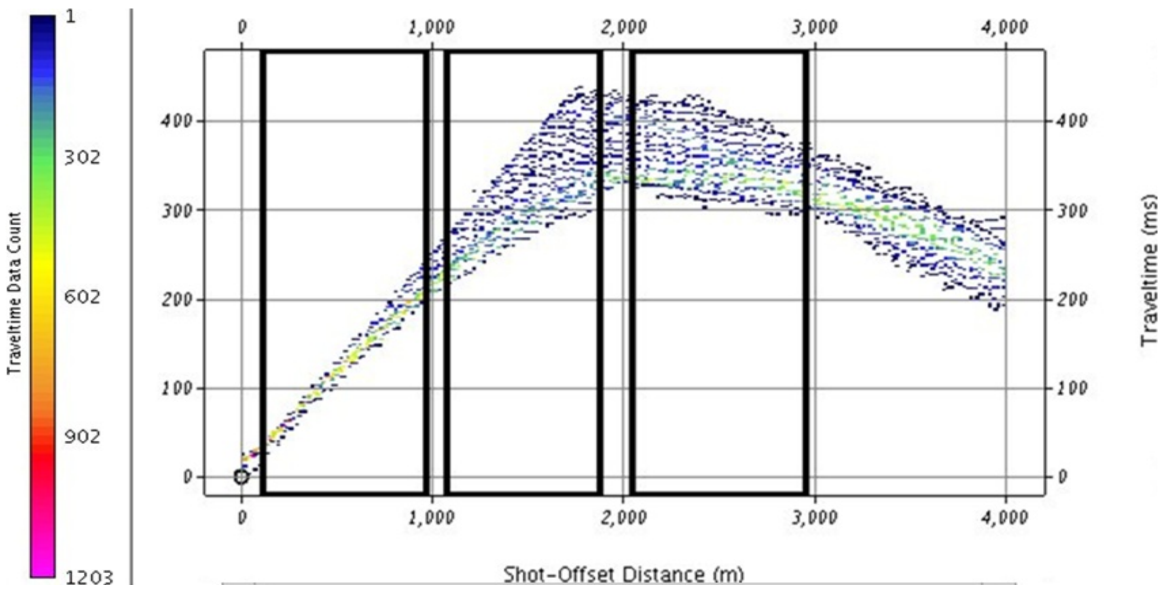

Figure 4.10: Pick 3 branches of first breaks according to the refractors. Plotting the traveltime versus offset with LMO 2500m/s applied.

4.3.1.3 Build RDT Velocity Model, Define Intermediate and Final Datum

After picking the branches of first breaks, RDT solutions were calculated to derive a velocity model and define intermediate and final datum as shown in Figure 4.11. 0 meters (sea level) and -400 meters were the intermediate datum and final datum respectively. A replacement velocity starting at 1500m/s and then with the velocity gradient away from the anomaly was used as the background to calculate the statics (see Figure 4.12). Both shot and receiver statics were referenced to sea level. Blue is the shot statics and red are the receiver ones.

In Figure 4.11 the X axis is the horizontal distance and the vertical axis notes the depth in meters. The color bar presents the velocity spread from 1350m/s which is in blue increasing to 3000m/s in pink. The top white line stands for final datum of is 0m (the sea level), the common choice for marine data. The middle white line indicates the ocean bottom and the intermediate datum beneath it is 400 meters below the sea level.

According to the depth of the near-surface velocity anomalies (the gas cloud regions), 400 meters below the sea level was picked as intermediate datum. Consequently, a gradient velocity consistent with the shallow velocity away from the gas anomaly, instead of constant velocity, had been chosen to be replacement velocity in statics calculation in order to avoid introducing velocity problems.

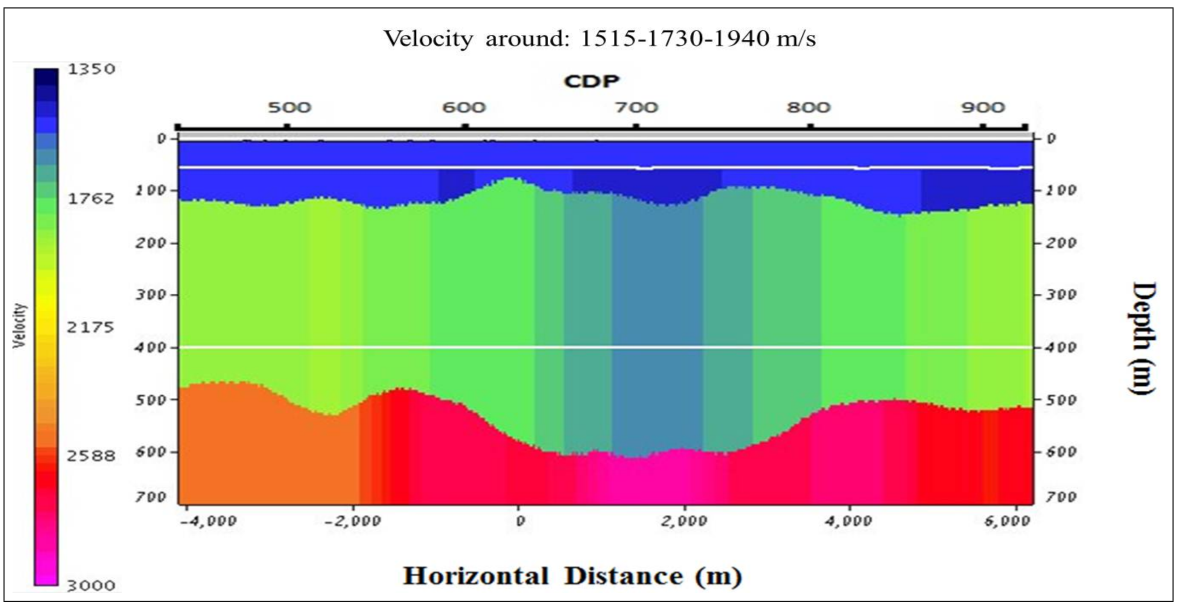

Figure 4.11: Three-Layer RDT velocity model. Three white lines are final datum on the top, ocean bottom in the middle, and intermediate datum at the bottom respectively.

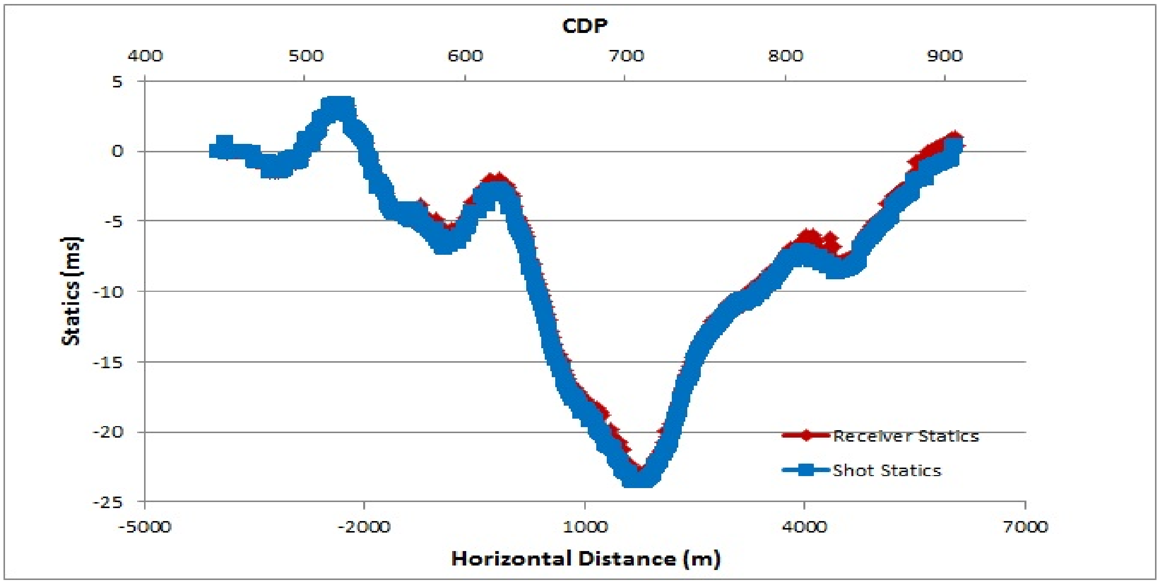

Figure 4.12: Delay-Time statics plot. Red are shots and blue are receivers.

4.3.2 First-Arrival Traveltime Tomography Solution (FAT)

4.3.2.1 FAT Velocity Model

Utilizing delay-time velocities as an initial model, 20 iterations of tomographic inversion were run to update velocity model. Figure 4.13 shows the rate of convergence. Final first-arrival traveltime velocity model and ray density model are shown in Figures 4.14 and 4.15. Figure 4.16 to 4.18 display the overlay predicted picks with the real picks.

4.3.2.2 FAT Statics

Using a final flat datum of 0 meters, an intermediate datum of -400 meters and a gradient replacement velocity as described in the RDT section, the statics of Figure 4.19 were calculated.

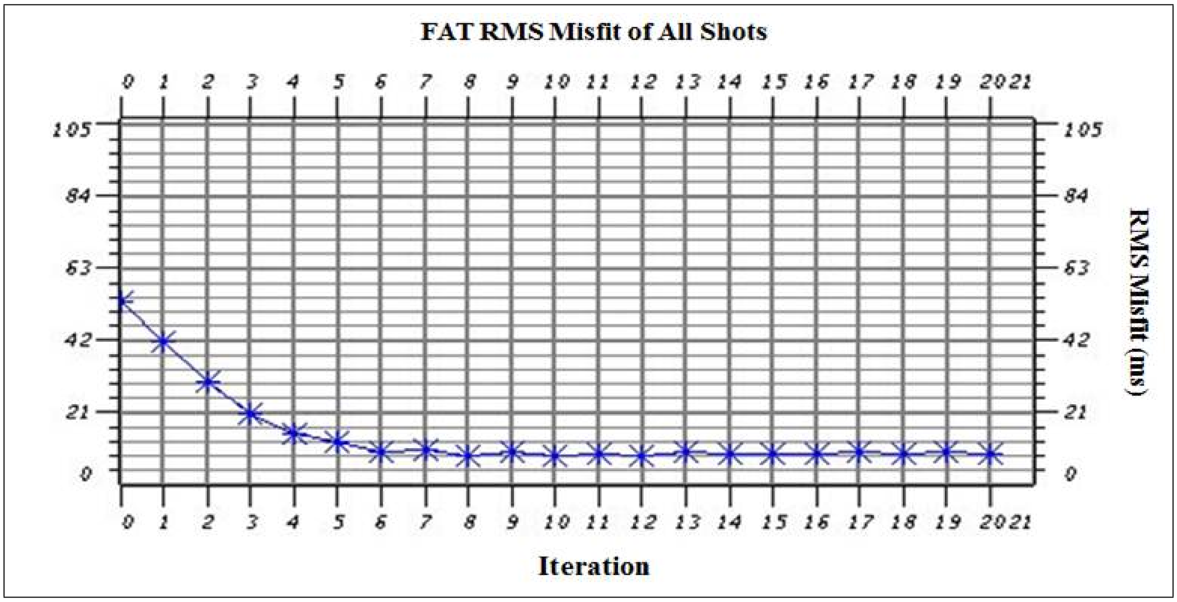

Figure 4.13: Tomographic inversion.

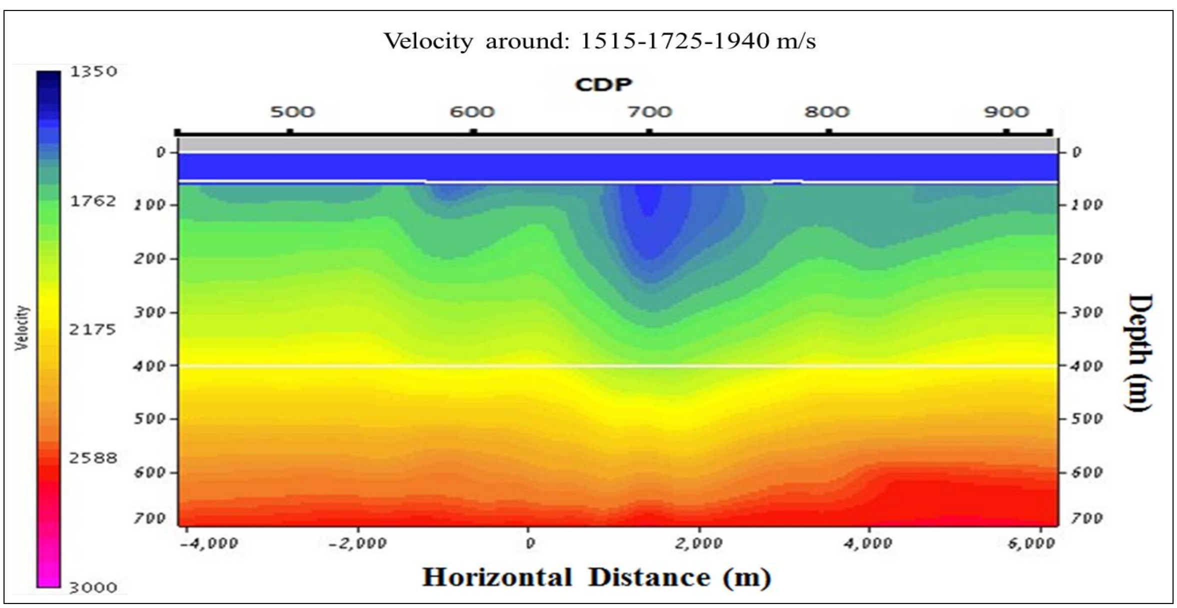

Figure 4.14: Final FAT velocity model inversed from delay-time model. Model grid size is 5m*5m. Three white lines are final datum on the top, ocean bottom in the middle, and intermediate datum at the bottom respectively.

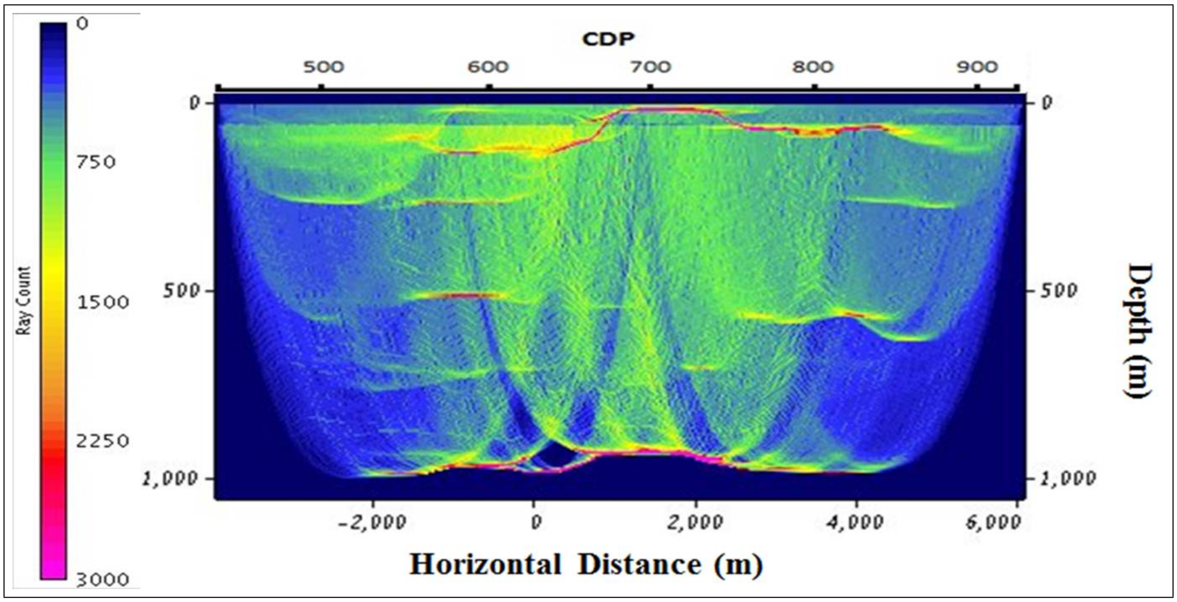

Figure 4.15: Ray density of final traveltime velocity model.

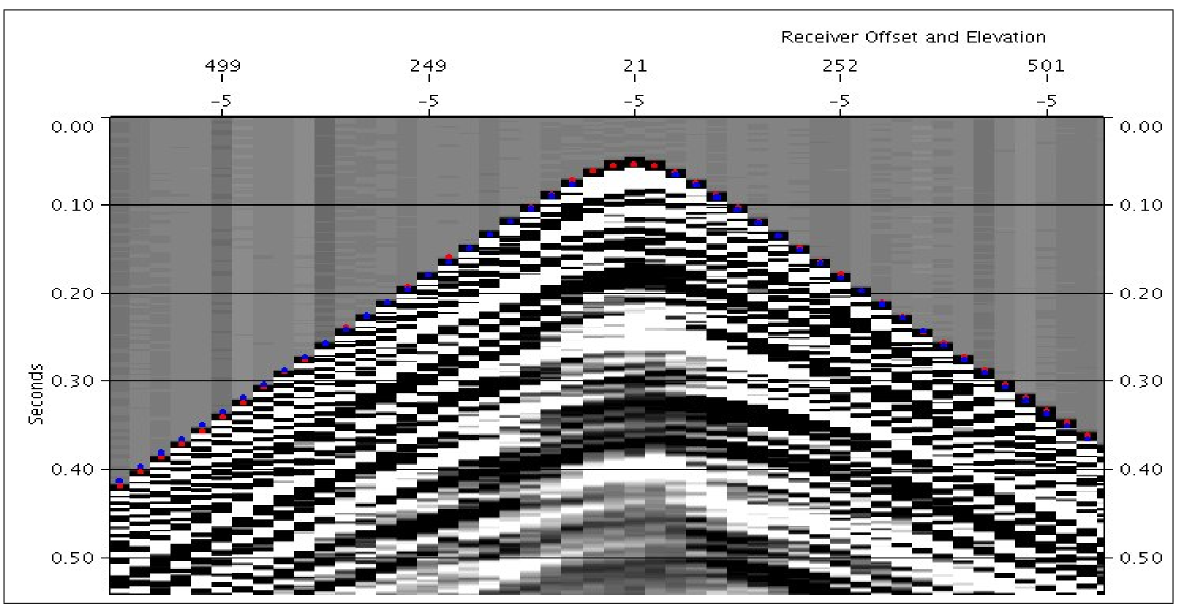

Figure 4.16: FAT overlay for shot 111: fitting the synthetic first arrivals in user picks. Blue are synthetic first breaks, red are observed first arrivals.

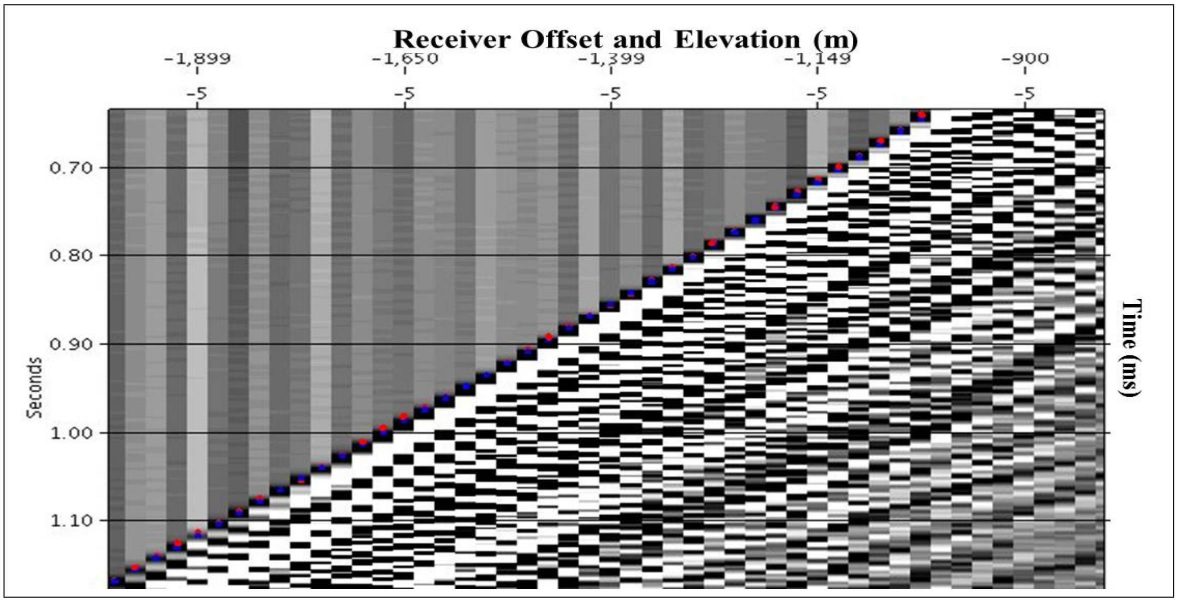

Figure 4.17: FAT overlay for shot 201: fitting the synthetic first arrivals in user picks. Blue are synthetic first breaks, red are observed first arrivals.

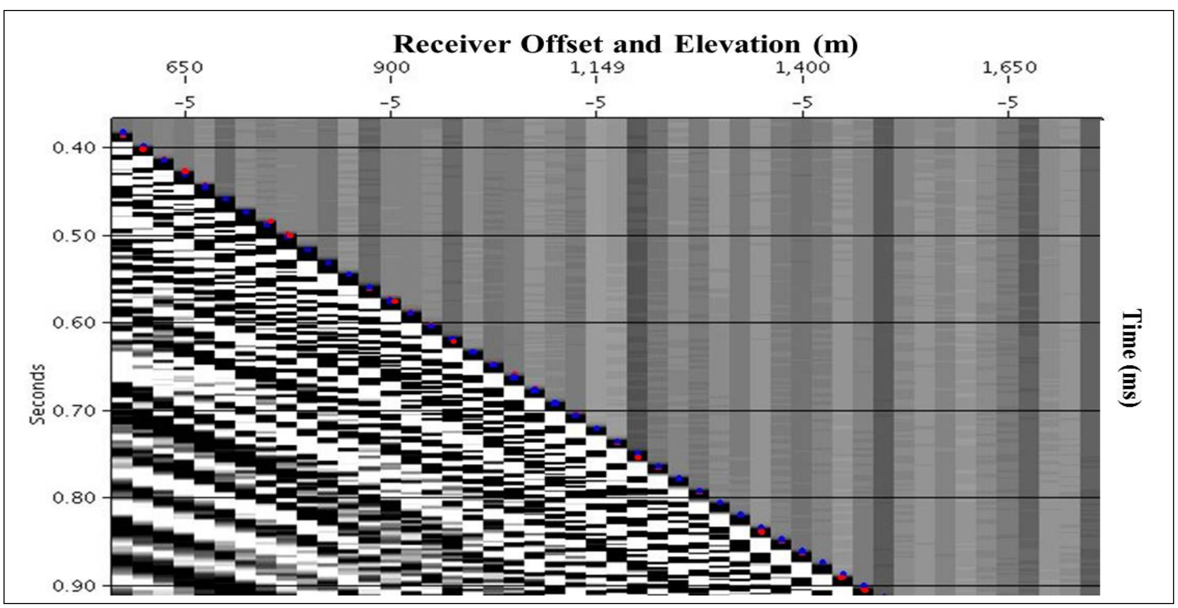

Figure 4.18: FAT overlay for shot 361: fitting the synthetic first arrivals in user picks. Blue are synthetic first breaks, red are observed first arrivals.

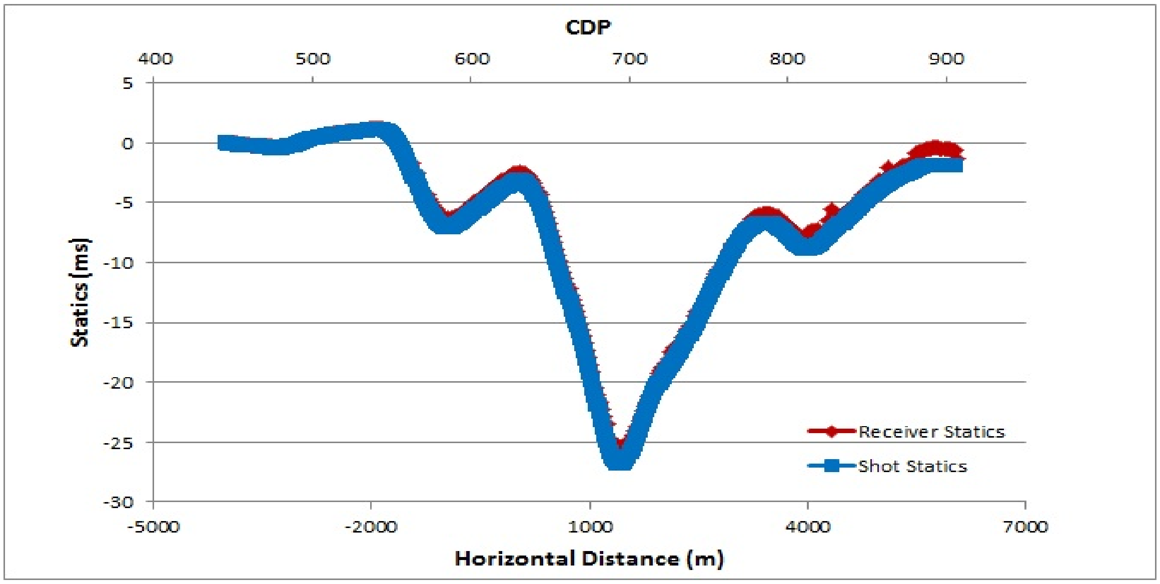

Figure 4.19: First-Arrival Traveltime Tomography statics. Red are receivers and blue are shots.

4.3.3 Early-Arrival Waveform Tomography (EAT) Solution

4.3.3.1 EAT Initial Seismic Data Signal Processing

The pre-processing of the 2D OBC seismic data was performed to prepare the data for waveform tomography including offset selection, band pass, muting the early noise and later mud roll, with selecting the windows. Figures 4.20 to 4.24 illustrate these procedures.

Again, take a common shot gather as an example, Figures 4.18 shows how this original shot looks after balancing the amplitude. Band-pass filter (Figures 4.21), selecting certain offset (Figures 4.22), mute outside noise and inside noise (Figures 4.23 and Figures 4.24) can reduce the pre-cursor noise and low frequency noise such as mud roll as well as improve the computation efficiency and to keep the appropriate low frequency seismic data to avoid cycle-skipping in the waveform inversion.

4.3.3.2 EAT Velocity Model

Using the first-arrival traveltime tomography velocity as an initial model and performing waveform tomography inversion with the convergence show in Figure 4.25. The final waveform velocity model shown in Figure 4.26 is achieved.

Figures 4.27 to 4.29 display the early-arrival waveform overlay of the predicted model data to the real windowed data.

4.3.3.3 EAT Statics

The same intermediate datum, final datum and gradient replacement velocity are used to calculate the EAT statics as seen in Figure 4.30.

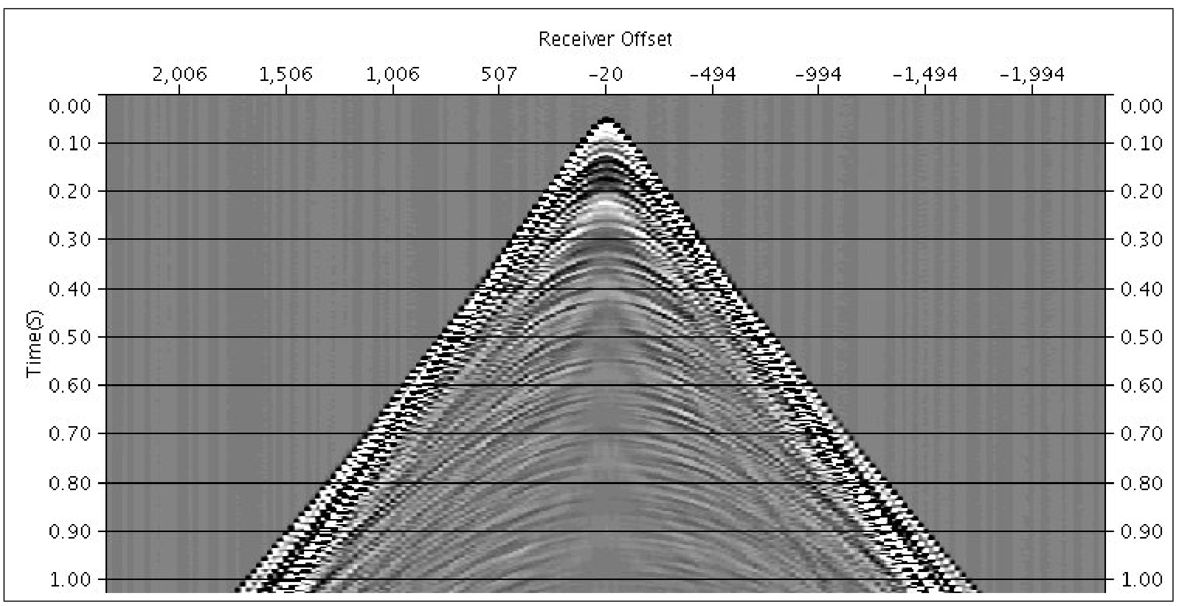

Figure 4.20: Initial seismic data signal processing: balancing original data.

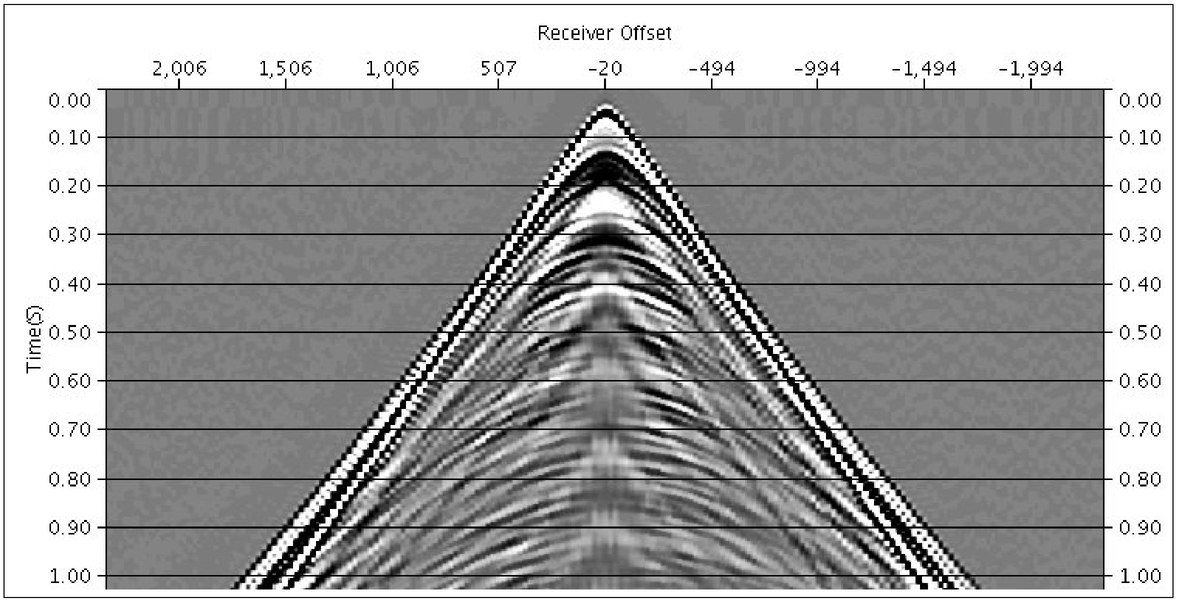

Figure 4.21: Initial seismic data signal processing: band-pass filter: 1-5-25-65.

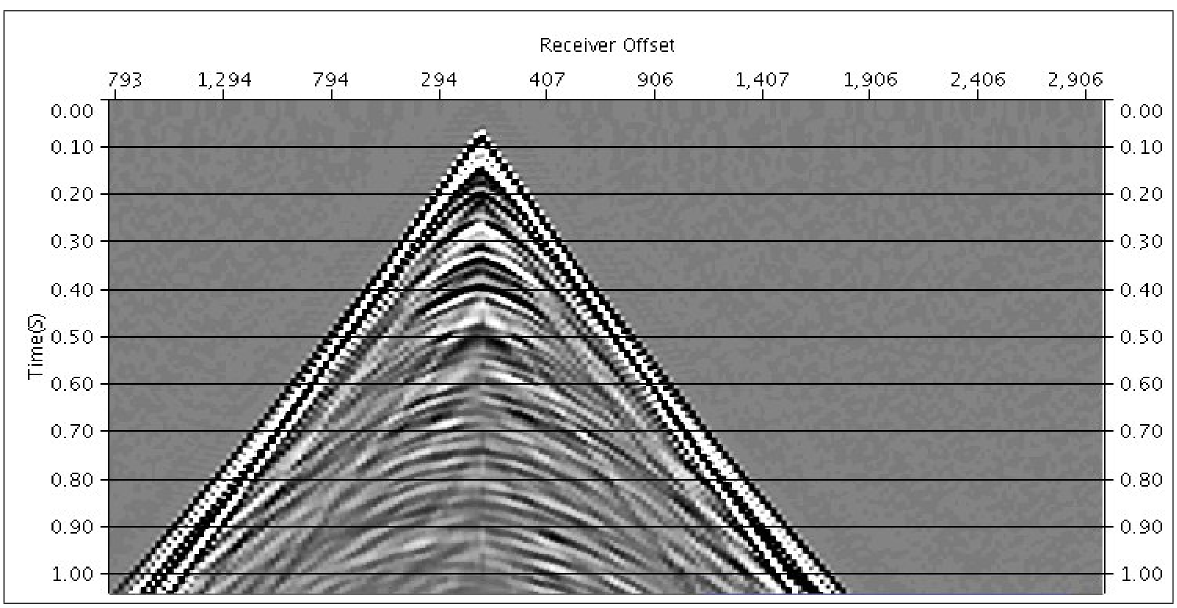

Figure 4.22: Initial seismic data signal processing: offset selection: 100-3000 meters.

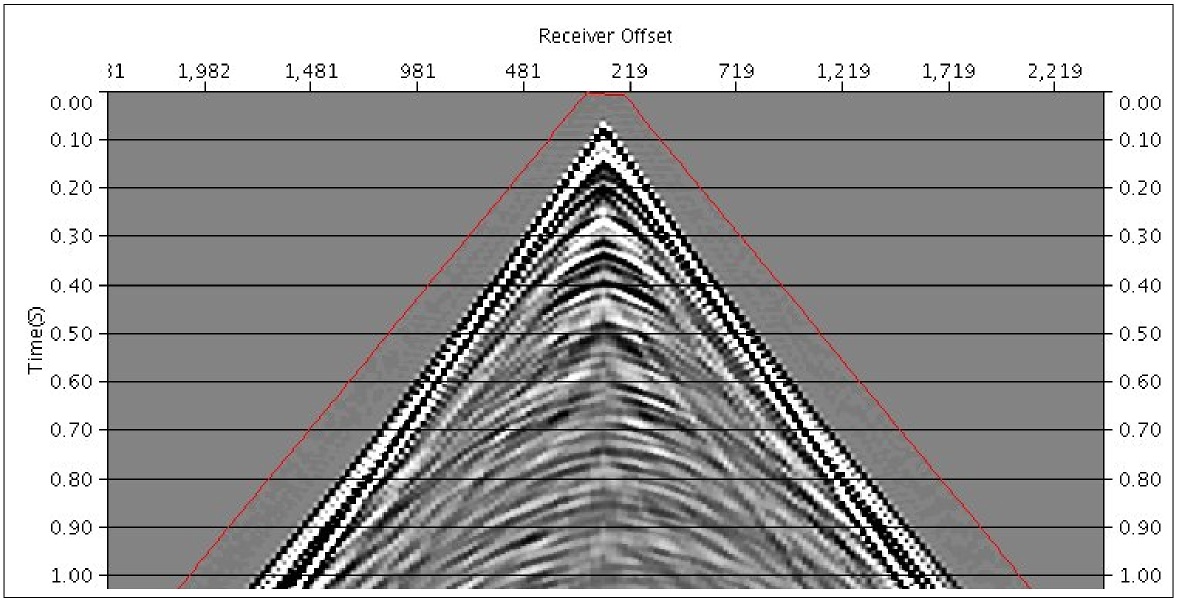

Figure 4.23: Initial seismic data signal processing: mute outside.

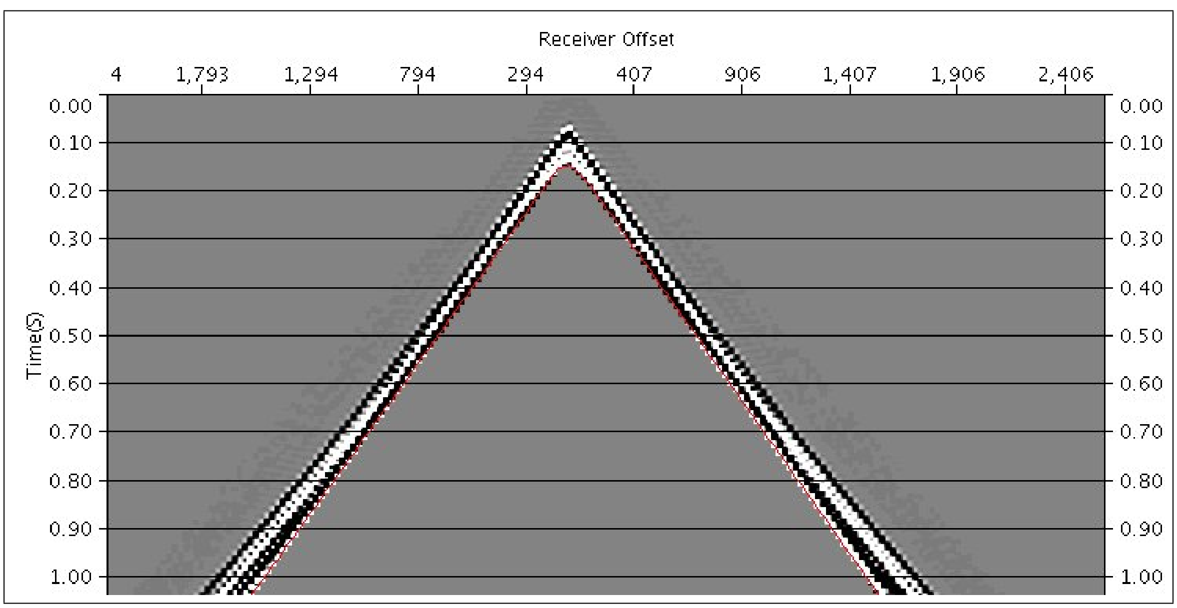

Figure 4.24: Initial seismic data signal processing: mute inside.

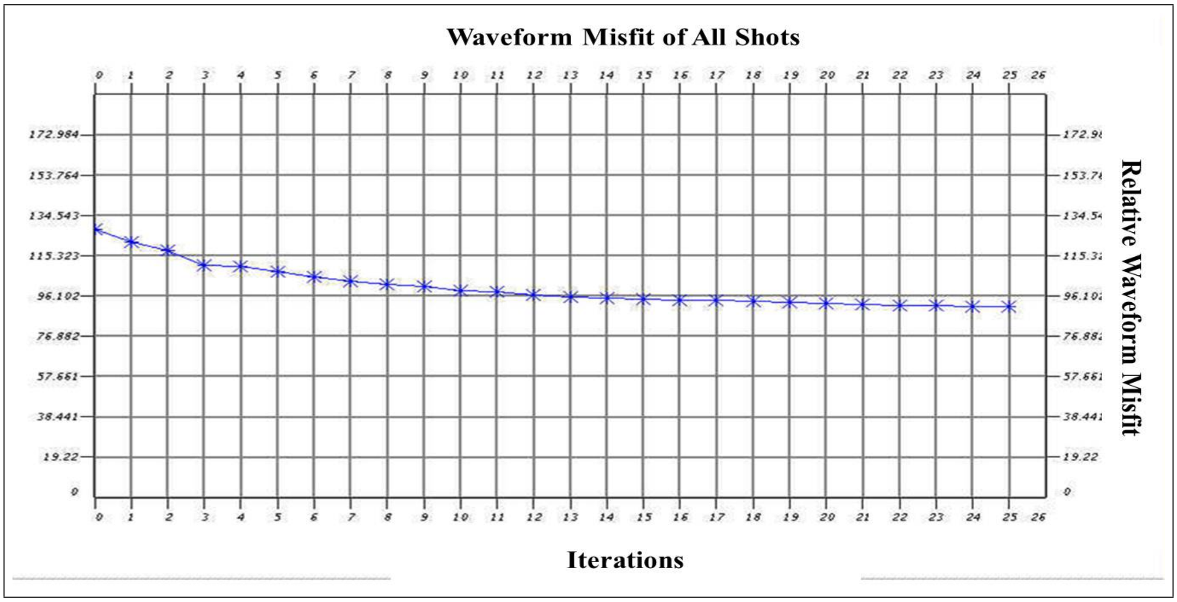

Figure 4.25: Perform EAT inversion

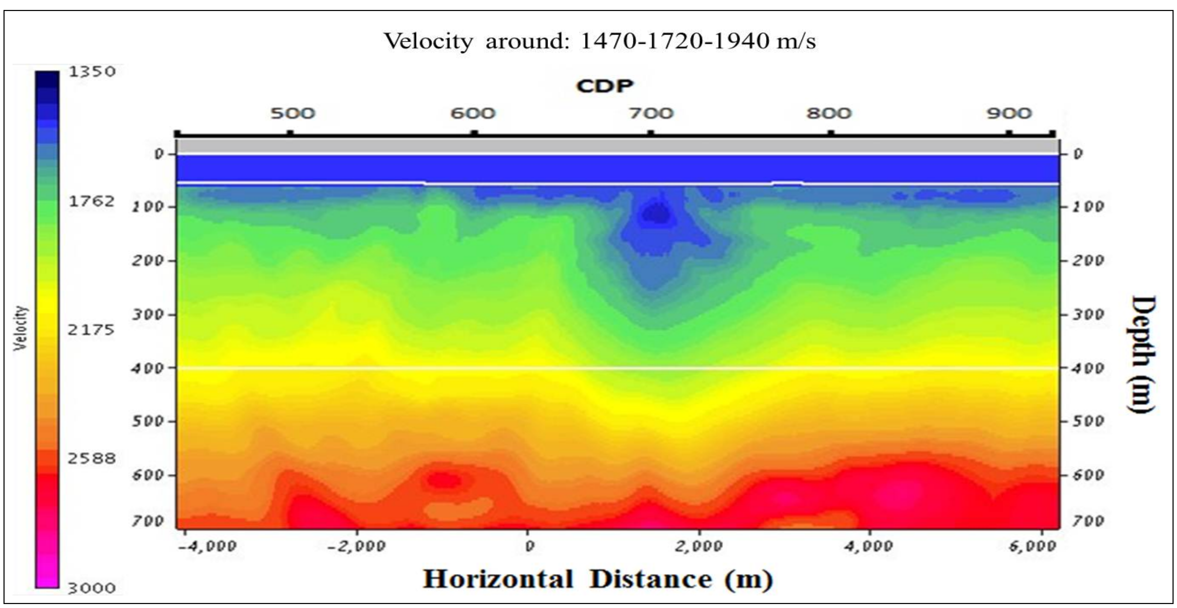

Figure 4.26: Final EAT velocity model after 25th iterations of waveform tomography inversion. Three white lines are final datum on the top, ocean bottom in the middle, and intermediate datum at the bottom respectively.

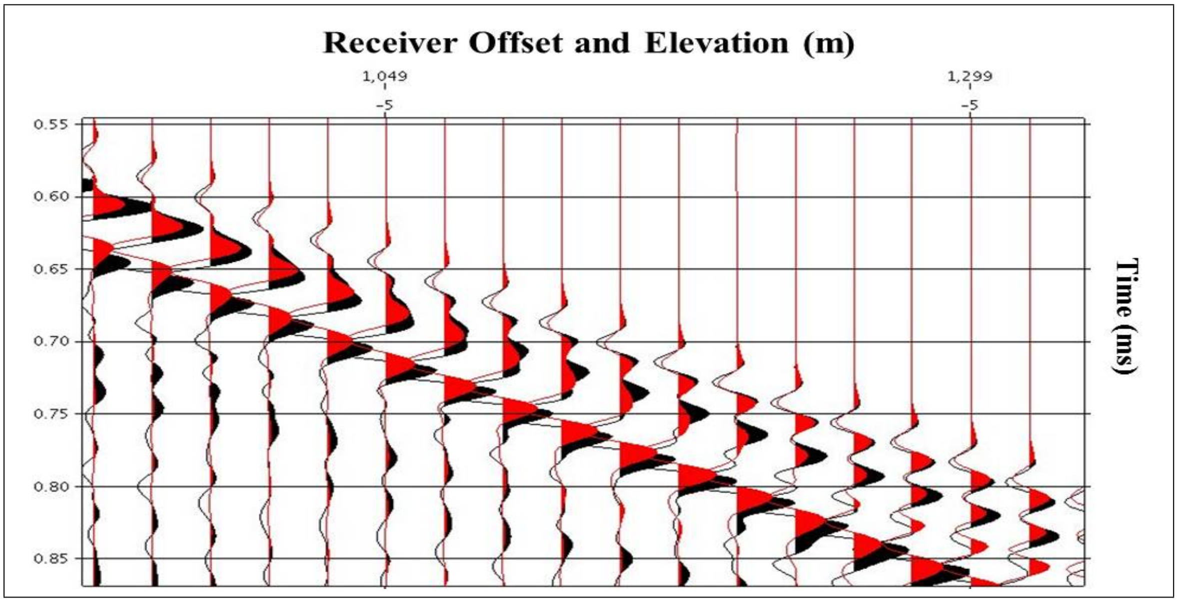

Figure 4.27: Overlay of synthetic data with seismic data for shot 20. Black are early-arrival seismic data. Red are calculated early-arrival waveforms.

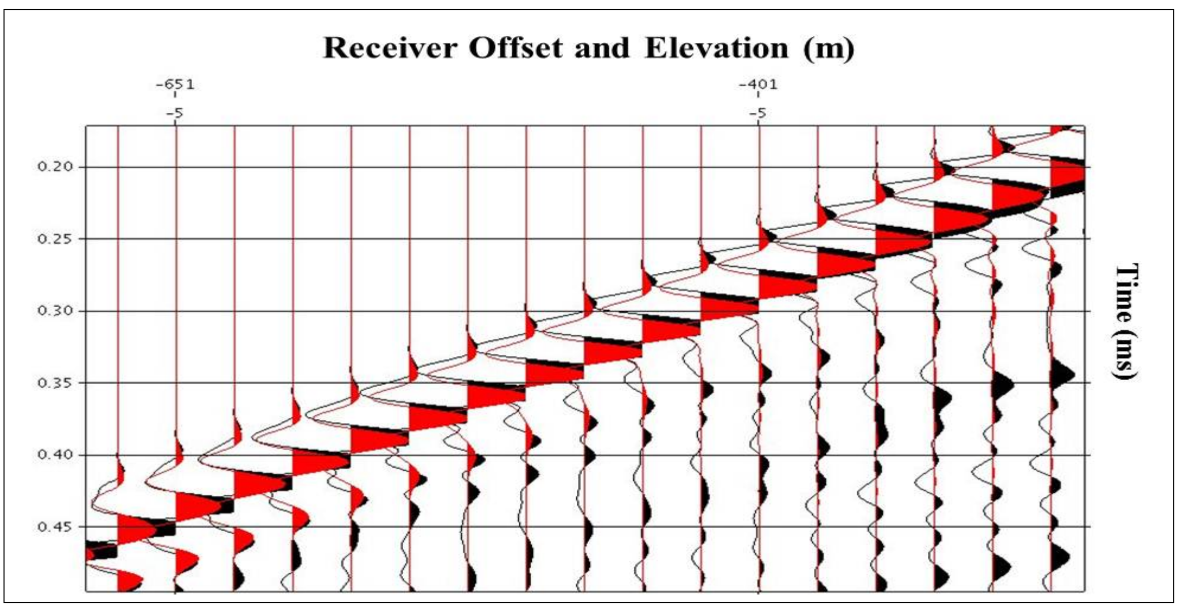

Figure 4.28: Overlay of synthetic data with seismic data for shot 50. Black are early-arrival seismic data. Red are calculated early-arrival waveforms.

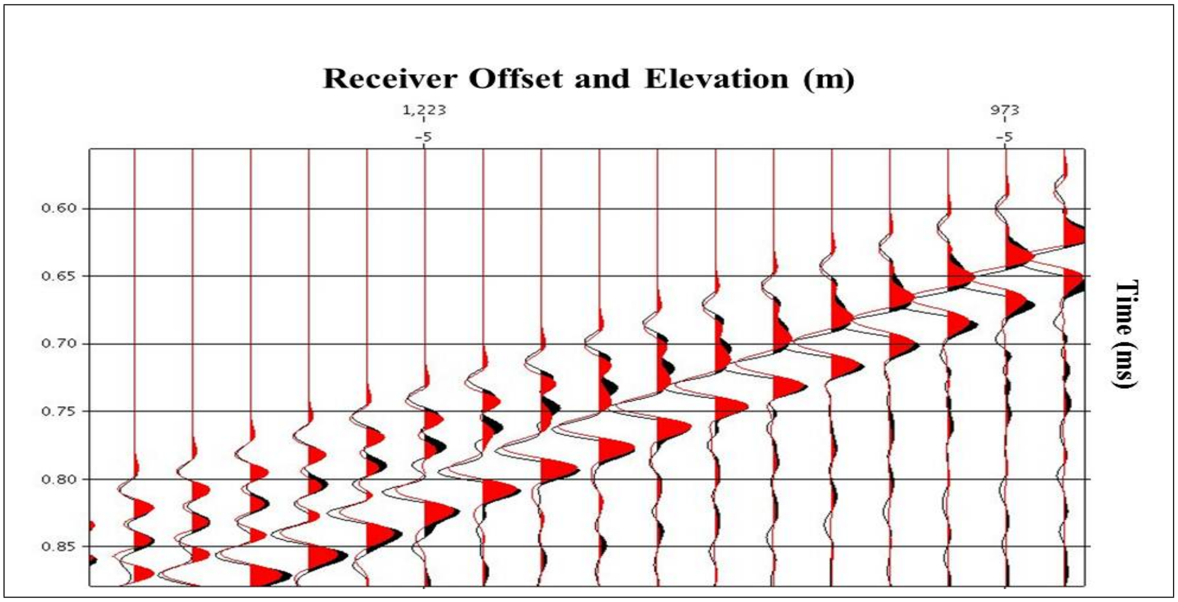

Figure 4.29: Overlay of synthetic data with seismic data for shot 60. Black are early-arrival seismic data. Red are calculated early-arrival waveforms.

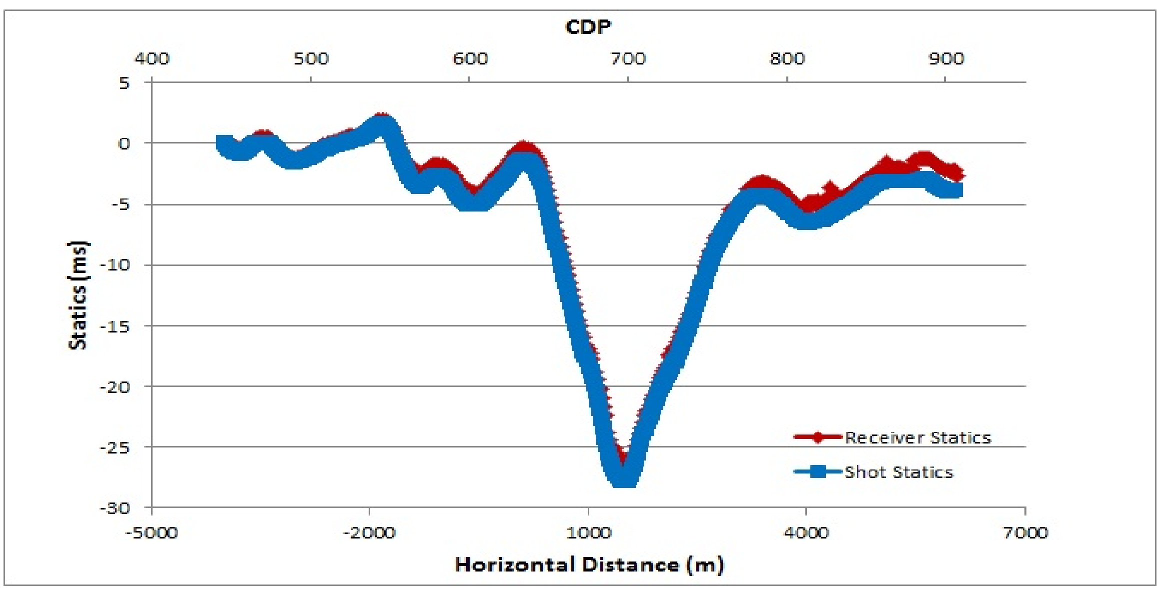

Figure 4.30: Statics of waveform tomography inversion. Red are receivers and blue are shots.

Chapter 5

COMPARISON OF RESULTS

5.1 2D Onshore Data in Peru

As was mentioned in the introduction, the near-surface velocity distortion addressed here leads to static corrections significantly longer than a cable length. The shorter period statics were calculated from reflection statics, and the dynamic corrections (reflection velocity analysis and application) were made after applying the RDT solution to remove an estimate of the structural impact from the seismic data. The differing long-period statics computed from each method were compared to the RDT solution by either removing the RDT statics altogether (the no-statics case), applying the FAT solution to the no-statics case, or applying the EAT statics to the no-statics case. The variation in the long-period statics solutions as can be seen below was not so significant as to warrant a re-interpretation of the reflection velocity field.

Judging the relative effectiveness of each solution would typically be accomplished with the knowledge base that an explorationist operating in the area would have:

a detailed knowledge of the geology of the area, well control, perhaps shot hole information, and other 2D and 3D lines that tie the ones in this study. Unfortunately none of this is available for this study, so an examination of the resulting stacks is the best option.

5.1.1 Velocity Comparison of 2D Onshore Data in Peru

To begin with, let's start with a comparison of the velocity models from each technique. For ease of review, Figure 5.1 to 5.3 are repeats of Figure 3.12, Figure 3.15 and Figure 3.30.

All three velocity models delineate lateral velocity variations in near-surface structures. But RDT velocities are much smoother than FAT and EAT. For instance, in the high velocity region (from CDP 1000 to 1400) , velocities spread from 2350 m/s to 2430 m/s in RDT model. EAT describes a more laterally extended high velocity area than RDT, also a higher velocity range from 2400 m/s to 2740 m/s. FAT extends the high velocity portion to the largest expanse, and velocities varies from 2700 m/s to 3200 m/s.

In the low velocity region between CDPs 1390 and 1790, RDT again depicts the smoothest velocity change among three models, varying from 1375 m/s to 1460 m/s. FAT finds a much larger and lower range of velocities, from 850 m/s to 1300 m/s. Among these three velocity models, EAT produces the lowest velocity zone, covering from 870 m/s to 1100 m/s in the shallowest zone.

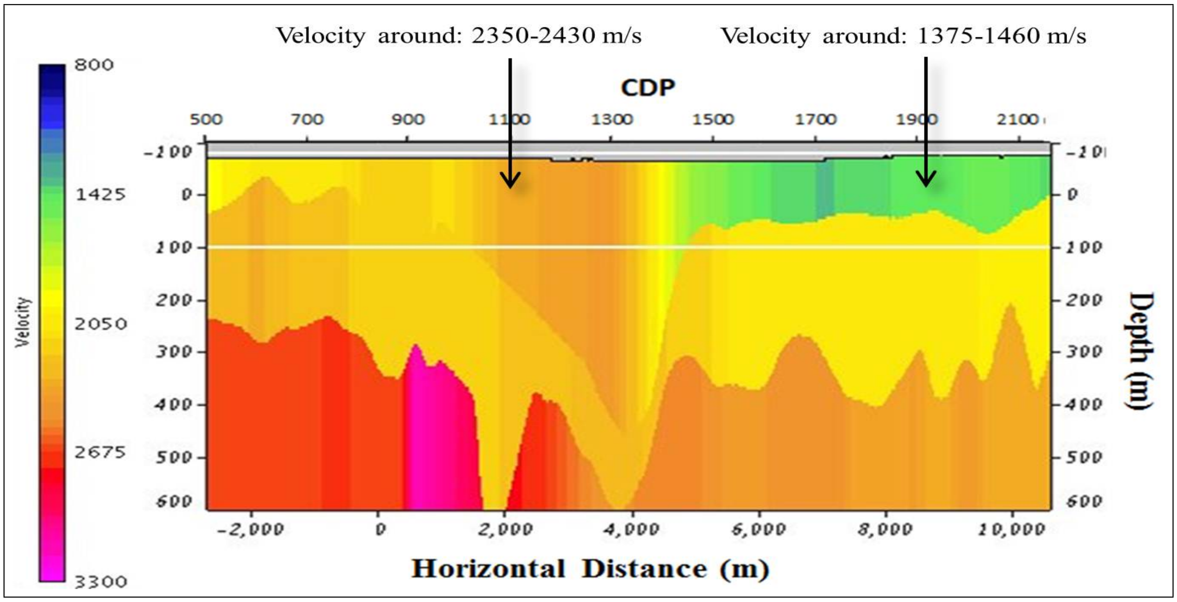

Figure 5.1: Three-Layer RDT velocity model. Two white lines are final datum on the top and intermediate datum at the bottom respectively.

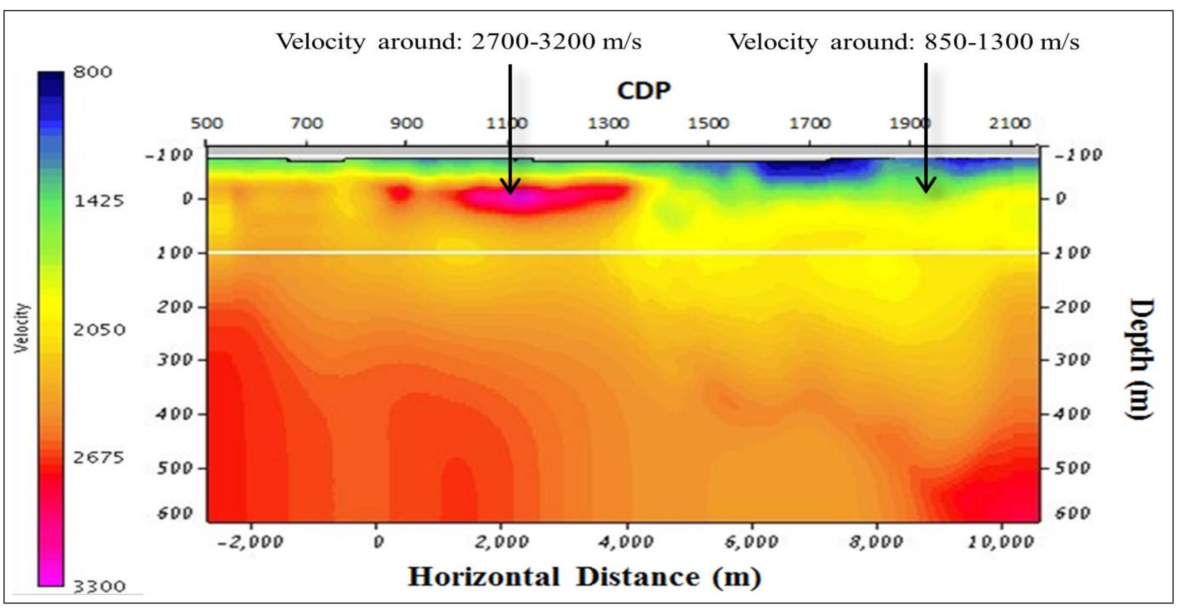

Figure 5.2: FAT velocity model inversed from delay-time model. Model grid size is 5m*5m. Two white lines are final datum on the top and intermediate datum at the bottom respectively.

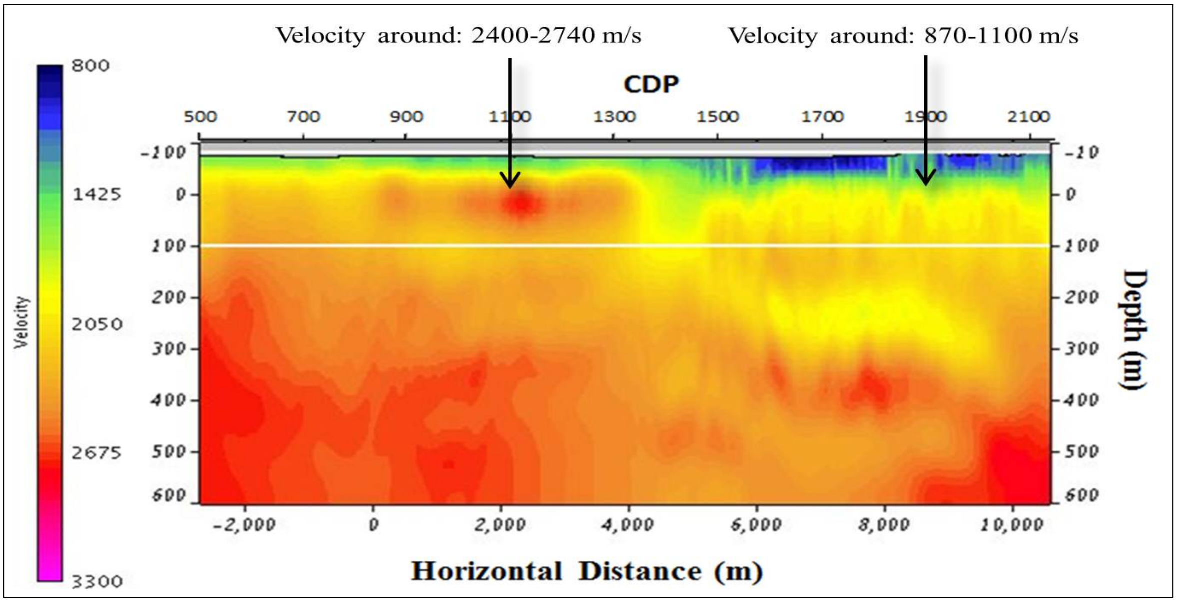

Figure 5.3: EAT velocity model after 25th iterations of waveform tomography inversion. Two white lines are final datum on the top and intermediate datum at the bottom respectively.

5.1.2 Statics Comparison of 2D Onshore Data in Peru

The shot and receiver statics comparison of these three methods are shown in Figure 5.4 - 5.5 where the statics in ms are plotted along shot and receiver stations. The blue plot is for the delay time solution, the red for the first arrival traveltime, and the green for the waveform inversion.

The biggest difference among the three statics solutions is between shot stations 26775 and 28775, related to receiver stations between 2678 and 2978. This discrepancy is associated with the low-velocity abnormality seen above in the velocity fields and corresponds to the CDP range mentioned above, CDP 1390 to 1790. The FAT and RDT statics are quite similar, whereas the EAT results are 10ms less.

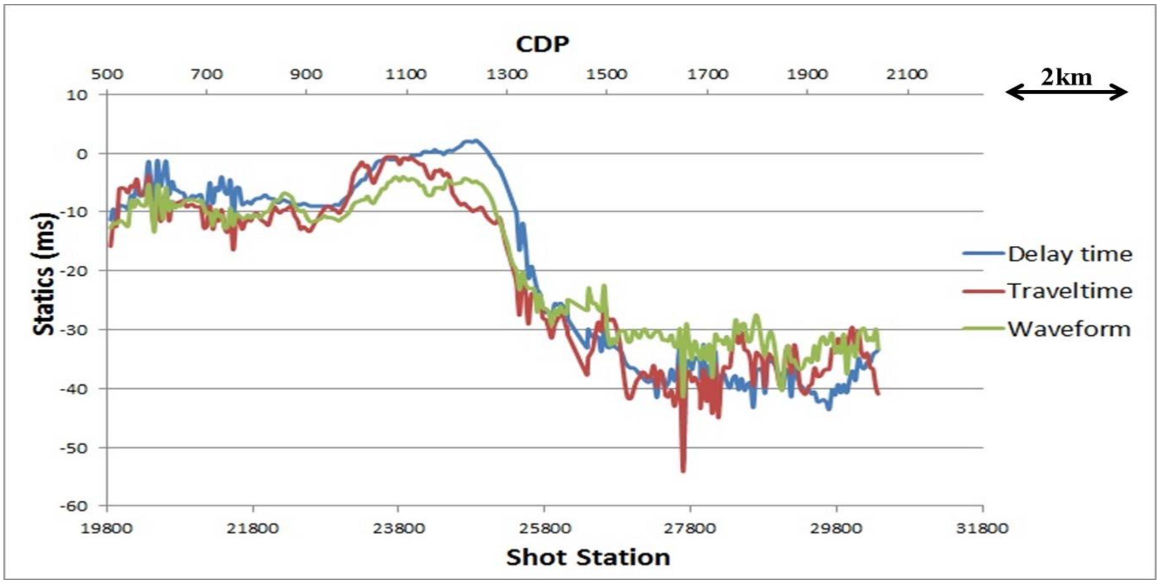

Figure 5.4: Shot Statics Comparison: blue is RDT, red is FAT, and green is EAT.

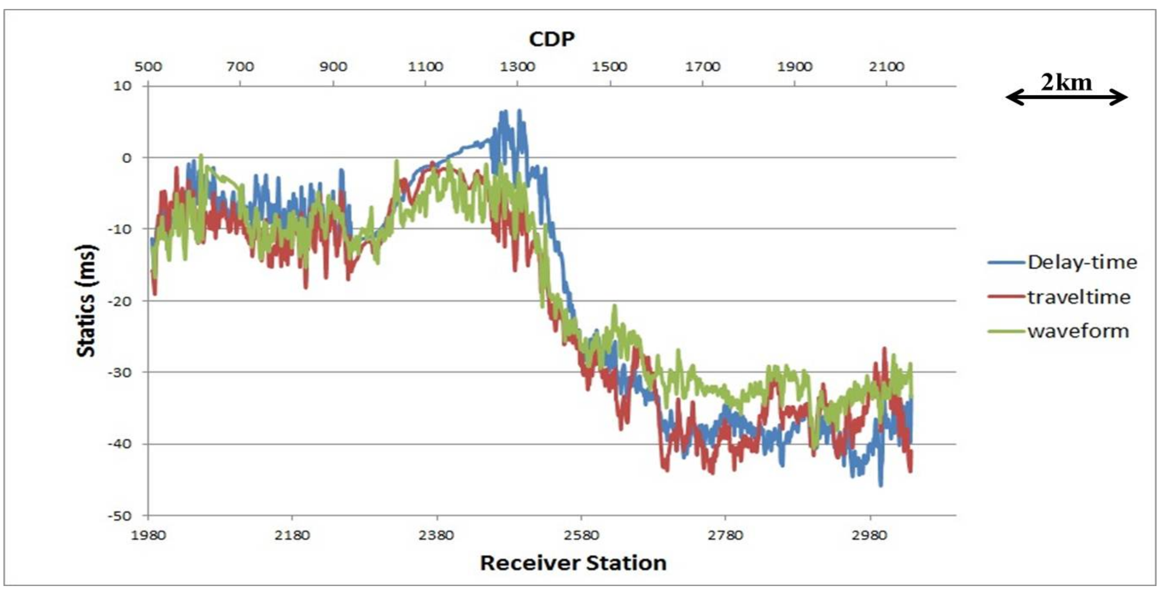

Figure 5.5: Receiver Statics Comparison: blue is RDT, red is FAT, and green is EAT.

5.1.3 CDP Comparison of 2D Onshore Data in Peru

Figure 5.6 shows CDP 1467 with statics applied from each of the methods. The second panel is the result of RDT. Red dots indicate the two events. In particular note the flattened event around 200ms and 350ms. RDT was then removed, and this is displayed in the first panel as"NO Statics". The flattened event mentioned previously has been shifted later and has lost its continuity. FAT was applied in the third panel, then EAT instead of FAT in the fourth. The results of the last three panels just show the bulk shift of the CDPs up and down depending on statics applied. The gathers remain flat as the velocities and short period statics remain the same.

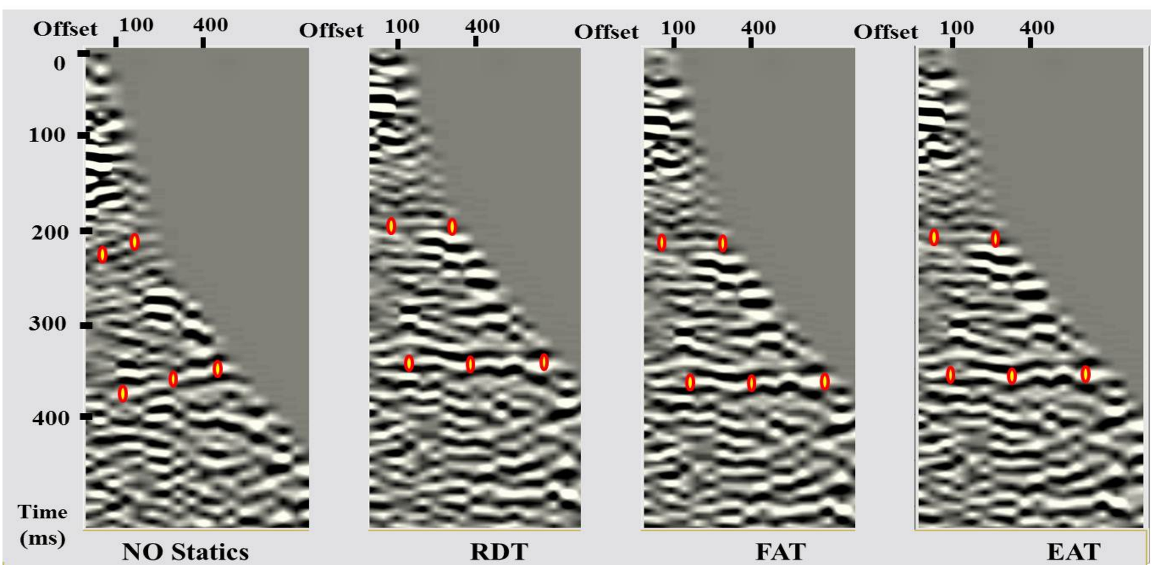

Figure 5.6: From left to right, they are CDP 1467 comparison of no long wavelength statics, RDT statics, FAT statics, and EAT statics respectively. Red dots indicate the two events.

5.1.4 Stack Comparison of 2D Onshore Data in Peru

Using the same methodology as for the CDPs above, stacks were produced for no statics (Figure 5.7), RDT (Figure 5.8), FAT (Figure 5.9), and EAT (Figure 5.10). Zoom comparison sections were then made and shown in Figures 5.11-5.14. The early part of the section was displayed as this is where the impact of the statics is most easily seen. A horizontal blue line is drawn on these zoomed sections as a flatness reference. A red window is drawn on each of the figures to show the area where FK analyses were performed. Figure 5.11 compares the long-period RDT statics removed in the upper section to the application of RDT in the lower section. Besides the general pull-up of events in the lower section, the event package round 200ms on the left hand side appears a bit flatter and the events around 450ms are more continuous as well.

In Figure 5.12 the stack of the RDT statics on top are compared with the FAT statics on the bottom. The solutions from the two techniques were similar, as are the stacks. In comparing the RDT with the EAT in Figure 5.13 (EAT on the bottom), there are some subtle differences. The dipping noise around CDP 1480 and 250ms has been stacked out on the EAT section, and also the event around 450ms is stronger, flatter, and more continuous in the left side of the section between CDPs 1200 and 1580. Similar observations can be made with respect to Figure 5.14 as well, where the FAT is plotter in the upper section and EAT in the lower. Figures 5.15-5.18 show FK plots over the windowed areas shown in plots above. Frequency is plotted on the vertical axis and wavenumber on the horizontal axis. Figure 5.15 is for the case of no-statics, Figure 5.16 for RDT, Figure 5.17 for FAT, and Figure 5.18 for

EAT. As can be seen for the figures, EAT focuses the energy better along the zero wavenumber line, indicating better flatness and event focus.

As discussed earlier, without additional data such as line ties and wells it is difficult to say which technique produces a better solution, but the greater continuity, stack response, and general flatness is strongly suggestive that EAT is is superior.

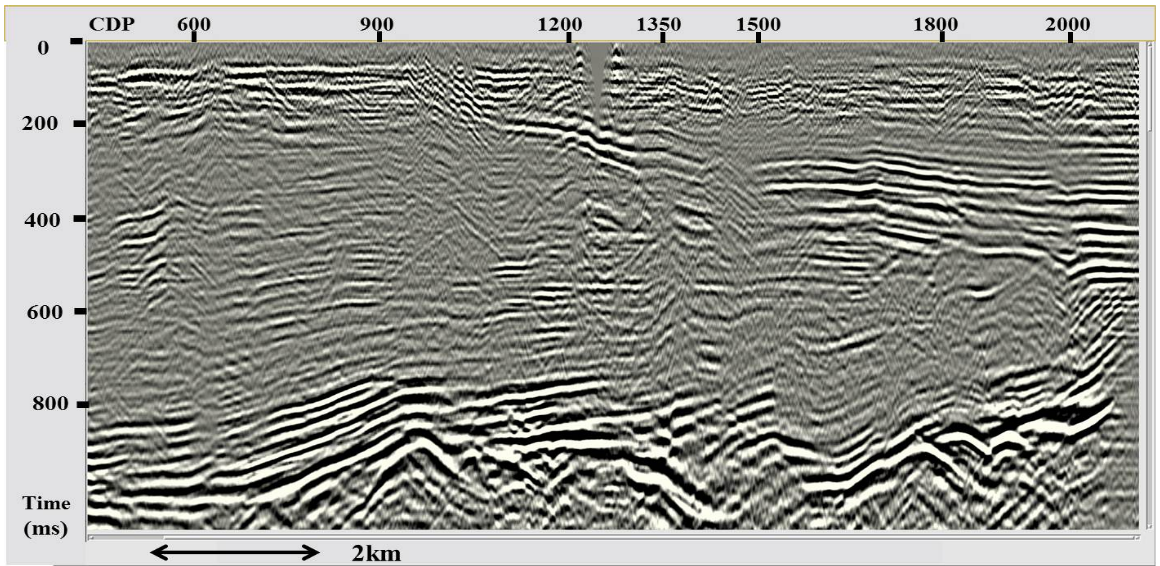

Figure 5.7: Stack of no long wavelength statics. X axis is CDP number, vertical axis is time in ms.

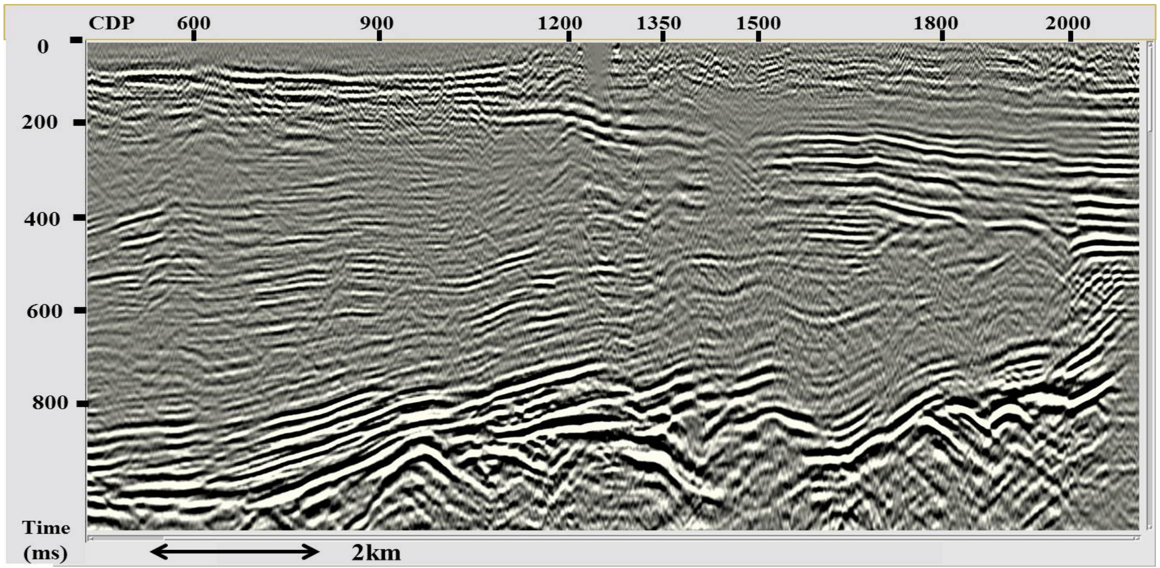

Figure 5.8: Stack of RDT statics. X axis is CDP number, vertical axis is time in ms.

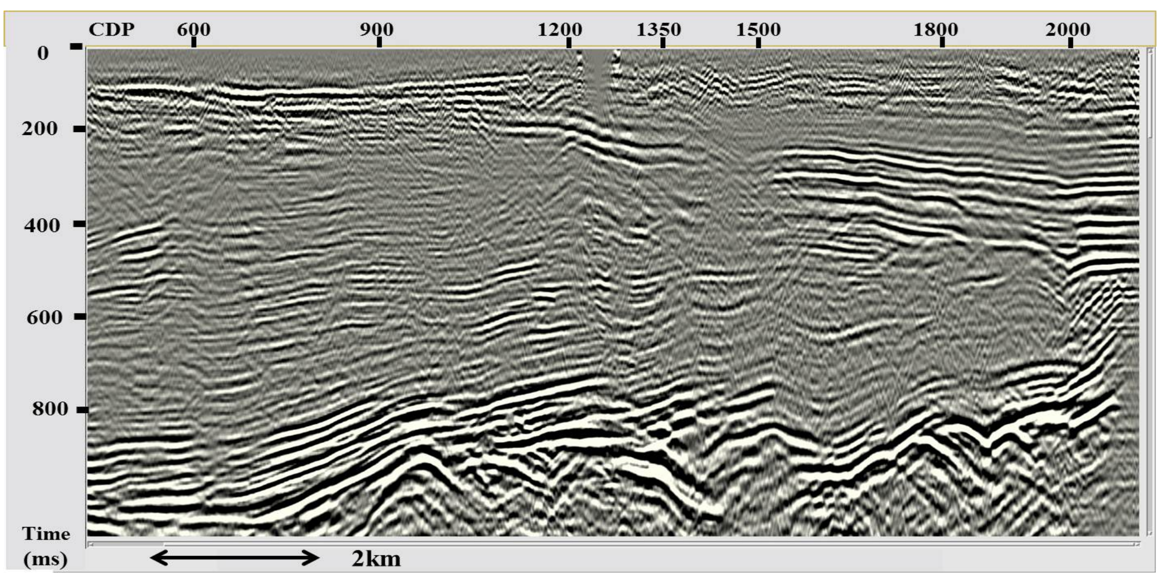

Figure 5.9: Stack of FAT statics. X axis is CDP number, vertical axis is time in ms.

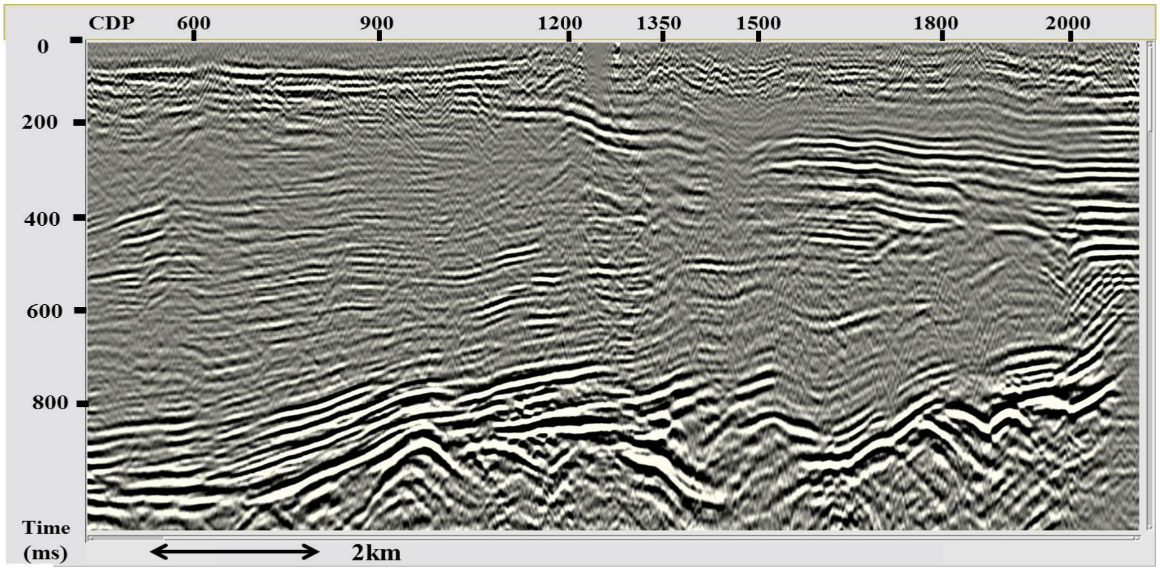

Figure 5.10: Stack of EAT statics. X axis is CDP number, vertical axis is time in ms.

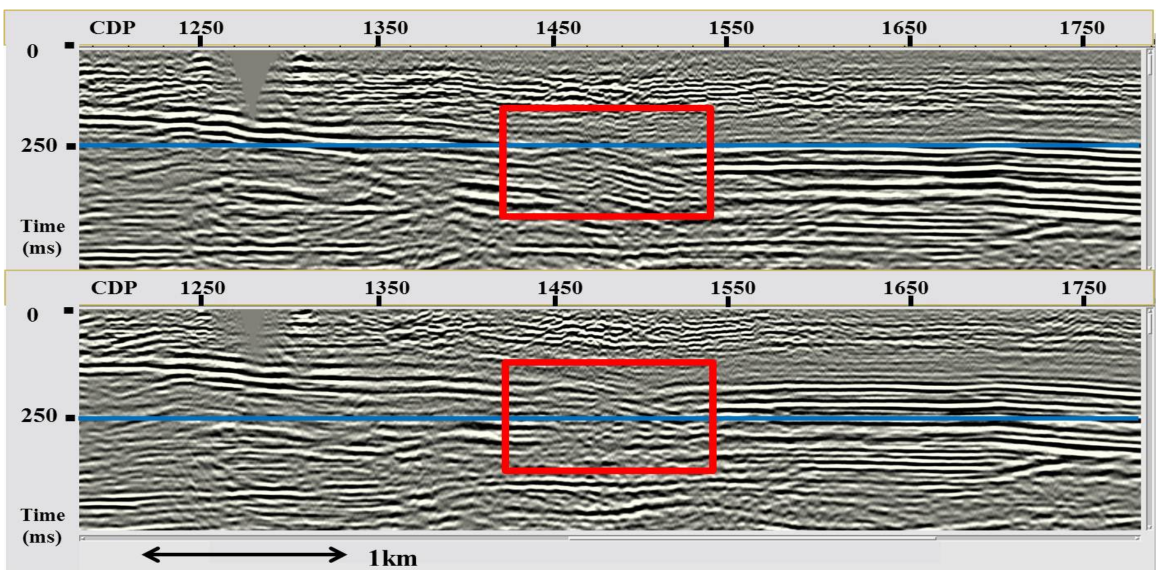

Figure 5.11: Stack comparison of no long wavelength statics on the top vs RDT statics at the bottom. X axis is CDP number, vertical axis is time in ms.

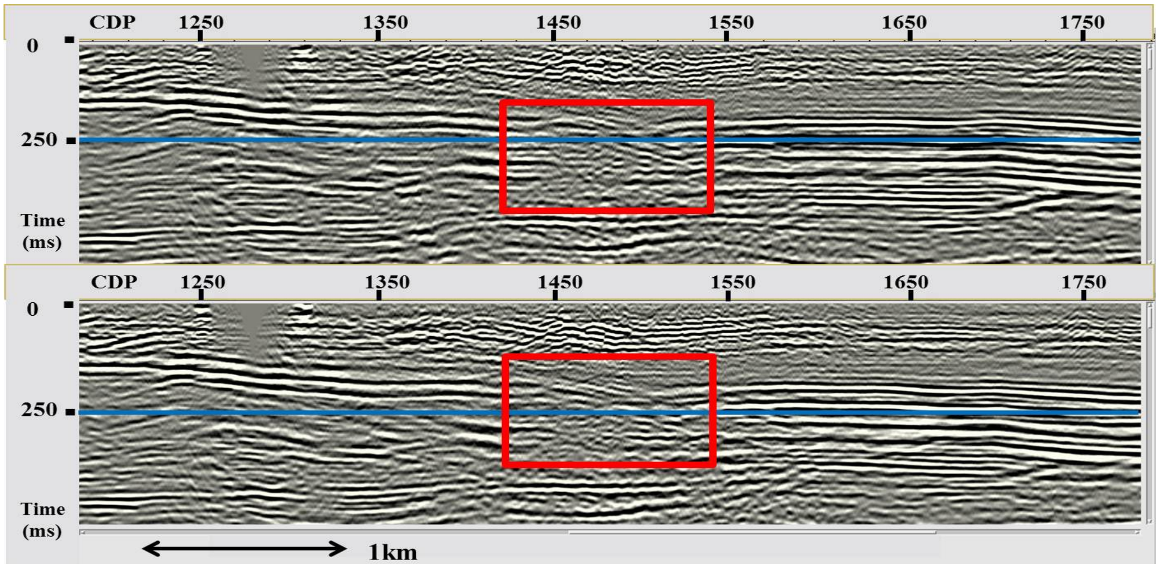

Figure 5.12: Stack comparison of RDT on the top vs FAT at the bottom statics. X axis is CDP number, vertical axis is time in ms.

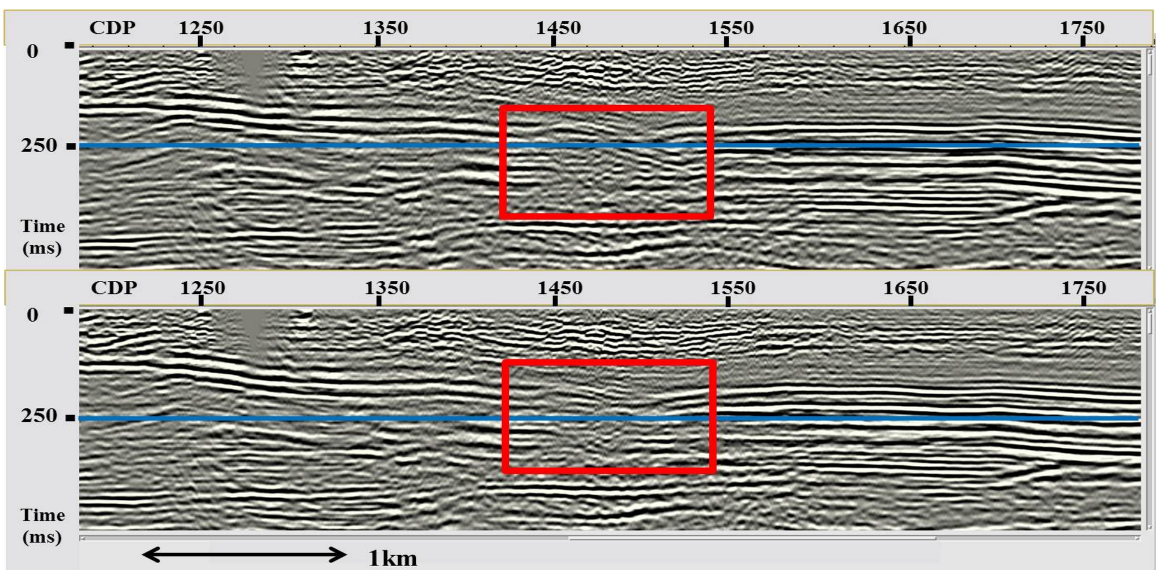

Figure 5.13: Stack comparison of RDT on the top vs EAT at the bottom statics. X axis is CDP number, vertical axis is time in ms.

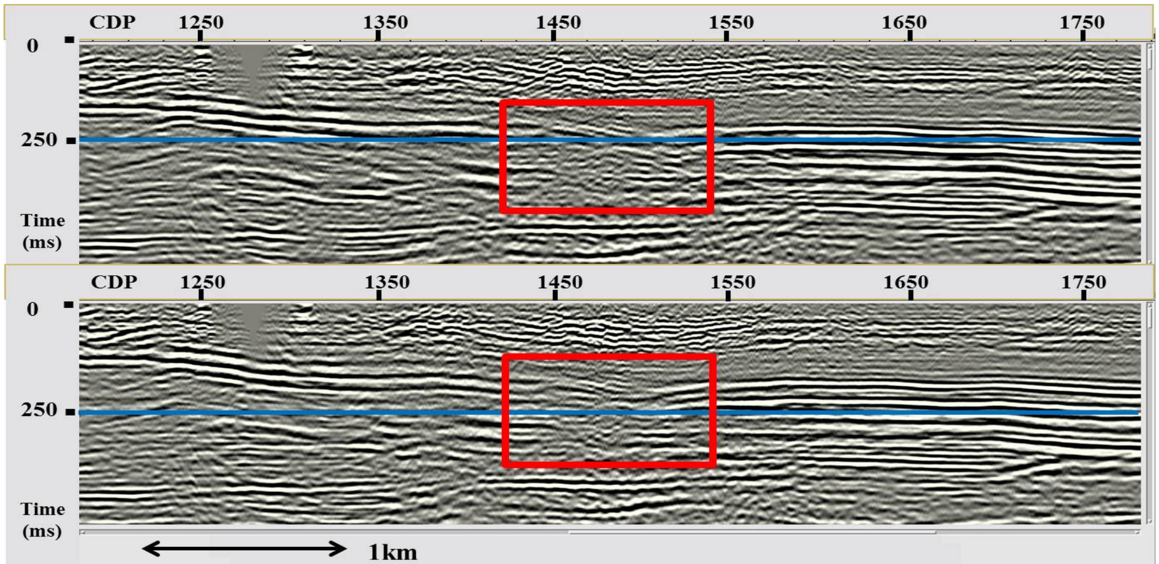

Figure 5.14: Stack comparison of FAT on the top vs EAT at the bottom statics. X axis is CDP number, vertical axis is time in ms.

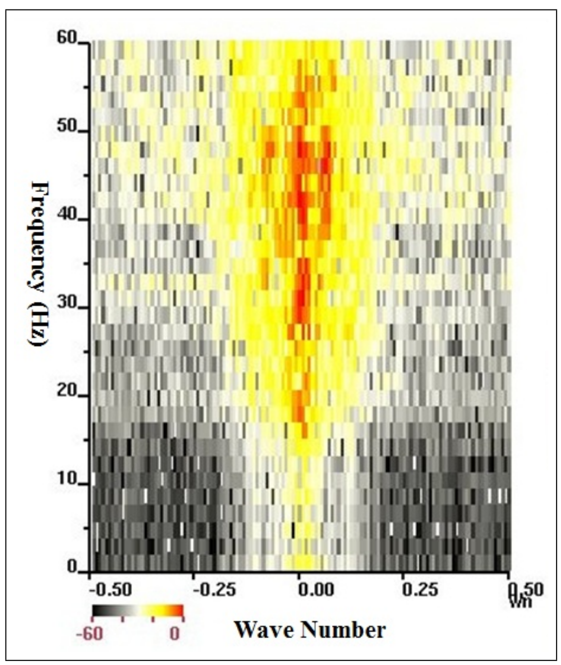

Figure 5.15: FK analysis of no statics. X axis is wave number, vertical axis is frequency.

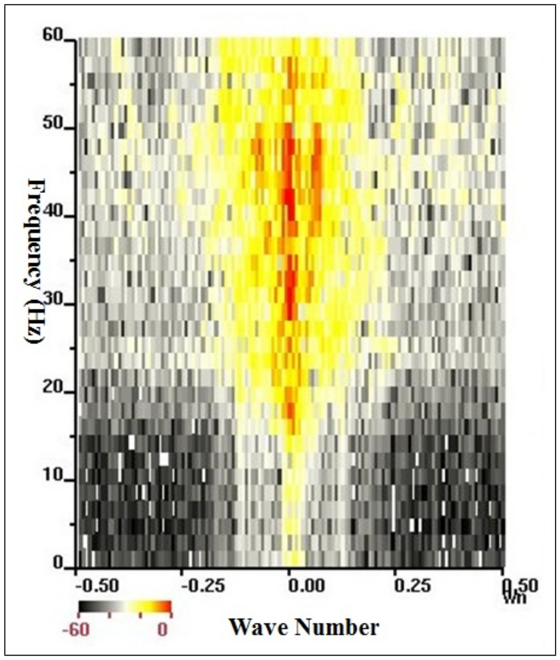

Figure 5.16: FK analysis of RDT. X axis is wave number, vertical axis is frequency.

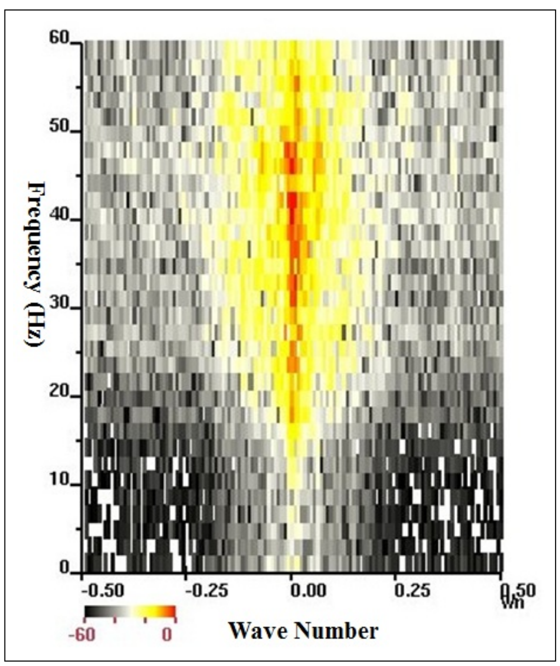

Figure 5.17: FK analysis of RDT. X axis is wave number, vertical axis is frequency.

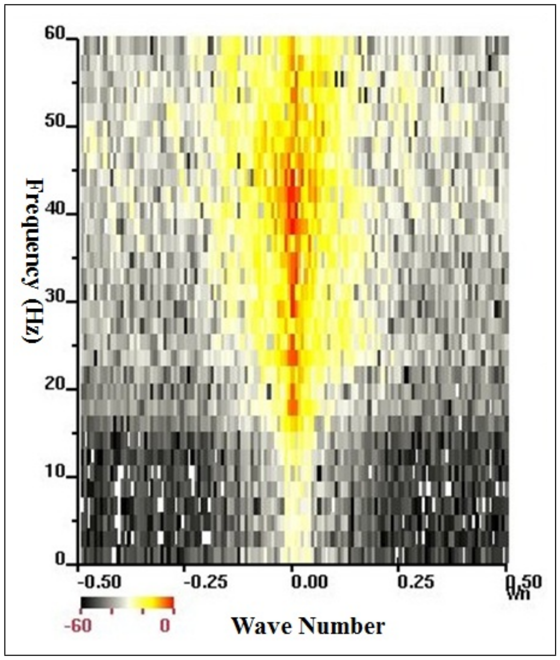

Figure 5.18: FK analysis of RDT. X axis is wave number, vertical axis is frequency.

5.2 2D OBC Data in Malaysia

5.2.1 Velocity Comparison of 2D OBC Data in Malaysia

As in the discussion of the Peru dataset, for ease of comparison, Figures 5.19 to 5.21 are repeated versions of Figures 4.11, Figure 4.14 and Figure 4.25. The velocity anomaly due to the gas is mostly between CDPs 530 and 790. Considering the size of seismic survey and the target region, the velocity models were limited from -4000 meters to 6000 meters, the length of the receiver cable.

Though RDT's near-surface velocity covers nearly the same variations (from 1515 m/s to 1940 m/s) with FAT and EAT, its velocity model is still the roughest among three models, because of the vertical velocity distribution. In this gas cloud situation, significant velocity variations occur to greater depth than typical low-velocity situations in land, leading to a much less realistic first layer in refraction modeling. Since marine structures in our case are relatively smooth except for gas cloud region, the velocity models of FAT and EAT would seem more likely. In addition, FAT's velocity model is the smoothest among all of them. The results of EAT delineates in more detailed near-surface velocity structures than FAT, as well as somewhat lower velocity in gas cloud area, varying from 1470 m/s to 1940 m/s.

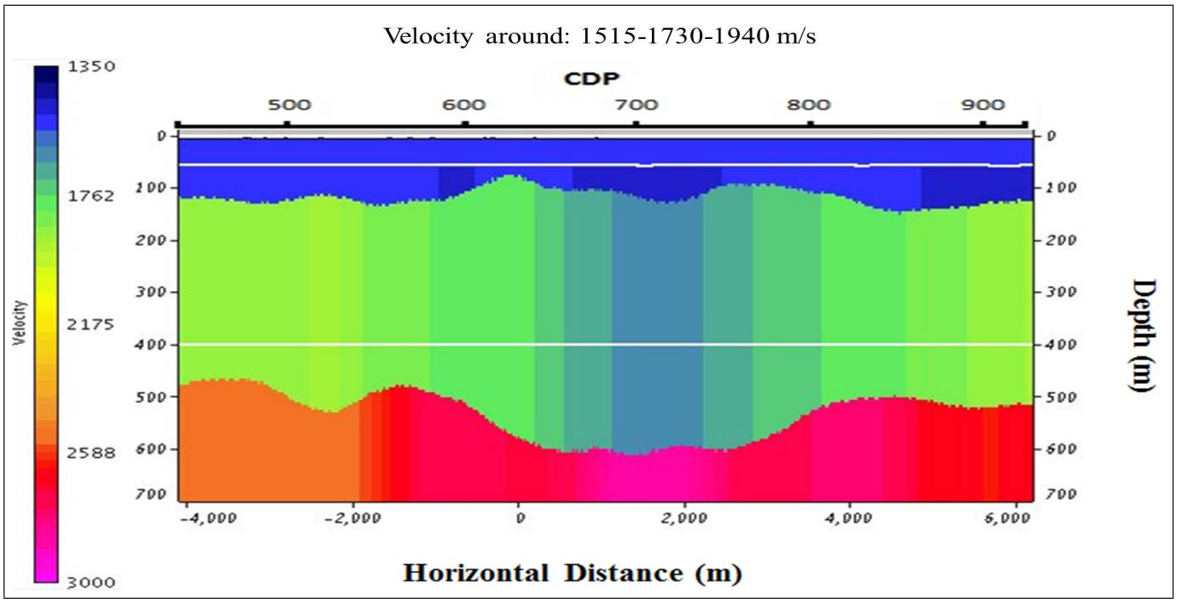

Figure 5.19: Three-Layer RDT velocity model. Three white lines are final datum on the top, ocean bottom in the middle, and intermediate datum at the bottom respectively.

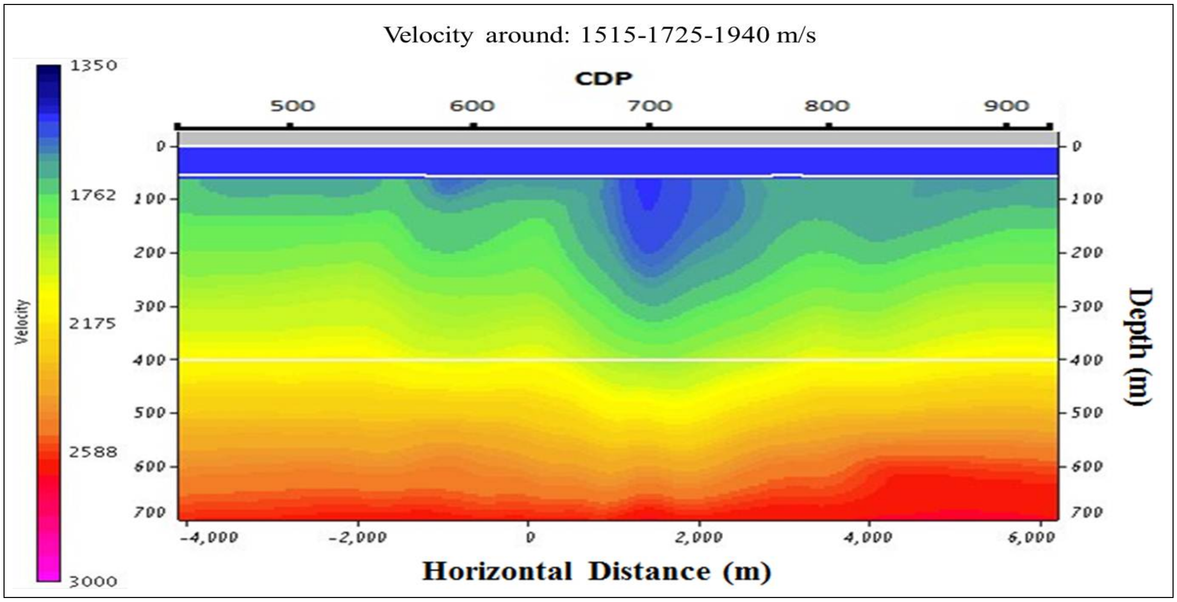

Figure 5.20: FAT velocity model inversed from delay-time model. Model grid size is 5m*5m. Three white lines are final datum on the top, ocean bottom in the middle, and intermediate datum at the bottom respectively.

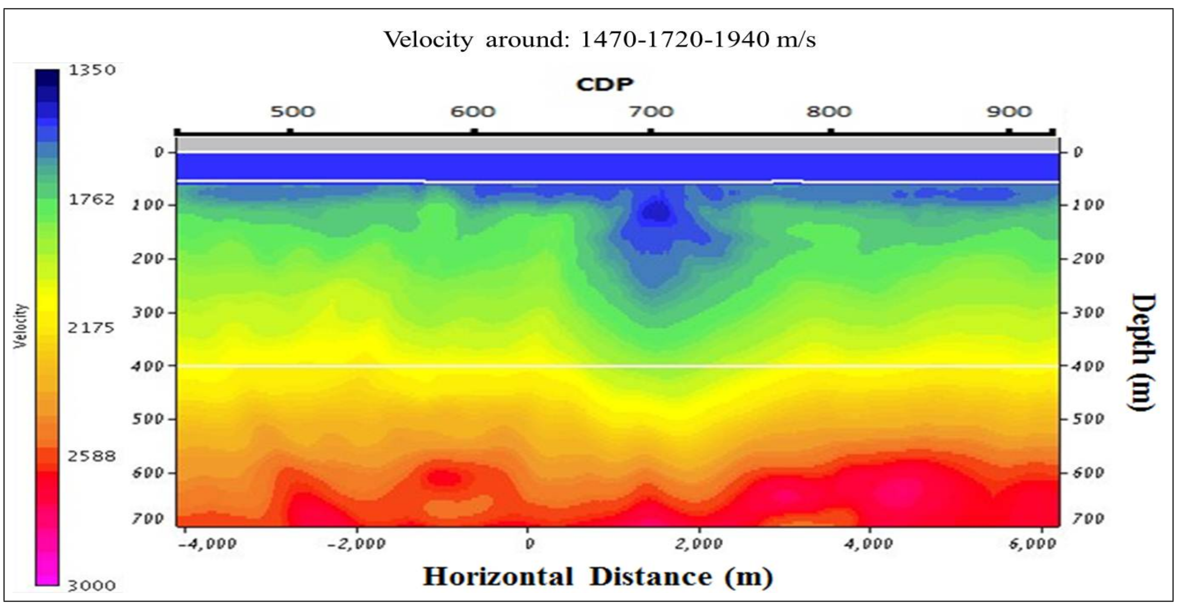

Figure 5.21: EAT velocity model after 25th iterations of waveform tomography inversion. Three white lines are final datum on the top, ocean bottom in the middle, and intermediate datum at the bottom respectively.

5.2.2 Statics Comparison of 2D OBC Data in Malaysia

Figures 5.22 and 5.23 compares the statics results from the three methods. All of the statics are referenced to sea level. The largest difference is that the statics from the RDT technique are spread out somewhat more horizontally and is slightly smaller than those of the other two. This is due to the inability of RDT to model quickly varying lateral velocity changes.

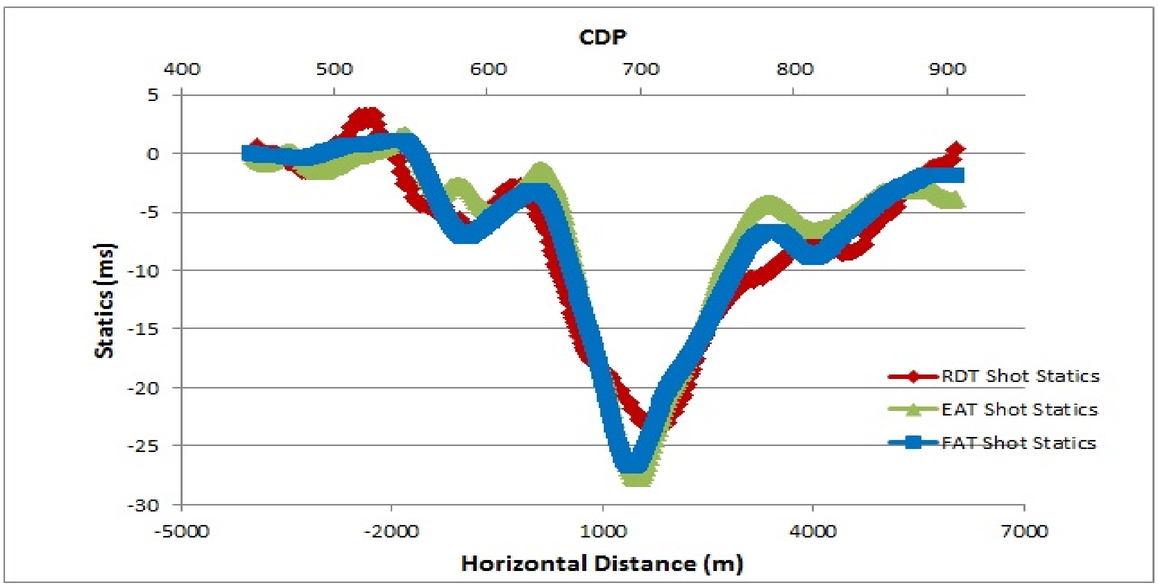

Figure 5.22: Shot statics comparison: blue is FAT, red is RDT, and green is EAT.

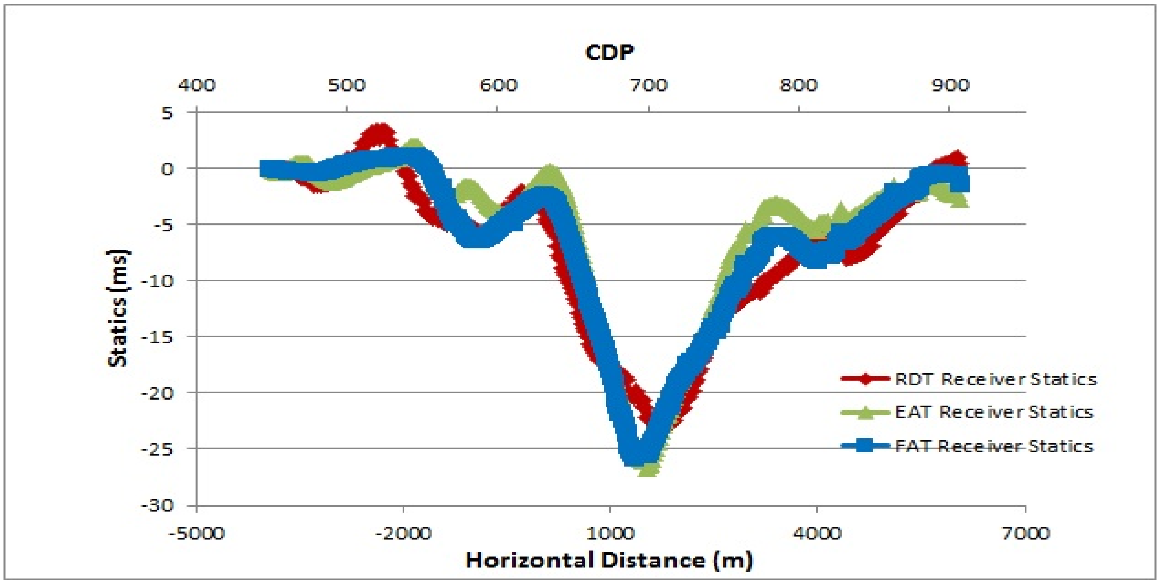

Figure 5.23: Receiver statics comparison: blue is FAT, red is RDT, and green is EAT.

5.2.3 CDP Comparison of 2D OBC Data in Malaysia

CDP 680 from the middle of the gas zone is shown in Figure 5.24. The second panel is the RDT solution combined with velocity application. The first panel is without any statics, and the third and fourth panels are the CDP with FAT and EAT applied instead of RDT. In this case long-period statics are long enough that they have no effect within the CDP as they did in the Peru dataset. Basically the events are simply shifted up and down depending on the shot and receiver statics applied to the CDP.

5.2.4 Stack Comparison of 2D OBC Data in Malaysia

Figures 5.25 through 5.28 show stacks of the dataset with no statics, RDT, FAT, and EAT. The anticlinal structure has been greatly exaggerated with the application of

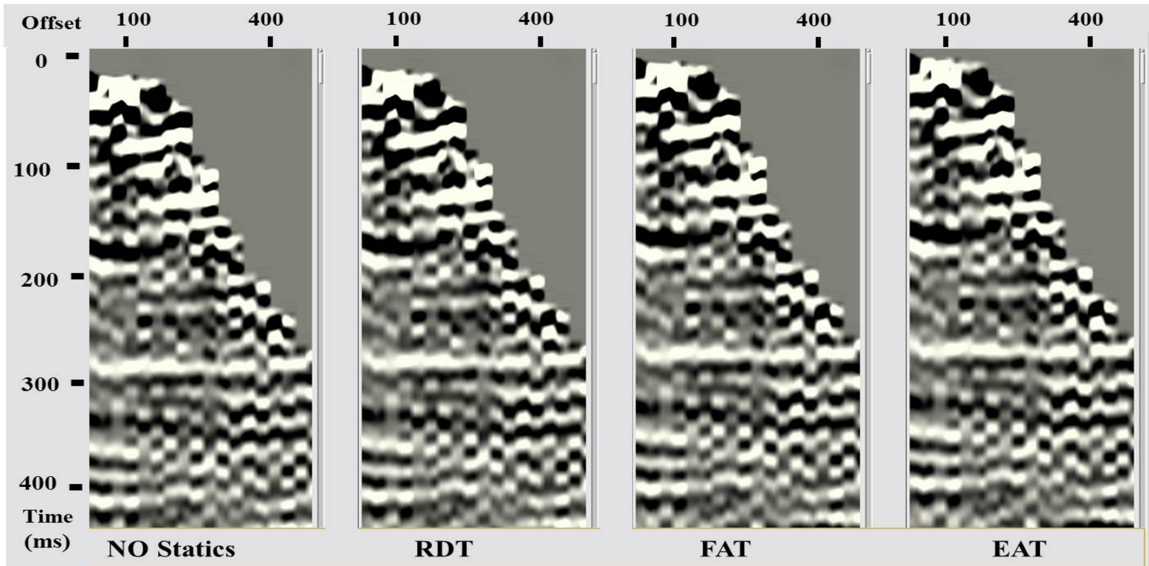

Figure 5.24: From left to right, they are CDP 680 comparison of no statics, RDT statics, FAT statics, and EAT statics respectively.

the long-wavelength statics. The tight horizontal scale of the plots further enhances this. Clearly the proper approach would be to use the shallow velocity fields derived in this study as part of a depth migration strategy in which the structure would appear in depth without so much pull up. This would be a good direction for future work.

However, by examining zoom comparisons as shown in Figures 5.29 to 5.32, some observations as to the impact of the statics on the core of the anticlinal structure can be made. As was done in the Peru dataset a horizontal line is plotted for structural reference and again the windows indicate the areas for FK analyses. In Figure 5.29 the upper section is displayed without statics, and the lower section with statics from RDT. The overall anticlinal structure is better flattened with the RDT but the other differences are subtle. In examining Figure 5.32 which compares the RDT result to the FAT result on the lower section, we also see the event in the middle at time 185ms is pulled up closer to flat in the FAT portion. The same can be said for the comparison in Figure 5.31, where the RDT results on plotted on the top and EAT is on the bottom. In Figure 5.32 with RDT on the top and EAT on the bottom, and perhaps the event in the middle is slightly better flattened. Figures 5.33 to 5.36 show the FK plots for no statics, RDT, FAT, and EAT respectively. Again they suggests EAT does a better job focusing the events along the zero wavenumber axis.

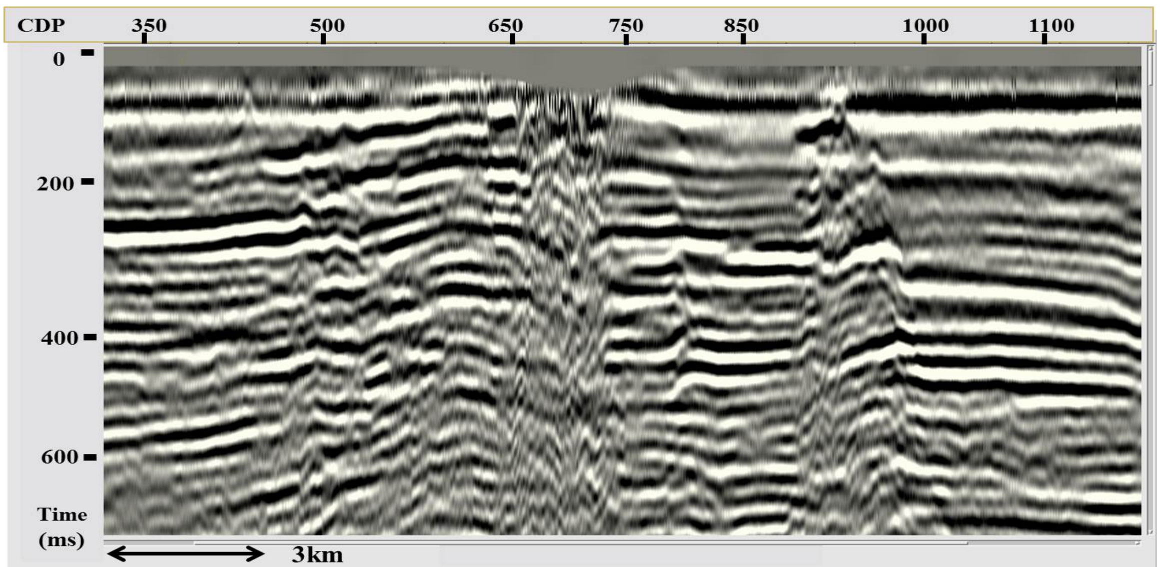

Figure 5.25: Stack of no statics. X axis is CDP number, vertical axis is time in ms.

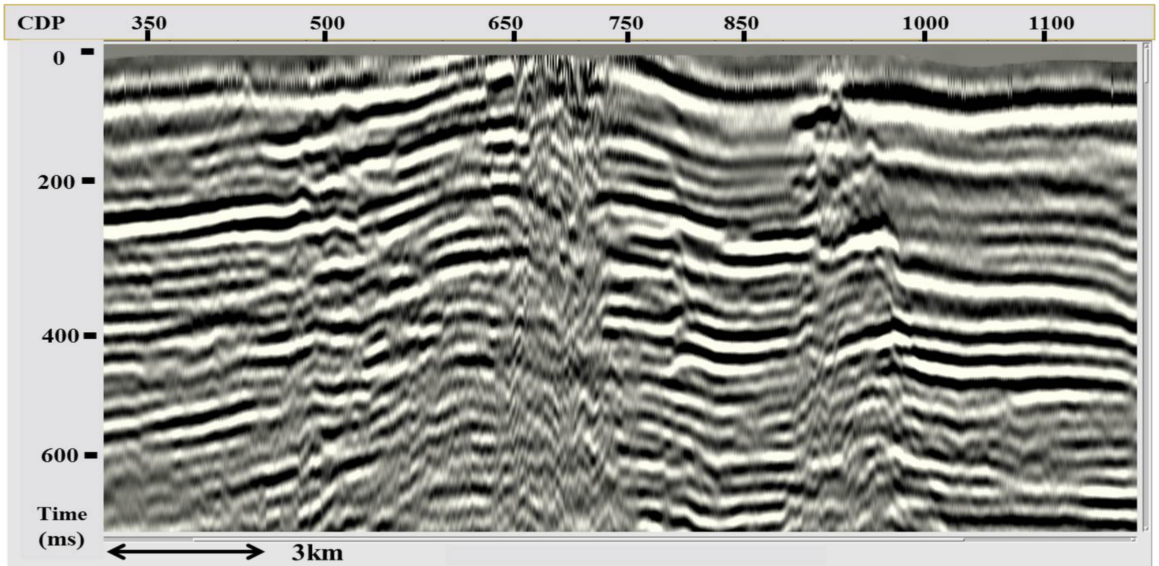

Figure 5.26: Stack of RDT statics. X axis is CDP number, vertical axis is time in ms.

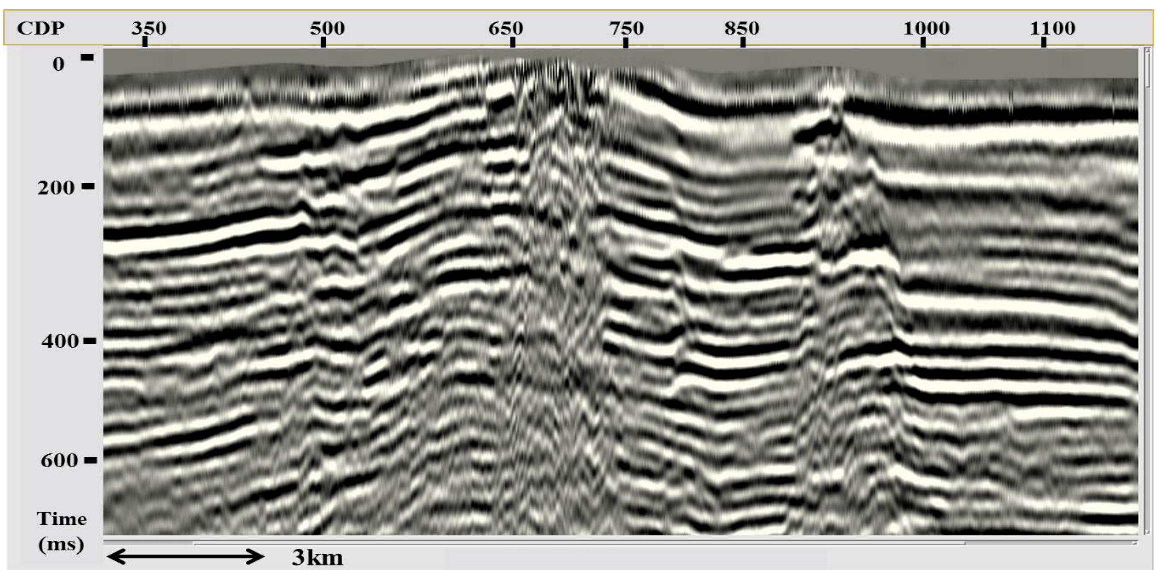

Figure 5.27: Stack of FAT statics. X axis is CDP number, vertical axis is time in ms.

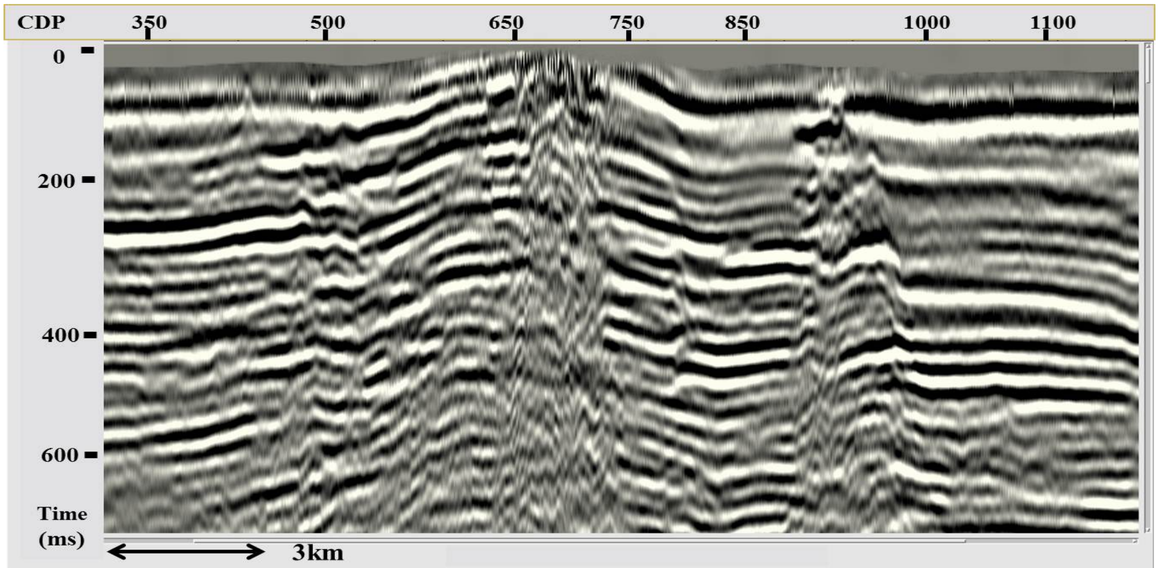

Figure 5.28: Stack of EAT statics. X axis is CDP number, vertical axis is time in ms.

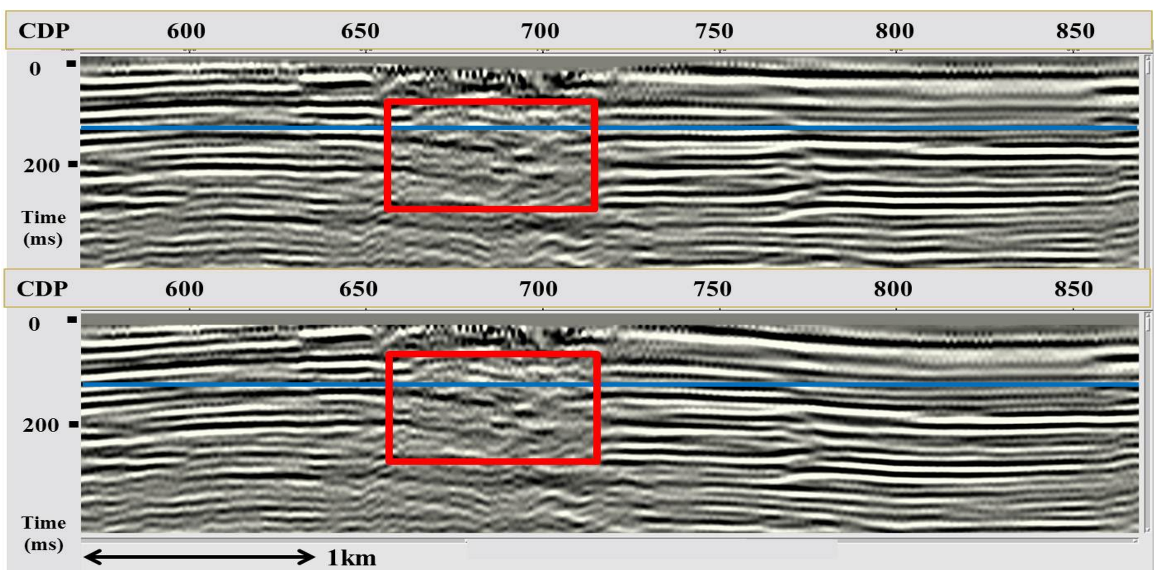

Figure 5.29: Stack comparison of no statics on the top vs RDT statics at the bottom. X axis is CDP number, vertical axis is time in ms.

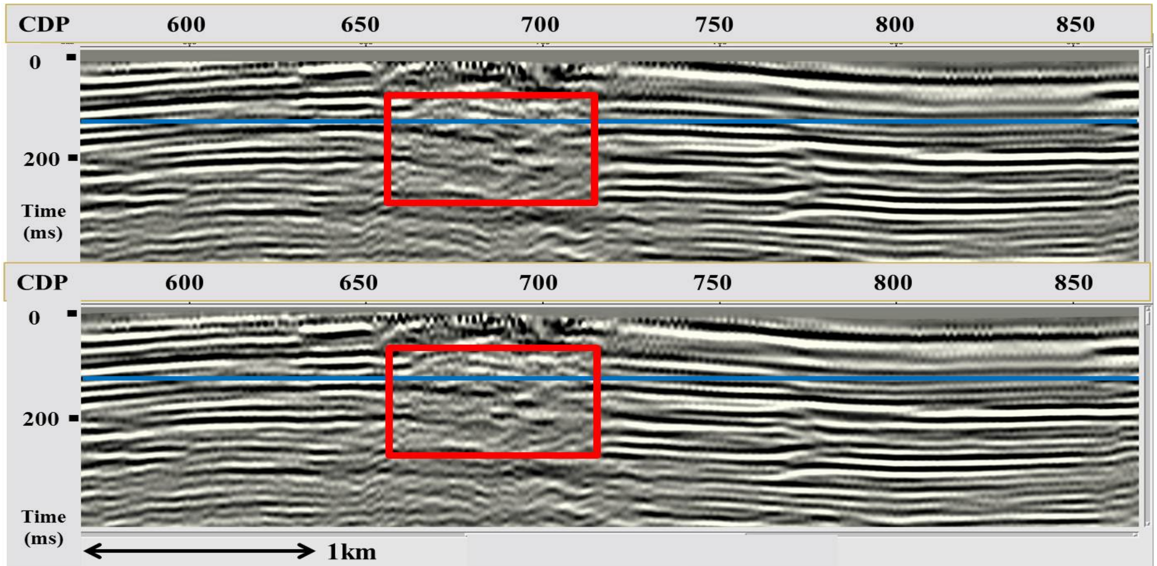

Figure 5.30: Stack comparison of RDT on the top vs FAT statics at the bottom. X axis is CDP number, vertical axis is time in ms.

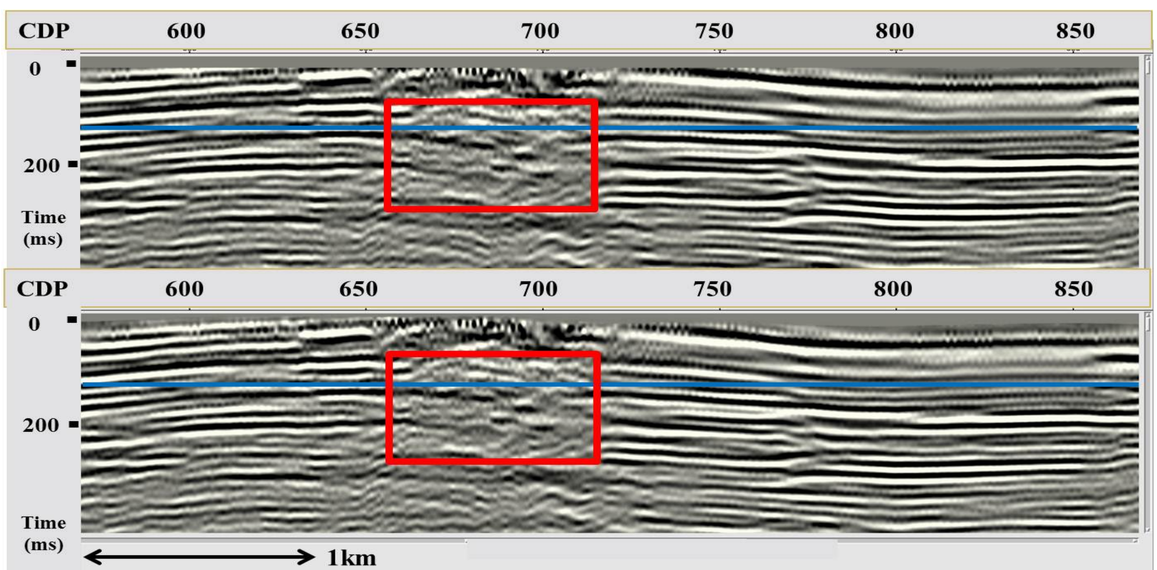

Figure 5.31: Stack comparison of RDT on the top vs EAT statics at the bottom. X axis is CDP number, vertical axis is time in ms.

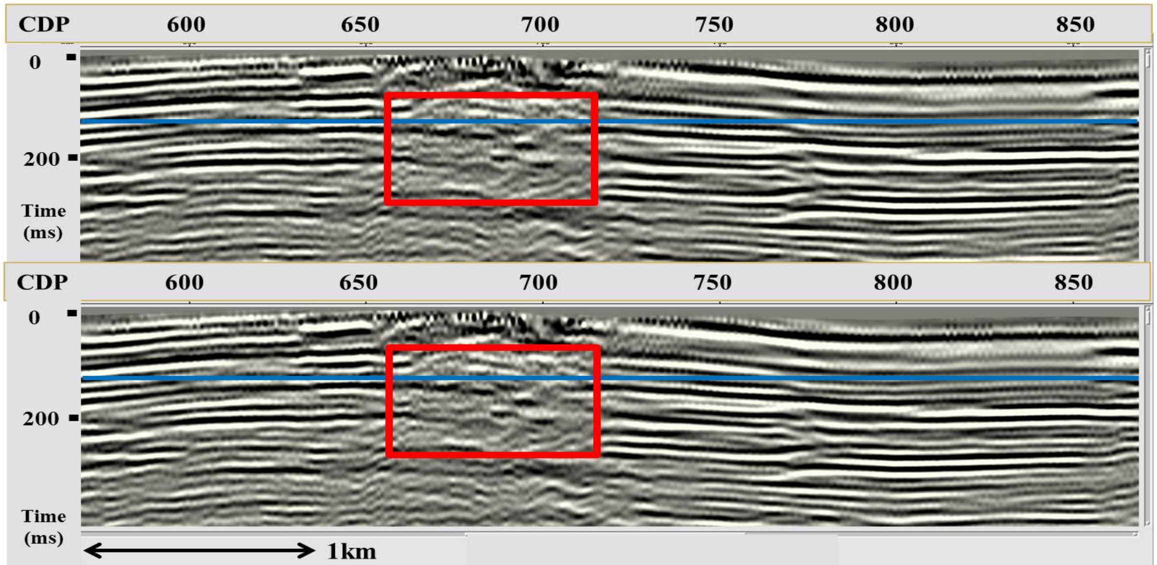

Figure 5.32: Stack comparison of FAT on the top vs EAT statics at the bottom. X axis is CDP number, vertical axis is time in ms.

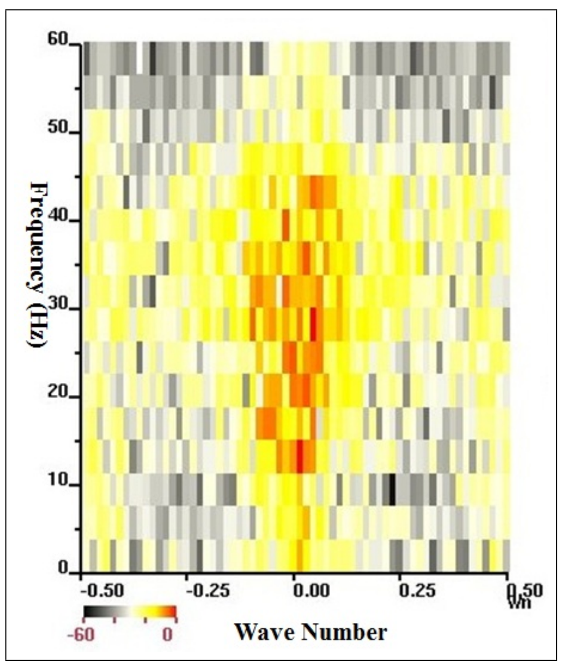

Figure 5.33: FK analysis of no statics. X axis is wave number, vertical axis is frequency.

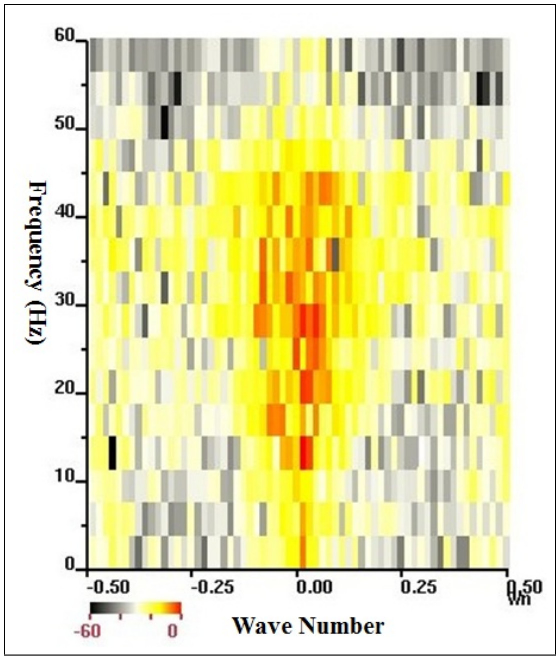

Figure 5.34: FK analysis of RDT. X axis is wave number, vertical axis is frequency.

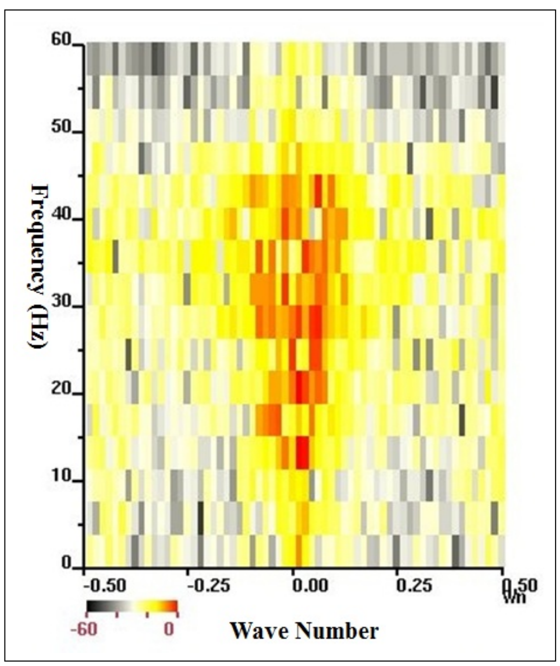

Figure 5.35: FK analysis of RDT. X axis is wave number, vertical axis is frequency.

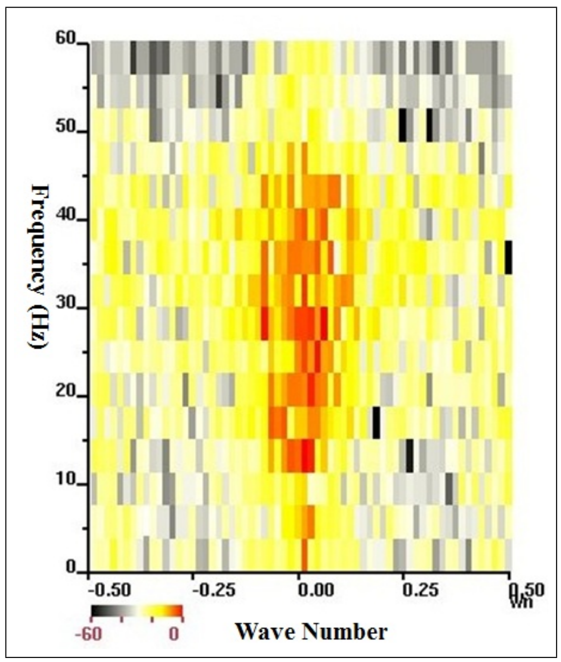

Figure 5.36: FK analysis of RDT. X axis is wave number, vertical axis is frequency.

Chapter 6

CONCLUSIONS

Both Refraction Delay-Time Method (RDT) and First-Arrival Traveltime Tomography (FAT) utilize first breaks to derive near surface velocities and can provide cost efficient and accurate near surface velocity models in many geological settings.

RDT would be a very good choice assuming the near-surface structure is simple, layer based, and has a stable refractor, as often is the case. It costs the least when comparing with FAT and EAT, since we only need to pick one or two branches most of the time. However, when the layer assumption for velocity structures fails, as in the case of rough topography and severe lateral velocity variations as demonstrated in this study, the results from RDT are insufficient to remove the near-surface distortions. In these situations more advanced geophysical tools are required.

FAT may produce better solutions using properly picked traveltime data as long as the velocity still generally increases with depth. The velocity models produced for both the Peru and Malaysia data appear more consistent with what is known about the near-surface geology, and the stack sections generally appear more reasonable than that performed with RDT.

In more complex near-surface situations, such as in the case of Peru, first arrival interpretation can be very difficult. The Early-Arrival Waveform Tomography (EAT) method can provide additional ability to resolve shallow velocity structures. This method fits early arrivals in the seismic data, including direct waves, refractions, diffractions, and reflections, thus enabling it to gain better detail in the inversion. Because of the additional data it can incorporate, it is less dependent on the traveltime picks, a benefit that appears to be driving the interest in this methodology. For the Peru dataset EAT has provided a better velocity estimate. The main disadvantage to the technique is of course it's computational cost.

In the case of the OBC data in Malaysia, the FAT and EAT solutions appeared to produce better statics in the core of the anticline than the RDT technique, at least as judged by the structural changes on some of the events. The first arrivals were very good and the near-surface geology was not very complicated so FAT could produce a reasonably good inversion. For the EAT technique to produce better results it would need additional development, such as the ability to model multiples and perhaps converted waves.

To summarize, it is difficult to tell which technique provides a better solution without additional geology information or data such as line ties and well logs. But the greater continuity, stronger event, and general flatness is promising and encouraging that EAT is possibly superior, at least in the Peru dataset.

Further research such as migrating the data in depth may produce better structural images, particularly in the OBC dataset. Moreover, applying EAT with geophone data or the summation of hydrophone and geophone data may also produce better solutions since they include more low frequency information.

Bibliography

Aki, K., and P. Richards, 2002, Quantitative seismology: University Science Books. Geology (University Science Books).: Seismology.

Aldridge, D. F., and D. W. Oldenburg, 1992, Refractor imaging using an automated wavefront reconstruction method: Geophysics, **57**, 378–385.

Ammon, C. J., and J. E. Vidale, 1993, Tomography without rays: Bulletin of the Seismological Society of America, **83**, 509–528.

Boonyasiriwat, C., P. Valasek, P. Routh, B. Macy, W. Cao, and G. T. Schuster, 2008, An application of time-domain multiscale waveform tomography to marine data: SEG Technical Program Expanded Abstracts, **27**, 3704–3708.

Buddensiek, M.-L., J. Sheng, T. Crosby, G. T. Schuster, R. L. Bruhn, and R. He, 2008, Colluvial wedge imaging using traveltime and waveform tomography along the Wasatch Fault near Mapleton, Utah: Geophysical Journal International, **172**, 686–697.

Bunks, C., F. M. Saleck, S. Zaleski, and G. Chavent, 1995, Multiscale seismic waveform inversion: Geophysics, **60**, 1457–1473.

Ernst, J. R., A. G. Green, H. Maurer, and K. Holliger, 2007, Application of a new 2D time-domain full-waveform inversion scheme to crosshole radar data: Geophysics,

72, J53–J64.

Gardner, L. W., 1939, An areal plan of mapping subsurface structure by refraction shooting: Geophysics, **4**, 247–259.

Gauthier, O., J. Virieux, and A. Tarantola, 1986, Two-dimensional nonlinear inversion of seismic waveforms; numerical results: Geophysics, **51**, 1387–1403.

Ha, W., S. Pyun, C. Shin, and D.-J. Min, 2006, Application of refraction tomography algorithms to real data: SEG Technical Program Expanded Abstracts, **25**, 3335–3339.

Hagedoorn, J. G., 1959, The plus-minus method of interpreting seismic refraction sections: Geophysical Prospecting, **7**, 158–182.

He, L., J. Zhang, and W. Zhang, 2011, Tradeoffs in the near-surface seismic imaging solutions: SEG Technical Program Expanded Abstracts, **30**, 4015–4019.

Jaillard, E., G. Laubacher, P. Bengtson, A. V. Dhondt, and L. G. Bulot, 1999, Stratigraphy and evolution of the Cretaceous forearc Celica-Lancones Basin of Southwestern Ecuador: Journal of South American Earth Sciences, **12**, 51 – 68.

Kltzsch, P., 1986, Inverse problems of acoustic and elastic waves. ed. by santosa, f./pap, y.-h./symes, w. w./holland, c., philadelphia, siam 1984. distr. by j. wiley. ix, 365 s., 36.65: ZAMM - Journal of Applied Mathematics and Mechanics / Zeitschrift fr Angewandte Mathematik und Mechanik, **66**, 447–447.

Lawton, D. C., 1989, Computation of refraction static corrections using first-break traveltime differences: Geophysics, **54**, 1289–1296.

Levander, A. R., 1988, Fourth-order finite-difference p-sv seismograms: Geophysics, **53**, 1425–1436.

Luo, Y., and G. T. Schuster, 1991, Wave equation inversion of skeletalized geophysical data: Geophysical Journal International, **105**, 289–294.

Lutter, W. J., R. L. Nowack, and L. W. Braile, 1990, Seismic imaging of upper crustal structure using travel times from the passcal ouachita experiment: J.Geophys.Res., **95**, 4621–4631.

Min, D.-J., and C. Shin, 2006, Refraction tomography using a waveform-inversion back-propagation technique: Geophysics, **71**, R21–R30.

Moser, T. J., 1991, Shortest path calculation of seismic rays: Geophysics, **56**, 59–67.

Nemeth, T., E. Normark, and F. Qin, 1997, Dynamic smoothing in crosswell traveltime tomography: Geophysics, **62**, 168–176.

Nolet, G., 1987, Seismic tomography: With applications in global seismology and exploration geophysics: D. Reidel. Seismology and Exploration Geophysics.

Ravaut, C., S. Operto, L. Improta, J. Virieux, A. Herrero, and P. Dell'Aversana, 2004, Multiscale imaging of complex structures from multifold wide-aperture seismic data by frequency-domain full-waveform tomography: application to a thrust belt: Geophysical Journal International, **159**, 1032–1056.

Sheng, J., A. Leeds, M. Buddensiek, and G. T. Schuster, 2006, Early arrival waveform tomography on near-surface refraction data: Geophysics, **71**, U47–U57.

Sheriff, R., 2002, Encyclopedic dictionary of applied geophysics: Society of Exploration Geophysicists. Seismology and Exploration Geophysics.

Shipp, R. M., and S. C. Singh, 2002, Two-dimensional full wavefield inversion of wide-aperture marine seismic streamer data: Geophysical Journal International, **151**, 325–344.

Stork, C., 2009, Addressing key land data quality challenges with passive seismic interferometry: SEG Technical Program Expanded Abstracts, **28**, 3238–3243.

Tarantola, A., 1984, Inversion of seismic reflection data in the acoustic approximation: Geophysics, **49**, 1259–1266.

Zelt, C. A., A. Azaria, and A. Levander, 2006, 3D seismic refraction traveltime tomography at a groundwater contamination site: Geophysics, **71**, H67–H78.

Zhang, J., and M. N. Toksoz, 1998, Nonlinear refraction traveltime tomography: Geophysics, **63**, 1726–1737.

Zhang, W., and J. Zhang, 2011, Full waveform tomography with consideration for large topography variations: SEG Technical Program Expanded Abstracts, **30**, 2539–2542.

Zhu, X., D. P. Sixta, and B. G. Angstman, 1992, Tomostatics: Turning-ray tomography + static corrections: The Leading Edge, **11**, 15–23.

Zhu, X., P. Valasek, B. Roy, S. Shaw, J. Howell, S. Whitney, N. D. Whitmore, and P. Anno, 2008, Recent applications of turning-ray tomography: Geophysics, **73**, VE243–VE254.